A Fluid Loop Actuator for Active Spacecraft Attitude Control

—

A Parametric Sizing Model and the Design, Verification, Validation and Test with a Prototype on an Air Bearing

Bas Martens

Dissertation in Partial Fulfilment of the Master of Philosophy in Space Studies

Department of Electrical Engineering

University of Cape Town

February 2019

SL19 – 03M

Declaration

I, Bas Martens, know the meaning of plagiarism and declare that all the work in the document, save for that which is properly acknowledged, is my own. It has not been previously submitted, in part or whole, to any university of institution for any degree, diploma, or other qualification. This thesis/dissertation has been submitted to the Turnitin module (or equivalent similarity and originality checking software) and I confirm that my supervisor has seen my report and any concerns revealed by such have been resolved with my supervisor.

Signed by candidate

Signed_____

1 February 2019

Abstract

Active spacecraft attitude control by using a pumped fluid as the inertial mass has potential advantages over reaction wheels, including high torque, lower power consumption, reduced jitter and prolonged lifetime. Previous work addressed conceptual and mission-specific control aspects, and one fluid loop has flown on a demonstration mission. In this dissertation, a parametric sizing model is developed that can optimize a fluid loop for any mission, based on pump capabilities and customer requirements. The model can be applied to circular, square and helical fluid loops, and includes the power consumption due to viscous friction. A configurable prototype was developed to verify the model, as well as a spherical air bearing to verify the rotational aspects of the various fluid loop configurations. The model was applied to various hypothetical missions. In conclusion, the fluid loop has the fundamental potential to replace reaction wheels in a wide variety of satellites above approximately 20 kg, if mass is carefully optimized and efforts are made to develop a suitable pump. This is considered worthwhile, as the actuator comes with many potential advantages.

Acknowledgements

I would like to extend many thanks to:

- Professor Peter Martinez, for the great support and advice throughout the project, and his immeasurable dedication to the SpaceLab.
- The other professors at the SpaceLab, for the exciting and thought-provoking lessons.
- Rudi Glatthaar, Johann Joubert and the other people at NewSpace Systems, for their expertise, trust and collegiality.
- James Barrington-Brown, for giving me the opportunity to work on this awesome project.
- My parents, Jos and Heleen, who enabled me to do my studies in South Africa, and who are also very nice people in general.

Table of Contents

Declaration ii

Abstract iii

Acknowledgements iv

List of Tables viii

List of Figures ix

Nomenclature xii

1 Introduction 1

1.1 Background 1

1.2 Inertial Attitude Actuation 3

1.3 Fluid Inertial Attitude Actuation 5

1.3.1 Pumping Strategies 8

1.3.2 Performance Parameters 9

1.4 Project Objectives 13

1.5 Dissertation Layout 13

2 Fundamentals of Attitude Actuation and Fluid Dynamics 15

2.1 Fundamentals of Attitude Actuation 15

2.1.1 Reference Frames 15

2.1.2 Rotational Motion 17

2.1.3 Disturbance Environment 19

2.1.4 Actuator Sizing Requirements 27

2.2 Fundamentals of Fluid Dynamics 30
2.2.1 Basic principles 30
2.2.2 Major Viscous Losses 32
2.2.3 Minor Viscous Losses 35
2.2.4 Pumping and Power Consumption 38
3 Requirements and Constraints 40
3.1 Requirements Validation 40
3.2 Requirements and Constraints for the Sizing Model 41
3.3 Requirements and Constraints for the Fluid Loop Prototype 44
3.4 Requirements and Constraints for the Air Bearing 46
4 Sizing a Fluid Loop 48
4.1 Fluid Loop Attitude Actuation 49
4.1.1 Mass 49
4.1.2 Angular Momentum 50
4.1.3 Torque 54
4.2 Fluid Loop Fluid Dynamics 55
4.2.1 Fluid Properties 55
4.2.2 Pressure Drop 56
4.2.3 Pumping and Power consumption 58
4.3 Fluid Loop Sizing Relations 60
5 Verification, Validation and Test 63
5.1 Fluid Loop Prototype VV&T 64
5.1.1 Reconfiguration of the Fluid Loop (Requirement FL-3) 65
5.1.2 Filling Mechanism (Requirement FL-10) 66
5.1.3 Flow Rate Measurement and Characterization (Requirement FL-5) 67
5.1.4 Pressure Drop Measurement (Requirement FL-6) 68

5.1.5 Power Consumption Measurement (Requirement FL-7) 70
5.2 Air Bearing VV&T 71
5.2.1 Balancing the Rotating Assembly (Requirement AB-4 and AB-5) 72
5.2.2 Angular Motion Measurement (Requirement AB-8) 73
5.3 Sizing Model Verification 78
5.3.1 Angular Momentum 79
5.3.2 Torque 80
5.3.3 Pressure Drop 80
5.3.4 Power Consumption 85
5.3.5 Orbital Disturbance Model 86
5.4 Sizing Model Validation 90
5.5 Sizing Model Test 92
5.5.1 Method 92
5.5.2 Optimizations 95
5.5.3 Final Comments on Pumping 98

6 Conclusions 99
6.1 Limitations 101
6.2 Recommendations 101

References 104
Appendices 111
Appendix 1: Altitude - Atmospheric Density Relation 112
Appendix 2: Satellite Mass – Residual Magnetic Moment Relation 113
Appendix 3: Integration of Angular Momentum in Rounded Corners 114
Appendix 4: Reverse-Calculation of MHD Pumping Efficiencies 115
Appendix 5: User Manual for the Sizing Model 116
Appendix 6: Mass Optimizations of Fluid Loops for Various Missions 121

List of Tables

Table 1-1 An overview of patents and literature on fluid attitude actuation in chronological order. The performance parameters of a fluid loop that are suggested to exceed those of reaction wheels are marked with a "+". 7

Table 1-2 The performance parameters of inertial attitude actuators. The PPs marked with an asterisk are of most interest in this dissertation. 10

Table 2-1 Reflectance factors of various materials. [35] 21

Table 4-1 The properties of various liquids at room temperature (25 °C). 55

Table 4-2 Surface roughness values of various channel materials. [51], [53] 57

Table 4-3 Data of two physical and three simulated magnetohydrodynamic fluid loops, respectively, and their reverse-calculated flow rate accelerations and overall efficiencies. 60

Table 5-1 Requirements verification of the fluid loop prototype. The different types of verification activities are, in order of increasing rigor: Inspection (I), Demonstration (D), Test (T) and Analysis (A) ... 64

Table 5-2 Requirements verification of the air bearing. The different types of verification activities are, in order of increasing rigor: Inspection (I), Demonstration (D), Test (T) and Analysis (A). Requirement AB-8.b (acceleration measurement) was not met due to a missing inertial measurement unit. 71

Table 5-3 Requirements verification of the fluid loop sizing model. The different types of verification activities are, in order of increasing rigor: Inspection (I), Demonstration (D), Test (T) and Analysis (A) ... 78

Table 5-4 the measured angular velocities of various configurations of the fluid loop (average of four tests) versus the expected theoretical values. The minimal deviation verifies the theory. 79

Table 5-5 Data of various satellite missions and their reaction wheels that are used as benchmarks to verify the orbital disturbance model. 88

Table 5-6 Data of various missions that serve as requirements and boundaries for the fluid loop optimizations. 93

Table 5-7 Data of various COTS mechanical pumps and MHD pumps that serve as boundaries for the fluid loop optimizations. 93

List of Figures

Figure 1-1 An astronaut unsuccessfully attempting to capture the spinning Intelsat 603, due to the rotating liquid propellant in the tanks (left). During a later spacewalk, three astronauts improvise a method to capture the satellite by hand (right). [2] [6] 1

Figure 1-2 An overview of the attitude determination and control system (ADCS) on a satellite and the various actuation methods. 4

Figure 1-3 Patent drawings from the first fluid attitude actuation patens from 1956, 1988 and 1989, respectively. [9], [11], [12] 5

Figure 1-4 Fluid loop hardware. (Left) The three-axes controlled cube taken on the parabolic flight. [14] (Centre) The single axis fluid loop from McGill, also tested on three axes. [26] (Right) The FDA-A6 that is currently operating on-orbit aboard the TechnoSat. [14], [26], [28] 6

Figure 1-5 Various methods of pumping, [from left to right] a gear pump, centrifugal pump and magneto-hydro-dynamic pump. Images modified from [22], [92], [93]. 9

Figure 2-1 The reference frames of interest to an Earth-centred mission. See the text for a discussion of the axes depicted in this diagram. 16

Figure 2-2 The variation with altitude of the major environmental disturbance torques on a satellite. The values are indicative, as this differs strongly per mission. [94] 19

Figure 2-3 The conceptual working and variables of the worst-case solar radiation torque. 20

Figure 2-4 The conceptual working and variables of the (worst-case) aerodynamic torque. 22

Figure 2-5 A simplified relation between atmospheric density and altitude, based on the NRL-MSIS-E-00 model at solar maximum ($N10.7 = 200$) and high density conditions to obtain a worst-case value. 23

Figure 2-6 The conceptual working and variables of the (worst-case) magnetic torque. 23

Figure 2-7 A generalized relation between a satellite's mass and its residual magnetic moment to help approach a realistic value for satellites of all sizes. 25

Figure 2-8 The conceptual working and variables of the (worst-case) gravity gradient torque. 26

Figure 2-9 Perifocal top view of the orbital plane, describing the geometry of a symmetric target-pointing manoeuvre at the beginning (t1) and end (t2). The satellite is in a circular orbit and passes exactly over the ground-based target 28

Figure 2-10 The parabolic velocity profile of a laminar flow in a pipe. The shear stress that causes viscous energy loss is proportional to the viscosity and velocity gradient. Turbulent flow has a more stub-nosed velocity profile, but an equal average velocity under continuity. 32

Figure 2-11 Turbulent and laminar pipe flow. 33

Figure 2-12 The Moody diagram shows the friction factor as a function of the Reynolds number and the relative pipe roughness. [51] 34

Figure 2-13 Two types of flow distortion in a bend that increase the friction loss in the pipe. [53] 36

Figure 2-14 Visualization of the three components of the bend resistance coefficient as a function of the relative bend radius for a given friction factor. [53] 37

Figure 4-1 Various fluid loop configurations (circular, square, helical) and channel cross-sections (circular, rectangular) with the dimensional notation used in this analysis. 48

Figure 4-2 Two fluid loops with different masses and channel diameters, but equal angular momentums. 51

Figure 4-3 The radius and velocity of an arbitrary fluid slice point mass in a circular and square fluid loop. These variables dictate the point mass' angular momentum. 52

Figure 4-4 The geometry of the angular momentum of a point mass in a rounded corner of a FLIA. 53

Figure 4-5 The angular momentum of the fluid loop can be scaled up by winding it in coils, thus increasing the effective flow rate. It can be seen as multiple small fluid loops working in parallel, actuated by a single pump. 54

Figure 4-6 Viscous friction in the loop results in a pressure drop that is compensated by the pump. 56

Figure 4-7 The angular momentum per unit mass ("mass efficiency"), and per unit power ("power efficiency"), as a function of flow rate and channel diameter. The graphs are specific to one configuration, but similar trends apply to all fluid loops. This configuration is for a circular fluid loop (D= 800 mm) with a circular channel cross-section, using water as working fluid and an overall efficiency of 10%. The inverse relation between the two efficiencies visualized in these graphs complicates the sizing process. 62

Figure 5-1 The fluid loop prototype VV&T setup on table-top. Software on the laptop sets the control voltage for the pump controller, and reads out electronic pressure measurements. The pump speed is be verified with the oscilloscope. 63

Figure 5-2 Some of the configurations of the fluid loop prototype in various stages of integration, all with a loop diameter of D = 180 mm. In clockwise order, starting top-left: the default configuration (no electronics, d = 4 mm); the helical configuration (tubing only; d = 4 mm; 10 coils); the square configuration with sharp elbows (d = 4 mm); the thin tube configuration (d = 2.5 mm). 65

Figure 5-3 The custom-designed filling housing and screws. 66

Figure 5-4 Left: A section view of one of the two filling cavities that hydraulically connects a pump port to the loop, pressure sensor and filling tubes. Right: Filling the fluid loop with a syringe. 66

Figure 5-5 Test results that show the relation between the control voltage and the flow rate. This is used by the interface software to control the pump speed. 68

Figure 5-6 A top view of the fluid loop. The pressure drop theory is only concerned with the green part of the loop, so the red part must be isolated and deducted from the test results. 68

Figure 5-7 The pressure drop over the entrance regions of the three different channel diameters: 2.5, 4 and 5 mm, respectively. The 2.5mm and 5mm entrances include the reducer fittings to adapt the diameter. 69

Figure 5-8 Side view of the air bearing that was designed for attitude tests with the fluid loop. The background grid squares are 10×10 cm². 71

Figure 5-9 Section view of the air bearing with the centre of gravity (black/white) aligned with the axis of rotation (green), with which the blue axis of symmetry should coincide. This can be approached by shifting the balancing weight. 72

Figure 5-10 The laser diode mounted on the rotating assembly pointing the angular position on a degree arc on the floor. The angular velocity is then derived from a video recording. 73

Figure 5-11 The variation of the air bearing's rotation over time. A cyclic and secular disturbance can be distinguished; the latter eventually brings the velocity down enough that the assembly stops making full rotations and starts oscillating around the point of stable equilibrium. 75

Figure 5-12 The variation of the disturbance accelerations on the rotating assembly as a function of its angular position, measured over multiple rotations. The points of equilibrium are around the intersections with the horizontal axis. 75

Figure 5-13 The measured pressure drop over the fluid loop as a function of flow rate versus the four theoretical predictions. Default configuration, circular loop, D= 180 mm, d= 4 mm. Corrected for entrance region friction. The sole discrepant measurement is disregarded; see text for further interpretation. 81

Figure 5-14 The measured pressure drop over the fluid loop as a function of flow rate versus the four theoretical predictions. Thin tube configuration, circular loop, D= 180 mm, d= 2.5 mm. Corrected for entrance region friction. 82

Figure 5-15 The measured pressure drop over the fluid loop as a function of flow rate versus the four theoretical predictions. 10 coil helix configuration, circular loop, D= 180 mm, d= 4 mm. Corrected for entrance region friction. 82

Figure 5-16 The measured pressure drop over the fluid loop as a function of flow rate versus the four theoretical predictions. Square loop with rounded corners, D= 180 mm, d= 4 mm, R_{corner}= 15 mm. Corrected for entrance region friction. 82

Figure 5-17 The measured pressure drop over the fluid loop as a function of flow rate versus the four theoretical predictions fitted curve that shows the K-factor of the non-ideal elbows. Square loop with sharp elbows, D= 180 mm, d= 4 mm, R_{corner}= 15 mm. Corrected for entrance region friction. 82

Figure 5-18 The derived pumping efficiency of the MGD1000F gear pump as a function of the pressure drop, at different flow rates. 85

Figure 5-19 The user interface of the orbital disturbance model that calculates attitude actuator requirements based on the satellite and mission parameters. It combines all equations described in section 2.1.3. 87

Figure 5-20 The user interface of the fluid loop sizing model. The user can input design parameters that result in the performance parameters of the fluid loop, which can then be compared to the set requirements. Using the Excel Solver function allows for optimization of the design parameters. 90

Figure 5-21 A suggested fluid loop configuration – a coiled square loop with rounded bends along the outer perimeter of the satellite. It has optimized geometry, light channel walls, and an impact- and leak-resistant outer casing, making it mass-efficient and safe from leaks. 94

Nomenclature

Abbreviation	Definition
ACDS	Attitude determination and control subsystem
Ceteris Paribus	While other conditions remain the same
CG	Centre of gravity
CM, cm	Centre of mass
Cp	Centre of pressure
GEO	Geosynchronous orbit
LEO	Low Earth orbit
MHD	Magnetohydrodynamic
MoI	Moment of inertia
NASA	National Aeronautics and Space Administration
NSS	NewSpace Systems
PoI	Product of inertia
Secular	Accumulating

Roman Symbol	Quantity	Unit
[–]	Dimensionless	–
A	Area	m^2
B	Geomagnetic field strength	T
c	Speed of light	$3 \cdot 10^8\ m/s$
C_d	Drag coefficient	–
d	Distance	m
d, D	Diameter	m
D	Spacecraft residual dipole moment	$A\ m^2$

f	Friction factor	$-$
F	Force	N
g	Gravitational acceleration	m/s^2
h	Altitude, height	m
h, H	Angular momentum	$N\ m\ s$
i	Orbital inclination	rad
I	Moment of inertia	$kg\ m^2$
K	Resistance coefficient	$-$
L	Length	m
m	Mass	kg
n, N	Number	$-$
p	pressure	Pa, bar
P	Power	W
q	Reflectance factor	$-$
Q	Flow rate	$m^3/s, L/min$
r, R	Radius	m
t	Time	s
T	Period	s
v	Velocity	m/s
V	Volume	m^3, L
w	Width	m
y	Distance	m
z	Vertical distance	m

Greek Symbol	**Quantity**	**Unit**
α	Angular acceleration	rad/s^2
$\alpha, \beta, \gamma, \theta$	Angle	rad
γ	Specific weight	N/m^3
ε	Surface roughness	mm

ε	Effective horizon from ground station	rad
η	Overall electrical efficiency	%
η	Off-nadir angle	rad
λ	Function of the geomagnetic latitude (0…1)	$-$
λ	Angle at Earth's centre from target to satellite	rad
μ	Absolute/dynamic viscosity	$Pa\ s$
μ	Standard gravitational parameter of the Earth	$3.99 \cdot 10^{14}\ m^3/s^2$
υ	Kinematic viscosity	m^2/s
ρ	Density	kg/m^3
σ	Fluid shear stress	Pa
τ	Torque	$N\ m$
φ	Angle of incident sunlight	rad
Φ	Solar constant	$1366\ W/m^2$
ω	Angular velocity	$rad/s, deg/s$
Ω	Orbital rate	rad/s

1. Introduction

In 1992, the Space Shuttle *Endeavour* set out on its maiden flight to capture Intelsat 603. Due to a separation failure of the upper stage from the second stage of the Titan III launch vehicle, the four-tonne communication satellite was stranded in low Earth orbit (LEO) instead of its intended geostationary orbit (GEO). The rescue plan was to capture the huge spinning satellite with a specially designed bar, attach a booster rocket to it, and send it on its way to GEO.

Despite extensive training in a microgravity simulation environment, six attempts during two extravehicular activities were not enough to arrest the satellite's spin and capture it. It turned out that the inertia of the rotating liquid propellant inside the tanks retained the satellite's spin. [1], [2] Although unintended and undesired, this was the first demonstration in space of attitude stabilization by a rotating liquid.

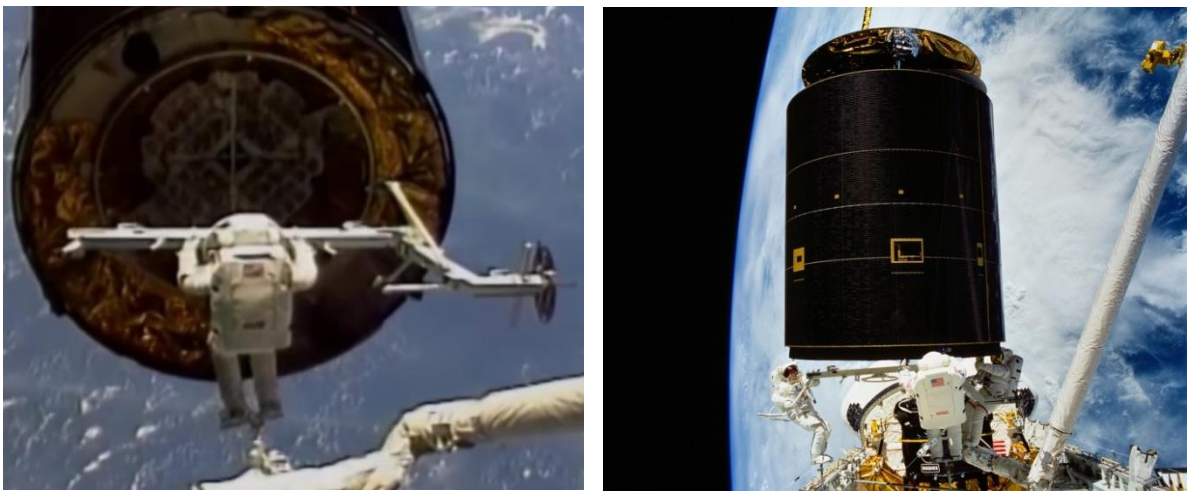

Figure 1-1 An astronaut unsuccessfully attempting to capture the spinning Intelsat 603, due to the rotating liquid propellant in the tanks (left). During a later spacewalk, three astronauts improvise a method to capture the satellite by hand (right). [2] [6]

1.1 Background

Controlling the orientation of a spacecraft is crucial for achieving its mission objectives, whether it is for pointing a payload, a communications antenna, or executing orbital manoeuvres. Historically, this has been done by employing passive methods such as gravity-gradient or spin-stabilization, or none at all. But as payloads, attitude determination capabilities and space-hardened on-board computing improved, so too grew the demand for more accurate and agile attitude control. [3]–[5] Subsequently, this demand for more capabilities was followed by a demand for cost reductions and reliability improvement, and was accelerated by the growth and commercialization of the space sector. As with all space systems, the push to improve capability, cost and reliability has shaped the technology of attitude actuators to the wide variety of options that is available today. This is an on-going process. [6]

Fluid attitude actuation is one of these variants. Fluid attitude actuation works on the same principle as conventional attitude actuation with wheels, but it uses the angular momentum of a liquid pumped through a closed loop instead of a solid mass rotating on an axle. This relatively unknown concept is becoming more popular and has recently made a jump in development with the launch of a fluid actuator aboard the German technology demonstration satellite TechnoSat in 2017.

The South African company NewSpace Systems (NSS) has also expressed an interest in developing a fluid attitude actuator. NSS specializes in the development of parts for the attitude determination and control subsystems (ADCS) for satellites and satellite constellations. NewSpace Systems and the author have set up a collaboration in which NSS provides supervision, funding, procurement and electrical integration of the first test setups, while the author provides the efforts described in this dissertation: desktop research, the development of a sizing model for fluid loop actuators, the mechanical design of the test prototype and spherical air bearing, and performance and analysis of the tests.

This chapter gives a brief introduction to attitude actuation with wheels and a more detailed introduction on fluid attitude actuation, reviewing previous work, pumping strategies, and the performance parameters used to characterize and compare their utility. Based on this, the scope and objectives of this project are determined. The final section of the chapter presents the layout of this dissertation.

1.2 Inertial Attitude Actuation

The ADCS of a spacecraft, and more specifically a satellite, is responsible for orienting and pointing the spacecraft on a set target and compensating for external and internal disturbance torques. As can be seen in Figure 1-2, the ADCS can be subdivided into three parts: the attitude sensors that determine the orientation of the spacecraft; the computing hardware, software and control algorithms that give correcting commands to where the satellite should be pointing; and the actuators that execute these control commands. This dissertation concerns actuators, which can be subdivided in passive and active actuators. Nearly all modern satellites possess some form of active attitude control. Missions that require a high pointing accuracy or manoeuvrability achieve this by exchanging angular momentum with an inertial mass inside the spacecraft. The fluid loop actuator falls in this category.

Inertial attitude actuation works on the principle of conservation of angular momentum. By accelerating or decelerating a rotating wheel inside the satellite, the satellite can be steered to perform slew manoeuvres, or unwanted rotation can be countered by transferring the angular momentum from the satellite structure into the rotation of the wheel's mass. Unwanted rotation can already be present in a tumbling satellite after orbit insertion or attitude failure. However, for the vast majority of a satellite's operation unwanted rotation is induced by external disturbance torques exerted by the space environment on the satellite. [7]

Depending on the spacecraft's orbit and orientation, the disturbances can by cyclic or secular. Cyclic torques cancel themselves out over the course of one orbit, whereas secular torques have a non-zero value after each orbit. Inertially compensating for secular torques leads to a build-up of angular momentum in the rotating mass of the actuator. When the mass cannot be spun up any further due to internal friction in the motor and bearings, the actuator reaches saturation. In order to keep using the actuator, that angular momentum must be dumped. Consequently, inertial actuators are typically used in combination with actuators that exchange torques externally (e.g. magnetorquers or thrusters), in order to de-spin the wheel while keeping the satellite motion under control with the external torquers. Despite this limitation, inertial actuators are widely used because of their high degree of control and accuracy.

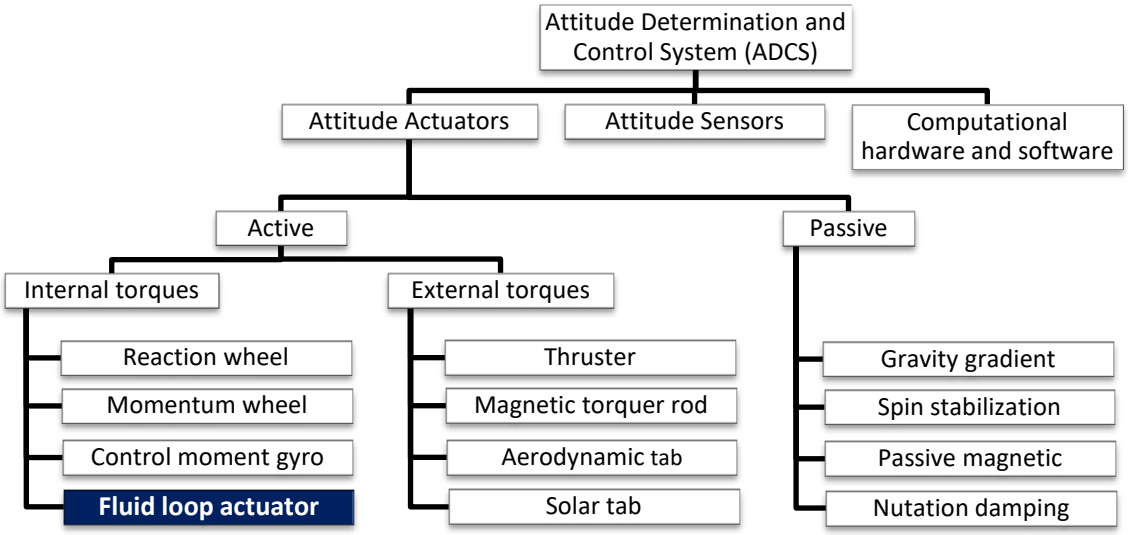

Figure 1-2 An overview of the attitude determination and control system (ADCS) on a satellite and the various actuation methods.

Each inertial actuator has its own advantages and disadvantages. [7] Reaction wheels are wheels with zero initial speed and are used for very accurate and versatile pointing requirements (>0.0001°). However, they are expensive, heavy, and three wheels are necessary for accurate three-axis control.

Unlike reaction wheels, momentum wheels have an initial speed to produce an angular momentum, resulting in gyroscopic rigidity that resists external disturbances. One momentum wheel on a satellite's pitch axis combined with external torquers such as magnetic torquers on the roll and yaw axes can be used for three-axes control and accurate nadir pointing (>0.01°). This is the most common form of attitude control in communication satellites. [8]

A control moment gyro (CMG) is a less frequently used attitude actuator. CMGs are momentum wheels on gimbals that can produce very large torques by rotating the wheel's axis of rotation. However, they are heavy, costly, their lifetime is limited, and their momentum must be controlled carefully to prevent gimbal lock.

The above wheel actuators differ in application, but they all operate on the principle of conservation of angular momentum. Because this principle is not necessarily reserved to a solid mass, a fluid loop could potentially fulfil the function of all of the above actuators. Whether fluid loops actually outperform wheels for specific missions can be determined by comparing their common system-level performance parameters such as angular momentum capacity, torque authority, power consumption and more. These performance parameters will be discussed in Section 1.3.2.

1.3 Fluid Inertial Attitude Actuation

Fluid attitude actuation works on the same principle as conventional attitude actuation with wheels, but it uses the angular momentum of a liquid pumped through a closed loop instead of a solid mass rotating on an axle.

Relatively little work has been done on fluid attitude actuation; in fact so little that all published work on the topic can be listed in Table 1-1. Nevertheless, the idea of using a fluid as an inertial mass to stabilize a satellite is as old as the space age itself – the first patent for fluid "orientation control for a space vehicle" was filed as early as 1956. [9] By the end of the 1980's the idea gained some momentum with improved patents filed by NASA, but the idea was dismissed due to concerns with leakage and thermal protection. [10]–[14] Only in the 2000's did other parties start investigating the idea past the concept level.

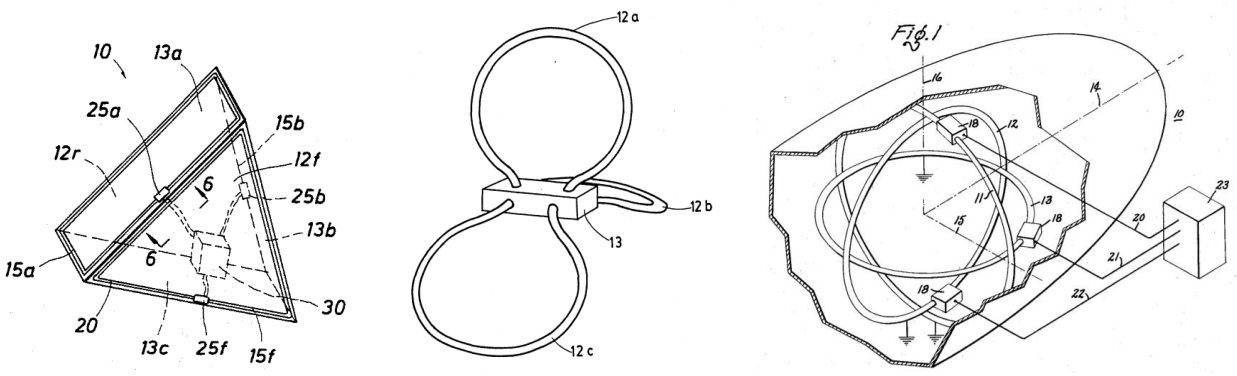

Figure 1-3 Patent drawings from the first fluid attitude actuation patens from 1956, 1988 and 1989, respectively. [9], [11], [12]

Theoretical work has been done on the feasibility of fluid loops and the simulation of control algorithms for fluid loops. [15]–[19] More recent theoretical work is focused on modelling *magneto-hydro-dynamic* (MHD) pumping, which will be briefly discussed in the next section. [20]–[22]

The first successful hardware demonstration was a three-axes controlled cube, developed by students at the University of Texas and tested on a parabolic flight to overcome previous difficulties with simulating the microgravity environment. [14] Other hardware tests by authors from McGill University and the Technical University of Berlin (TUB) took a less time-constrained (but less exciting) approach on an air bearing table in one or three axes, allowing for better characterization of the system. These tests were focused on validating the control algorithms for specific (hypothetical) missions. Most notably, the TUB researchers have recently developed the 30-centimetre Fluid Dynamic Actuator FDA-A6, which was launched in 2017

aboard the technology demonstration satellite TechnoSat. Much work has been done in preparation of this actuator, but little of it was published. [23]

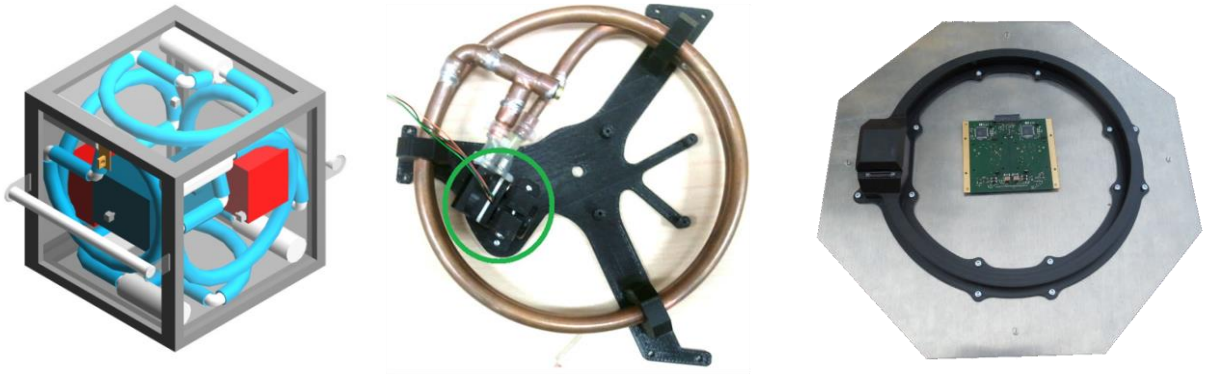

Figure 1-4 Fluid loop hardware. (Left) The three-axes controlled cube taken on the parabolic flight. [14] (Centre) The single axis fluid loop from McGill, also tested on three axes. [26] (Right) The FDA-A6 that is currently operating on-orbit aboard the TechnoSat. [14], [26], [28]

In general, all literature has very positive recommendations on the application of fluid loop actuators for a wide variety of missions, as either an auxiliary or autonomous actuator. Fluid loops have also been suggested and successfully simulated to take on other functions in a spacecraft, such as a passive libration damper that make use of the fluid's viscosity. [16] All in all, fluid loops seem to have a high potential to complement or substitute solid wheels and other attitude actuators. Therefore the question arises: *why has there been so little interest in fluid attitude actuation?* After reviewing the literature, the following conclusions can be drawn that help answer this question. At the same time, they indicate what previous work has not addressed, thus providing direction for this dissertation.

A reason for the lack of interest in the concept could be due to the fluid loop's lack of flight heritage. Developing and launching a new type of actuator from scratch is costly and risky, while the supply and demand for capable, flight-ready, flight-proven solid wheels is ubiquitous. The (alleged) advantages of a fluid loop actuator might not be big enough or worth this risk in the first place, which discourages the development of a fluid loop attitude actuator.

The little work published also suggests that the concept is simply not very well-known. Consequently, ADCS or mission designers are not aware of the potential of fluid loops, and consequently do not even consider them.

Table 1-1 An overview of patents and literature on fluid attitude actuation in chronological order. The performance parameters of a fluid loop that are suggested to exceed those of reaction wheels are marked with a "+".

Tech. Readiness Level [24]	Year	Author	Organisation	Title	Reference	Momentum Capacity	Torque Authority	Jitter/mass imbalance	Accuracy	Range	Power cons. /efficiency	Mass	Volume; shape	Schedule (design)	Price	Reliability	Robustness	Life Time	Redundancy	Passive Libration damping	Thermal management	EM/MHD Pumping	Mechanical pumping	Comments
2	1956	Haviland	General Electric	Orientation Control for a Space Vehicle (Patent)	[9]							+	+	+		+	+	+				+		Filed before Sputnik-1 launch!
2	1973	Wyatt	US Navy	Combined Fluid Flywheel and Propulsion System for Spacecraft (Patent)	[10]							+						*			+	+		Rotating tank, fluid follows. *Of the satellite, due to more efficient fuel use
2	1988	Maynard	JSC, NASA	Fluidic Momentum Controller (Patent)	[11]	+	+	+			+	+	+					+			+		+	Large bodies, damping of cyclic torques
2	1989	Iskenderian	JPL, NASA	Liquid Angular-Momentum Compensator (Patent)	[12]			+	*		+		+				+						+	*Better than thrusters
2	1991	Lurie	JPL, NASA	Fluid-Loop Reaction System (Patent)	[13]			+			+	+	+	+			+		+				+	
3	2003	Varatharajoo	Dresden UT	Approach for Combining Spacecraft Attitude and Thermal Control Systems	[15]							+	+	+	+			+			+	+		
5	2004	Kelly	University of Texas	A Performance Test of a Fluidic Momentum Controller in Three Axes	[14]			+			+	+	+	+							+		+	
3	2009	Kumar	Ryerson University, Toronto	Satellite Attitude Stabilization using Fluid Rings	[16]			+	+		+	+		+	+					+				Liquid propellant could be used
3	2009	Alkhodari, Varatharajoo	University Putra Malaysia	H2 and Hinf control options for the combined attitude and thermal control system	[17]																+			
3	2011	Shan	Harbin IT	Small Satellite Attitude Control based on Mechanically Pumped Fluid Loops	[18]		+	+			+	+	+	+						+			+	Small satellites; permanent magnets etc may influence the equipment sensitive to magnetism
2	2012	Casteras	CNES	Magnetohydrodynamic inertial actuator (Patent)	[25]				+									+				+		Especially in lower rpm regions due to no stiction
4	2013	Nobari	McGill University, Montreal	Attitude Dynamics and Control of Satellites with Fluid Ring Actuators (PhD)	[26]		+ *				–	+								+			+	Only high T/m ratio with high V; Good as aux. actuator with magnetic torquers or spin stab sat
4	2014	Noack	TU Berlin	Laboratory Investigation of a Fluid-Dynamic Actuator Designed for CubeSats	[27]		+				+					+	+					+		Small satellite
3	2015	Mesurolle	University of Toulouse	Finite Difference 2D Model of a Magnetohydrodynamic Inertial Actuator	[20]												+	+				+		
3	2015	Teyebi	University of Tehran	A Comparative Study of CMG and FMC Actuators for Nano Satellite Attitude Control System-Pyramidal Config	[19]		*	+	*			+	+										+	*In comparison to CMGs
3	2015	Curti	Sapienza University, Rome	MHD Reaction Wheel for Spacecraft Attitude Control: Configuration and Lumped Parameter	[21]			+					+	+		+						+		
3	2017	Curti	Sapienza University, Rome	Magneto-Hydro-Dynamics Liquid Wheel Actuator for Spacecraft Attitude	[22]	– *	– *	+			+			+		+							+		*Worse at higher torque and angular momentum demands
8	2017	Noack	TU Berlin	FDA-A6 – A Fluid-Dynamic Attitude Control System for TechnoSat	[28]		+				+					+	+	+		+		+	+	
						1	4	9	2		8	10	9	8	2	4	6	5	1	4	5	9	7	

Even if designers are aware of their potential, there is no widespread method of quantifying the characteristics of fluid loops in order to compare them to wheels. This is confirmed by the demand from the South African ADCS company, NSS. Even though NSS recognizes the potential of a fluid loop, there is no method readily available to grow their understanding past the conceptual level to allow for comparison with solid wheels, and it takes considerable work to map all new and unknown variables. This is one of the reasons for collaboration with the author. Other parties interested in fluid loops face a similar situation.

In addition, previous work has all been formulated from the perspective of one specific mission while focusing on the design and simulation of control algorithms, rather than sizing of the hardware itself – the size and fluid of the fluid loop are set once and are then computed. As opposed to sizing a solid wheel, there are previously unknown variables to consider. Hence, changing a fluid loop's input sizing parameters (such as loop geometry, fluid properties and pump capabilities) unintuitively influences its output performance parameters (such as angular momentum and power consumption). The relations between the fluid loop's input parameters and its performance parameters are not described, except for the angular momentum of a circular loop on one occasion. [27] Consequently, there is no framework for sizing or optimizing the geometry and other characteristics of the fluid loop.

In the next sections, fluid attitude actuation is elaborated by listing the overall performance parameters and how they compare to those of conventional solid wheels. This is done to (1) present a complete picture of the fluid loop and its strengths and weaknesses, and (2) to identify relevant performance parameters.

1.3.1 Pumping Strategies

Where a wheel has an electromotor to drive its mass, a fluid loop has a pump. The pumping strategy greatly influences all performance parameters, so it is necessary to briefly address them.

Conventional mechanical pumps, such as centrifugal pumps or gear pumps, are easy to implement and control, can propel almost any liquid, and give little magnetic interference. Centrifugal pumps are light and can produce a high flow rate, and gear pumps can produce a high pressure and accurate flow control. However, both can produce unwanted torques and momentum with their own rotation, and have moving parts, which implies vibration and a low overall reliability and lifetime in space.

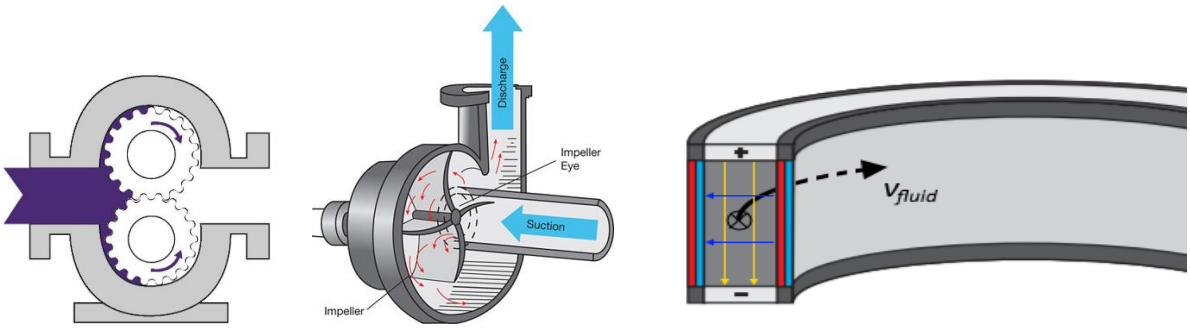

Figure 1-5 Various methods of pumping, [from left to right] a gear pump, centrifugal pump and magneto-hydro-dynamic pump. Images modified from [22], [92], [93].

Magneto-hydro-dynamic (MHD) pumping works through the Lorentz body force, which is induced in the fluid orthogonal to a magnetic field intersecting a direct current (DC) electric field (see Figure 1-5). This type of pumping only works with electrically conducting fluids such as liquid metals, but this is not necessarily a constraint – their high density makes them very effective inertial fluids. The MHD pump principle is applied in microfluidics and molten metal transport, so not many pumps exist yet for this application. Although this method is more difficult to model and control, it has no moving parts, and thus has no vibrations and a high reliability and lifetime in space. This pumping method has also been applied in the flown FDA-A6. Consequently, it can be argued that MHD pumping is the most suitable pumping strategy for space applications.

Other pumping methods could be used, but have limiting drawbacks. Piezoelectric pumping is low in power, but generally requires operating voltages of 100 V or more. Other methods with no moving parts are electrohydrodynamic, electroosmotic or electrochemical methods, but they produce a low flow rate and require operating voltages in the order of kilovolts. [29]

1.3.2 Performance Parameters

The utility of a fluid loop can be compared to the utility of a wheel actuator by comparing their common system-level performance parameters (PP) listed in Table 1-2. All PPs depend on the configuration of the actuator, so it is difficult to determine whether one actuator excels over the other generically. Nevertheless, some generalizing statements can be made by comparing the basic characteristics of a liquid pumped through a loop versus those of a wheel rotating on an axle. In addition, authors have proposed that a fluid loop has the potential to outperform a wheel in many areas; the most often proposed are highlighted in Table 1-1. The PPs in Table 1-2 with an asterisk will be of most interest in this dissertation.

Capability

One of a reaction wheel's most important PPs is the *angular momentum capacity*, and it is the product of the wheel's moment of inertia (MoI) and its angular velocity around an axis. Although the MoI of a liquid can be made arbitrarily large by increasing the radius and tube diameter of the loop, it is currently impossible for the pumped liquid to approach the angular velocity of the electric motors in wheel actuators. Hence, it seems that a fluid loop underperforms for very high angular momentum requirements. [22] Nevertheless, a fluid loop can be sized to match the angular momentum of a solid wheel within the same mass constraints and satellite envelope. [27]

Torque authority is another important PP and is proportional to the fluid's angular acceleration. The achievable torque is highly dependent on the type of pump and how effectively the pump can accelerate the fluid. Tests showed that a centrifugal pump can provide a high torque at the cost of high power consumption, whereas an MHD pump can achieve a torque of up to two orders of magnitude higher (!) than that of a similarly sized wheel at the same power consumption. [26], [27]

Table 1-2 The performance parameters of inertial attitude actuators. The PPs marked with an asterisk are of most interest in this dissertation.

	Performance Parameter	Also known as / indicator of
Capability	Angular momentum capacity*	Gyroscopic rigidity, momentum bias, passive resistance to disturbance torques, desaturation frequency
	Torque authority*	Agility, active resistance to disturbance torques
	Jitter	Vibrations, high-frequency angular motion, mass imbalance
	Accuracy	Pointing accuracy, control, angular deviation from target
	Range	Range of accuracy, manoeuvrability
Cost	Power consumption*	Efficiency, friction losses
	Mass*	Weight, moment of inertia
	Volume; shape*	Dimensions, geometric compatibility
	Design time	Ease of implementation, need for iterations, control design
	Price	Production cost
Reliability	Reliability	Predictability, risk, chance of failure, damage in case of failure
	Robustness	Structural integrity, shock resistance, launch load resistance
	Life time	Expected time until failure, wear-free operation
	Redundancy	Back-up, functionality in case of failure

Jitter is the high-frequency vibration caused by mass imbalances and the high rotation rate of a wheel. A fluid loop, on the other hand, can be very quiet – fluid has a continuous mass distribution over time and it runs smoothly through the tube at a lower velocity. However, a mechanical pump could still generate vibrations.

Accuracy is one of the biggest traits of inertial attitude actuators over other actuators, and is a main selection criterion. It is unknown how accurately a fluid loop can control the attitude of a satellite, but this will largely depend on the degree of control of the fluid velocity by the pump. This is complicated by the fact that direct, non-intrusive flow rate or velocity measurement is hard to achieve. [27] In addition, as opposed to wheels rotating around a fixed axle, it is possible that uncertainties in the geometry of the fluid loop reduce the knowledge of the distribution of the fluid's angular momentum. Advantages of the fluid loop include that there are no bearing stiction effects near zero RPM, and the reduced jitter also has a positive effect on the pointing accuracy. [25]

Cost

Power consumption is a major consideration for attitude actuators. Power in wheel actuators is consumed when accelerating the wheel, and to overcome mechanical friction and electromotive force (EMF) in the bearings and motor, respectively. Similarly, power in a fluid loop is consumed to accelerate the fluid and overcome mechanical and EMF friction in the pump. However, a fluid loop also has to overcome EMF in the fluid when it is conductive, and always has to overcome viscous friction in the fluid. Numerous authors claim that fluid loops would have advantageous power consumption, but this is mostly unsubstantiated. [11]–[14], [18] Power consumption depends heavily on the pumping strategy: where Nobari [26] found the power consumption inhibitively high with his centrifugal pump, Noack [27], [28] found the power consumption of his MHD-pumped fluid loop to be less than a similarly sized wheel. Regardless of the pumping strategy, viscous friction in the fluid *always* has a share in the power consumption of a fluid loop, but this has thus far been neglected or unreported. However, viscous friction in the fluid could play a major role when optimizing the actuator. In addition, it can be approached theoretically and it can be generically applied to any fluid loop. It is therefore a major point of interest in this dissertation.

The MoI (which indicates the effectiveness of the actuator) is proportional to its *mass*. However, mass is also a major cost on a system level, and should therefore be minimized while maximizing the MoI. The mass distribution of a wheel is physically constrained around the central axle, whereas the mass of a fluid loop can be concentrated in a tube as far away as

possible from the imaginary central axis of rotation. Locating the mass far away from the rotational axis greatly increasing the inertia, which consequently allows for minimal overall mass.

A reduction in fluid mass also implies a reduction in its *volume*. In addition, the volume of a fluid loop can be efficiently distributed over the satellite in any shape because the tube is not constrained to a physical axle. For instance, the small mass of a fluid loop can be distributed in a thin tube along the outer structure, whereas a heavy wheel takes up a large chunk of space inside the satellite.

In addition, a fluid loop is easy to scale, and could therefore reduce *design time* throughout the iterative design process of a space mission. When reconfiguring a wheel, it must be redesigned for new inertia, loads and vibrations, or a new commercial off-the-shelf (COTS) wheel must be identified, whereas the geometry of the tube of a fluid loop can easily be scaled or changed to meet the changing mission requirements.

Reliability

When considering the *reliability* of the fluid loop there are both advantages and disadvantages. The chance of actuator failure is low, because there are few or no moving parts that can sustain damage. This lack of moving parts also provides the fluid loop with wear-free operation, and hence an almost unlimited *lifetime* as opposed to the lifetime of a wheel that is limited by its bearings. [7]

The lack of moving parts and an even mass distribution also offers the fluid loop *robustness*; shocks and vibrations during launch and separation are distributed throughout the fluid instead of concentrated on the axle of a wheel.

However, the damages in case of failure could be disastrous. In case of a leak by a micrometeorite, broken seal or any other cause, the actuator completely loses its functionality and the conductive liquid in microgravity would jeopardize all other electronics aboard the satellite. Leakage could be accelerated by high on-orbit temperature differences that cause expansion pressure.

In addition, as opposed to a wheel that keeps spinning for a while when its motor stops, failure of the pump results in relatively quick drop in fluid velocity, unloading all present angular momentum and spinning up the satellite.

Another disadvantage of the fluid loop to mission designers is its lack of flight heritage: it is risky to choose an unproven technology that needs to be developed from scratch when there are a myriad of capable and flight-proven wheel-based actuators available.

1.4 Project Objectives

The above findings have led to the formulation of the main research question:

What is the fundamental potential of the fluid loop as an attitude actuator?

This question should be answered by fulfilling the following objectives:

1. Create a theoretical base and a design model for the first-order sizing and optimizing of a fluid loop, which relates the actuator´s input sizing parameters to the most important output performance parameters, taking viscous losses into account.
2. Create a worst-case external disturbance model as a function of spacecraft and mission parameters, so that the type of missions for which the fluid loop is suitable can be determined, and requirements can be formulated. This model must be applicable to the majority of present-day missions.
3. Design and develop a single-axis fluid loop prototype to validate the theoretical design model from objective 1 by characterizing the relation between the various input and output parameters.
4. Design and develop a spherical air bearing table to perform dynamic attitude control tests.
5. Analyse the test results and implement these in the theoretical design model from objective 1.
6. Draw conclusions and make recommendations on the fundamental potential of a fluid loop actuator.

1.5 Dissertation Layout

This dissertation is divided into six chapters.

This first chapter gives an introduction to attitude actuation and fluid attitude actuation. The literature and technology development are reviewed, the reported performance parameters of the fluid loops and wheels are discussed and compared, and the objectives and scope of this dissertation are set.

Chapter 2 discusses the fundamentals of attitude dynamics and fluid dynamics. It elaborates the theory and equations on which the sizing model is based: rotational motion, the orbital disturbance environment, sizing requirements, viscous friction losses and pumping.

Chapter 3 sets the requirements and constraints for the three developed products: the sizing model, the prototype and the spherical air bearing.

Chapter 4 presents a framework for the conceptual design and sizing of a fluid loop. It formulates the fundamental equations from chapter 2 specifically for a fluid loop.

Chapter 5 is a large chapter that encompasses all verification, validation and test (VV&T) activities of the three developed products. All hardware, measurement and test methods are described, followed by the verification of the theoretical sizing framework by fluid loop tests on both the table top and the air bearing. The model is then validated and tested by optimizing fluid loops for various satellite missions ranging from 1 kg to 3000 kg.

This leads to conclusions on the fundamental potential of fluid loop actuators, the limitations of this study and recommendations for future work.

2. Fundamentals of Attitude Actuation and Fluid Dynamics

This chapter presents the theory required for the conceptual design of a fluid loop. First, the fundamentals of attitude actuation are presented, addressing reference frames, rotational motion, how to quantify the disturbance environment, and how to set up actuator requirements based on this. Then, the fundamentals of fluid dynamics are discussed. Viscous friction is of major interest here, because 1) there is currently no framework for viscous energy losses in a fluid loop, and 2) the viscous friction is very dependent on the geometry of the fluid loop, making it an integral part of the fluid loop sizing and design process. The basic governing equations from this chapter are adapted and parameterized in Chapter 4 for efficient conceptual design and optimization of a fluid loop, accommodating for the iterations needed throughout the mission design.

2.1 Fundamentals of Attitude Actuation

Attitude is the three-dimensional orientation of a vehicle with respect to a specified reference frame. [7] This section discusses the basics of attitude actuation: rotational motion, a method for estimating the disturbance environment, and the sizing requirements for reaction and momentum wheels. It also addresses the assumptions made in this dissertation.

2.1.1 Reference Frames

A spacecraft in orbit always has 6 degrees of freedom (DoF). Attitude control is concerned with the 3 rotational DoF that describe the angular motion of a body, as opposed to the 3 translational DoF that describe rectilinear motion.

The systematic description of the rotation of a spacecraft is done with reference frames, as illustrated in Figure 2-1. Reference frames are located at a point of interest, such as the centre of the Earth or the centre of mass (CM) of a satellite, and can either be rotating or inertially fixed. Depending on the mission, the reference frame of a satellite can be inertially oriented (e.g. astronomy), Sun-oriented (e.g. heliophysics), or Earth-oriented (e.g. Earth observation and communication). Because the latter category comprises the vast majority of all space missions, this will be the scope for this dissertation.

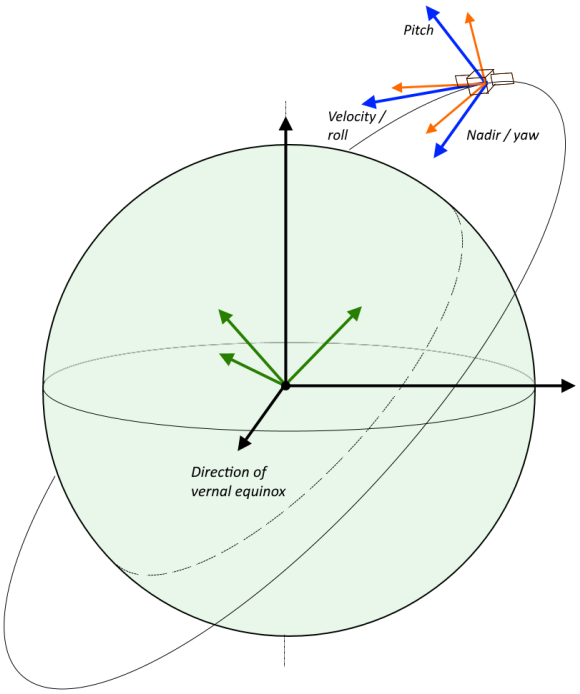

Figure 2-1 The reference frames of interest to an Earth-centred mission. See the text for a discussion of the axes depicted in this diagram.

The rotating *body frame* (orange) of a satellite is located at the CM of mass of the satellite, and its axes are aligned with the principal axes of the satellite – wherever the satellite is pointing, the body frame is pointing. Unless stated otherwise, in this dissertation the CM and geometric centre of the satellite coincide, and the satellite's principal axes align with the body frame axes. The rotational axis of any actuator under discussion also aligns with one of these axes.

The rotating *orbital frame* (blue) is also centred at the CM of the satellite, but its axes are aligned with the nadir and the velocity vector. For Earth-oriented missions, the attitude control on a satellite strives to align the body frame to the orbital frame during normal operation. The x, y and z axes of this frame are also known as the roll, pitch and yaw axes, respectively. For circular

orbits (which is assumed throughout this dissertation), the frame is rotating at the orbital rate Ω, with a tangential velocity v and a period T_{orbit}, as shown in equation 2.1, where μ is the standard gravitational parameter of the Earth. [30]

$$\Omega_{orbit} = \sqrt{\frac{\mu}{R_{orbit}^3}} \qquad v_{orbit} = v_{sat} = \sqrt{\frac{\mu}{R_{orbit}}} \qquad T_{orbit} = 2\pi\sqrt{\frac{R_{orbit}^3}{\mu}} \tag{2.1}$$

The Earth-centred, inertially fixed *perifocal frame* (green) is of interest when illustrating slew manoeuvres around the pitch axis. The *x* and *y* axes lie in the orbital plane, the former pointing in the periapsis direction, and the $\hat{z}$ axis is pointing perpendicular to this plane in the direction of the orbit's angular momentum. [31]

Finally, the *Earth-centred inertial frame* (ECI, black) has its *x* axis pointing towards the vernal equinox, the *y* axis perpendicular in the same equatorial plane, and the $\hat{z}$ axis aligned with the rotational axis of the Earth.

2.1.2 Rotational Motion

Inertial attitude actuators operate through the rotation and acceleration of an inertial mass, thus generating angular momentum and torque. The equations below describe the dynamics of rotation, and can be applied to both solids and fluids.

Moment of Inertia

The rotational analogue of mass is moment of inertia (MoI), and is a measure of resistance against angular acceleration. The MoI of a particle with mass m at a distance r around an axis is given by:

$$I = mr^2 \tag{2.2}$$

The complete rotational inertia of any given body can be expressed by an inertia tensor [Eq. 2.3]. In this dissertation, all bodies are assumed symmetric at the principal planes, so the products of inertia (PoI) that indicate uneven mass distribution become zero.

$$\hat{\boldsymbol{I}} = \begin{bmatrix} I_{xx} & I_{xy} & I_{xz} \\ I_{yx} & I_{yy} & I_{yz} \\ I_{zx} & I_{zy} & I_{zz} \end{bmatrix} \qquad \hat{\boldsymbol{I}}_{\boldsymbol{sym.}} = \begin{bmatrix} I_{xx} & 0 & 0 \\ 0 & I_{yy} & 0 \\ 0 & 0 & I_{zz} \end{bmatrix} \tag{2.3}$$

The MoI of a body about a principle axis z is calculated by adding up the MoIs of all infinitesimal particles, as shown in equation 2.4. [32] For most standard geometric shapes such as cylinders, rectangular prisms or rings, this can be simplified to a factored form of equation 2.2.

$$I_{zz} = \sum_{i=1,n}^{n} m_i r_{z,i}^2 = \int_o^m r_z^2 dm \tag{2.4}$$

Angular Momentum

Angular momentum H is the rotational analogue of momentum. External disturbances on a satellite can be resisted by transferring them into the angular momentum of a reaction wheel, or by the gyroscopic rigidity of a momentum-bias wheel. When considering the simplified case of a particle rotating around one axis through the CM at velocity $\boldsymbol{v}$ or angular velocity $\boldsymbol{\omega}$, the angular momentum vector $\boldsymbol{H}$ is obtained by:

$$\boldsymbol{H} = I\boldsymbol{\omega} = m\boldsymbol{v} \times \boldsymbol{r} \tag{2.5}$$

The magnitude of the particle's angular momentum vector can be obtained by using the velocity component perpendicular to the direction of the radius vector $v_\perp$, as shown in equation 2.6. [33]

$$|H| = I\omega = mv_\perp r \tag{2.6}$$

When considering a body (a collection of particles) rotating around an axis z that passes through with its CM, the magnitude of the angular momentum is the sum of the angular momentum of all particles around that axis. [33] This is what we are interested in for single-axis sizing purposes, and is given by:

$$|H_z| = \sum_{i=1,n}^{n} m_i v_{z,i,\perp} r_{z,i} = \int_o^m v_{z,\perp}^2 r_z dm \tag{2.7}$$

The total angular momentum of a satellite is the sum of its own angular momentum and that of all rotating objects inside the spacecraft, such as inertial attitude actuators.

$$\boldsymbol{H} = \hat{\boldsymbol{I}}\boldsymbol{\omega} + \boldsymbol{h}_{int} \tag{2.8}$$

Torque

Torque is the rotational analogue of force, and through it angular momentum can be exchanged between various components in the satellite, thereby generating or counteracting the satellite's rotation. Equation 2.9 gives various expressions of the torque on an imaginary axis related to the force $\boldsymbol{F}$ on, or the angular acceleration $\boldsymbol{\alpha}$ of, a particle rotating around that axis.

$$\boldsymbol{\tau} = \boldsymbol{F} \times \boldsymbol{r} \quad = m\dot{\boldsymbol{v}} \times \boldsymbol{r} \quad = I\boldsymbol{\alpha} \quad = I\dot{\boldsymbol{\omega}} \quad = \dot{\boldsymbol{H}} \tag{2.9}$$

In normal pointing mode, the rate of change of the satellite's attitude is governed by the external disturbance torques $\boldsymbol{\tau}_{ext}$ and the internal actuation torques $\dot{\boldsymbol{h}}_{int}$, under the assumption that there is no shifting mass or gyroscopic torque that alters the direction of the angular momentum. [7]

$$\hat{\boldsymbol{I}}\dot{\boldsymbol{\omega}} = \boldsymbol{\tau}_{ext} - \dot{\boldsymbol{h}}_{int} \tag{2.10}$$

2.1.3 Disturbance Environment

In order to size and design attitude actuators, the disturbance environment that they are expected to operate in should be determined. Although this environment consists of several highly predictable torques, it is difficult to pinpoint an accurate estimation due to the variable space environment and continuously changing mission design. Hence, an assumption-based worst-case scenario limited to external disturbance torques usually suffices during the earlier stages of the mission design and sizing process. [7] This section presents a simple method to quantify the worst-case disturbance environment for a large range of satellite design configurations.

To estimate the worst-case values, expressions from Wertz and Larson's Space Mission Engineering module are applied. [7] With the resulting torque values, a cyclic or secular worst-case angular momentum build-up can be acquired by integrating the worst-case torque over the time it takes to build up. This is then translated to actuator requirements in the following section.

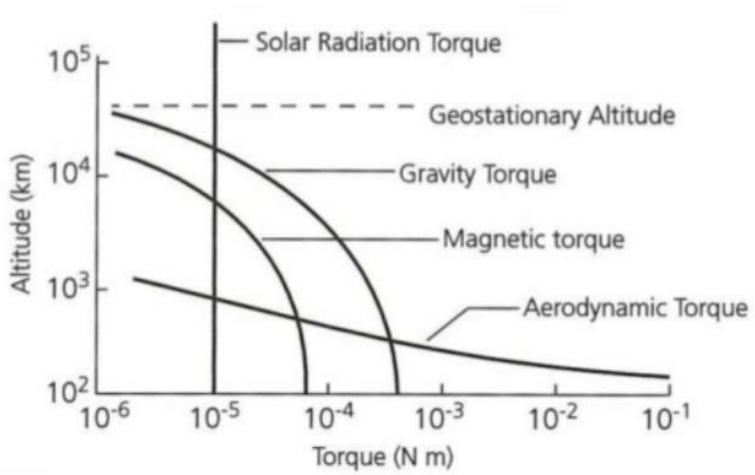

Figure 2-2 The variation with altitude of the major environmental disturbance torques on a satellite. The values are indicative, as this differs strongly per mission. [94]

The four major disturbance torques and their variation with altitude are shown in Figure 2-2. However, this graph is merely indicative – the actual values vary strongly with satellite and mission design. Hence, the following discussion is limited to Earth-oriented satellites in a circular orbit to obtain worst-case sizing values for the majority of missions. For computational simplicity, only the magnitudes (instead of vectors) of the torque and angular momentum around an arbitrary principal axis are considered. The variables are later parameterized for easy use during actuator sizing.

Solar Radiation Torque

Incident photons from the Sun impart miniscule amounts of momentum to the surface of a satellite. This results in a disturbance torque τ_{srp} if the resultant force is not aligned with the CM. For Earth-orbiting satellites the average is the same for all altitudes. For GEO satellites, this is the major disturbance component. A worst-case scenario illustrated in Figure 2-3 and the respective torque can be obtained with equation 2.11.

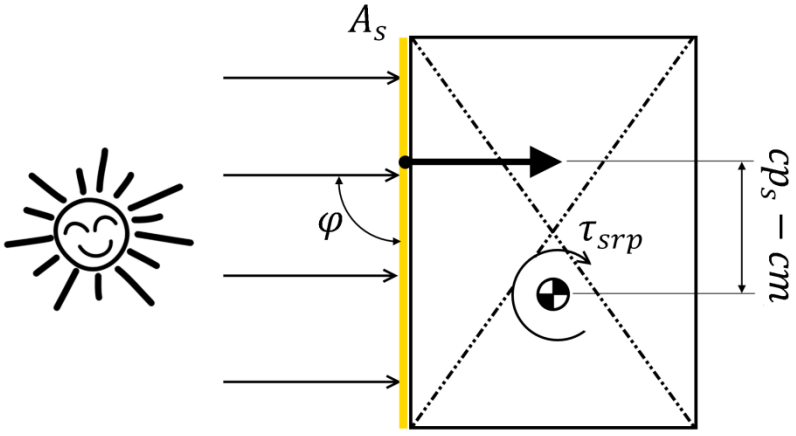

Figure 2-3 The conceptual working and variables of the worst-case solar radiation torque.

$$\tau_{srp} = \frac{\Phi}{c} A_s (1 + q)(cp_s - cm) sin\varphi \qquad 2.11$$

Where:

Φ	=	Solar constant (average of 1.366 W/m² at 1AU for Earth-orbiting satellites).
c	=	The speed of light ($2.998 \cdot 10^8$ m/s).
A_s	=	Largest sunlit surface of the satellite [m²].
q	=	Material-specific reflectance factor [–]. See Table 2-1 for typical reflectance values.
$cp_s - cm$		Offset of the centre of solar pressure from the CoM, perpendicular to incident rays.
φ	=	Sunlight angle of incidence with surface [rad/degrees]

Surfaces that reflect perfectly collect twice as much momentum from photons as perfectly absorbing surfaces. Table 2-1 gives reflectance factors for various materials. The direction of the resultant force also differs between the two cases: reflected photons push normal to the surface, whereas absorbed photons push parallel to incident sunlight. [34] This difference can be ignored in a worst-case scenario of perpendicular incidence.

Table 2-1 Reflectance factors of various materials. [35]

Material	Reflectance
Black paint	0.025
Solar cell (fused silica)	0.20
Titanium 6AL4V (polished)	0.55
Aluminium 606xT6	0.62
Goldized Kapton	0.75
Aluminium 606xT6 (polished)	0.8
Aluminized Teflon	0.84
Silvered Teflon	0.92

For Earth-oriented satellites the solar radiation torque can be assumed cyclic, resulting in a maximum angular momentum build-up after a quarter orbit. To obtain the angular momentum, the time integration is done by multiplying a quarter of the orbital period T_{orbit} by the root mean square of a sine-function, as will be done for some of the following cyclic disturbance torques too. [7]

$$H_{srp,max} = \tau_{srp} \frac{0.707\, T_{orbit}}{4} \tag{2.12}$$

Aerodynamic Torque

The few atmospheric molecules present at orbital altitude also impart momentum on the frontal surface of a satellite. Similar to how solar radiation torque is generated, an aerodynamic torque is generated when the resultant drag force is not aligned with the CM

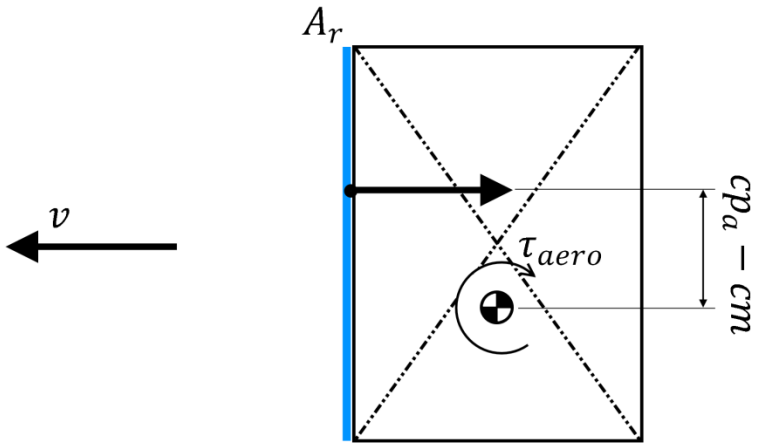

.

Figure 2-4 The conceptual working and variables of the (worst-case) aerodynamic torque.

$$\tau_{aero} = \frac{1}{2}\rho C_d A_r v^2 (cp_a - cm) \qquad 2.13$$

Where:

ρ `	=	atmospheric density [kg/m³]
C_d	=	drag coefficient (typically between 2 and 2.5 for spacecraft [7]) [–]
A_r	=	frontal area in the direction of the spacecraft velocity [m²]
v	=	velocity of spacecraft [m/s]
$cp_a - cm$	=	misalignment of centre of atmospheric pressure and CM [m]

The magnitude of the aerodynamic torque depends on the density of the upper atmosphere. Besides altitude, atmospheric density varies with temperature, which in turn depends on solar activity, geomagnetic field, latitude, the time of year and the time of day. [36] As a result, density values at a certain altitude can vary up to three orders of magnitude. [37]

There are numerous models that attempt to model the atmospheric density, but all are limited due to loss of accuracy over certain ranges. [38] For sizing purposes, however, an atmospheric model is only required to determine a worst-case order of magnitude. To this end, a simplified relation in Equation 2.14 between altitude and atmospheric density is obtained by a curve-fit on data points from an accurate and often-used atmospheric model, NRL-MSIS-E-00. [36], [38], [39]. It is taken during very high solar activity ($N_{10.7}$= 200), at the equator, at noon, on the day of the vernal equinox for a high atmospheric density. [40] The curve deviates in the order of ten percent from the data points in the range where aerodynamic drag is significant (300-1000 km altitude; derivation in Appendix 1). [41]

$$\rho = 1.714 \cdot 10^{6}\, h^{-6.575} \qquad 2.14$$

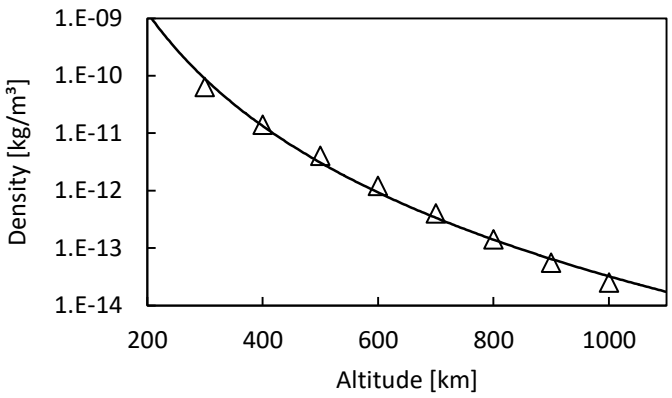

Figure 2-5 A simplified relation between atmospheric density and altitude, based on the NRL-MSIS-E-00 model at solar maximum ($\boldsymbol{N_{10.7}}$= 200) and high density conditions to obtain a worst-case value.

Earth-orbiting, Earth-pointing satellites experience a constant, secular aerodynamic disturbance torque resulting in a worst-case angular momentum build-up per orbit of:

$$H_{aero,max} = \tau_a\, T_{orbit} \qquad 2.15$$

Magnetic Torque

The residual magnetic moment present in magnetorquers and other parts of the satellite interact with the geomagnetic field, resulting in a disturbance torque that works to align the magnetic moment with the local magnetic field like a compass needle, as illustrated in Figure 2-6 and Equation 2.16.

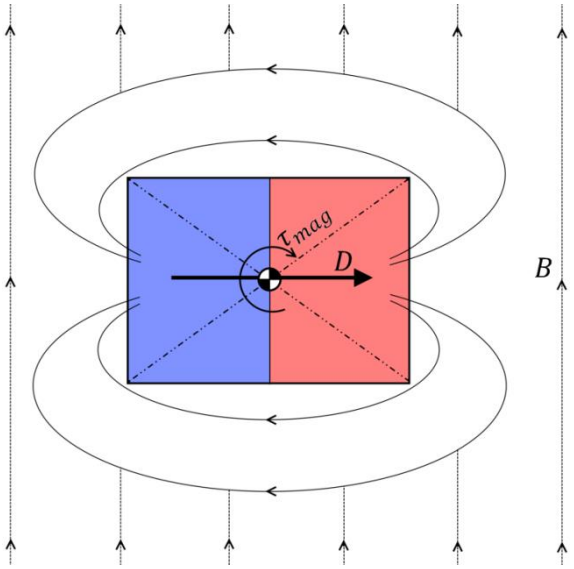

Figure 2-6 The conceptual working and variables of the (worst-case) magnetic torque.

$$\tau_{mag} = DB = D\left(\frac{M_{mag,earth}}{R_{orbit}^3}\lambda\right) \quad 2.16$$

Where:

D	=	the spacecraft's residual dipole moment [Am²]
B	=	the geomagnetic field strength [T]
$M_{mag,earth}$	=	product of the Earth's magnetic moment and magnetic constant (7.8E15 Tm³ [7])
R_{orbit}	=	Orbital radius [m]
λ	=	function of magnetic latitude (1 at magnetic equator, 2 at magnetic poles)

To obtain the magnitude of this torque for sizing purposes, assumptions must be made for the residual magnetism in the satellite and the geomagnetic environment. The geomagnetic field strength at the poles is roughly twice as high as at the equator, so a simple formula for the geomagnetic latitude λ as a function of orbital inclination i (between 0° and 180°) is used here.

$$\lambda = 1 + \sin i \quad 2.17$$

It must be noted that the geomagnetic field strength B can only be approximated as done in equation 2.16 for altitudes below approximately two Earth radii, rendering this equation valid only for LEO. [42] For the purpose of this dissertation this is justified by the fact that magnetic disturbances at geostationary altitudes are negligible. [43] This will be noted in the sizing model.

The residual magnetism D of the satellite is difficult to determine generically, because it depends on the design of the satellite and many other (time-dependent) factors. Values can range from very close to zero up to 20 Am². [7] In addition, values are not often published. [44] Nevertheless, to provide a handle in this sizing model, a relation is made between the satellite mass and its residual magnetic moment, based on the reported magnetic moments of various magnetically-uncompensated satellites (see Appendix 2 for derivation). Although this method should be considered a rough estimate at best and has few data points, it can be seen in Figure 2-7 that the trend line agrees well with the reported values.

$$D = 0.00441 m_{sat} \quad 2.18$$

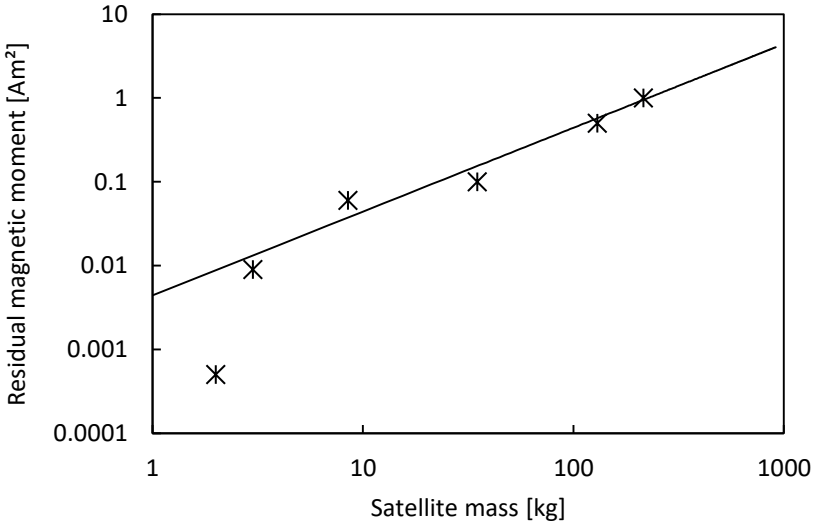

Figure 2-7 A generalized relation between a satellite's mass and its residual magnetic moment to help approach a realistic value for satellites of all sizes.

The angular momentum build-up due to magnetic disturbances for an Earth-orbiting, Earth-pointing satellite can be assumed cyclic, with a maximum build-up in a quarter orbit. [7]

$$H_{mag,max} = \tau_m \frac{0.707\, T_{orbit}}{4} \tag{2.19}$$

It should be noted that an MHD-pumped fluid loop could add to the satellite's magnetic moment due to the permanent magnets, or if the conducting fluid were to act as a current loop that induces a magnetic field. This could introduce complicated disturbance torques and an increase the overall magnetic disturbance torque, which would lead to an undesired increase in attitude control requirements.

Gravity Gradient Torque

The gravitational field of the Earth decreases as the inverse square of the distance from its centre. Consequently, the centre of gravity (CG) generally does not precisely coincide with the CM. The gravity gradient torque works to align the CG (which lies on one of the principal axes) and the CM with the local vertical. For nadir-pointing spacecraft, the gravity gradient torque can be very small because of the small deviation of the principal axis from the local vertical (~1°). [7] However, satellites for which the principal and pointing axis are not properly aligned, or satellites that perform slew manoeuvres are subjected to a higher gravity gradient torque.

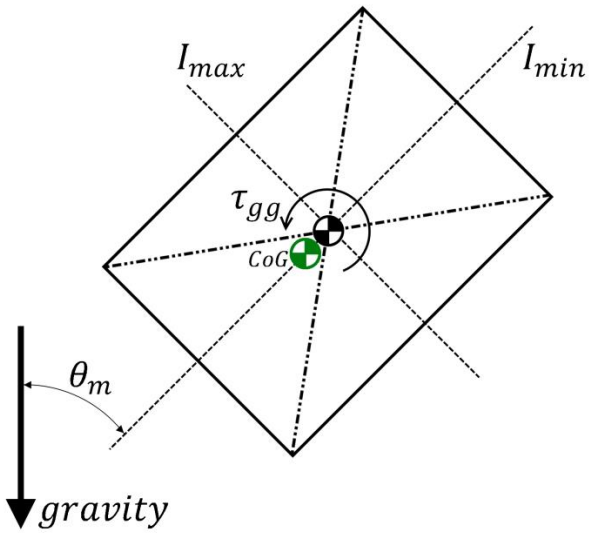

Figure 2-8 The conceptual working and variables of the (worst-case) gravity gradient torque.

$$\tau_{gg} = \frac{3\mu_{earth}}{2R_{orbit}^3}(I_{max} - I_{min})\sin(2\theta_m) \qquad 2.20$$

Where:

μ_{earth}	=	Earth's gravitational parameter (3.986 x10^14 m^3/s^2)
R_{orbit}	=	orbital radius [m]
I_{max}, I_{min}	=	maximum and minimum MoIs [kgm^2]
θ_m	=	angular deviation or mean slew angle of the satellite's principal axis from the local vertical [deg/rad]

The gravity gradient torque is constant for Earth-oriented satellites and results in a secular build-up of angular momentum. Slew manoeuvres result in a higher gravity gradient torque, so they should be accounted for in the angular momentum capacity requirements. It will be assumed here that slew manoeuvres are symmetric, so that the torque can be treated cyclic.

$$H_{gg,dev} = \tau_{g,nadir} T_{orbit} \qquad \text{(normal mode, secular)} \qquad 2.21$$

$$H_{gg,slew} = \tau_{g,slew} \Delta t_{maneouvre} \qquad \text{(slew mode, cyclic)} \qquad 2.22$$

2.1.4 Actuator Sizing Requirements

With the knowledge of the disturbance environment discussed in the previous section, torque and angular momentum requirements for an attitude actuator can now be formulated. In addition, the angular momentum requirement can be increased to reduce the wobble in a momentum-bias stabilized satellite (which is indicative of the pointing accuracy), and the torque requirement can be increased to accommodate slew manoeuvres.

Normal Torque Requirement

The worst-case total disturbance torque that acts on the satellite is obtained by adding up all individual worst-case torques [Eq. 2.23]. This is the torque that needs to be rejected by the actuator. Although this case would realistically never occur, it is a good starting point for actuator sizing. In addition, a margin is included in the control torque requirement to ensure proper disturbance rejection and accuracy [Eq. 2.24]. This is the control torque requirement in normal pointing mode, and often drives the actuator design. [7]

$$\tau_{ext,max} = \tau_{srp} + \tau_{aero} + \tau_{mag} + \tau_{gg} \tag{2.23}$$

$$\tau_{control} = \tau_{ext,max} * margin \tag{2.24}$$

Normal Angular Momentum Capacity Requirement

The angular momentum capacity of a reaction wheel determines after how many orbits n_{orbits} it needs to be desaturated, and thus the continuity of operation of the satellite. This is mainly dictated by the secular disturbance torques (aerodynamic and gravity gradient torques for Earth-oriented satellites), because they accumulate angular momentum over the course of an orbit. On top of that, there are the cyclic torques (solar radiation and magnetic torques for Earth-oriented satellites) that briefly build up angular momentum but cancel themselves out over the course of an orbit, and possible temporary momentums from slews.

$$H_{cap} = n_{orbits}\left(H_{aero,max} + H_{gg,max}\right) + H_{srp,max} + H_{mag,max} + H_{gg,slew} + H_{slew} \tag{2.25}$$

Angular Momentum Requirement and Allowable Motion of Momentum-Bias Wheel

The angular momentum requirement for a momentum wheel is calculated differently. Much like a spinning top, a momentum-bias stabilized satellite will precess at an angle around a central axis (often the pitch axis) when resisting a disturbance torque. The higher the angular momentum is, the lower the deviation from the desired axis. The relation between the required momentum and

the allowable angle of motion θ_a (in radians) is given by equations 2.26 and 2.27. This angle is directly related to the (roll and yaw) pointing accuracy of a momentum-bias system.

$$H_{bias} = \frac{\tau_{ext,max}}{\theta_a}\frac{T_{orbit}}{4} \tag{2.26}$$

$$\theta_a = \frac{\tau_{ext,max} T_{orbit}}{4H_{bias}} \tag{2.27}$$

Slew Manoeuvre Torque

When considering an Earth-oriented satellite, it is often required to perform a slew manoeuvre for ground target pointing or communication with a ground station, and more specifically around the pitch- or *y*-axis in the orbital reference frame. Slews require high torques, so this could drive the sizing process of attitude actuators.

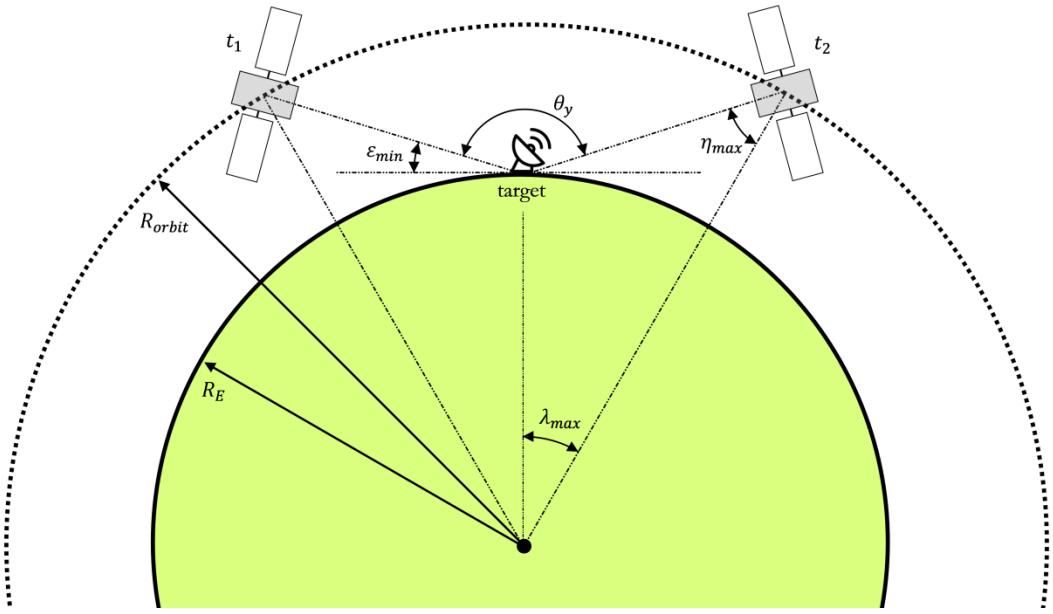

Figure 2-9 Perifocal top view of the orbital plane, describing the geometry of a symmetric target-pointing manoeuvre at the beginning (t1) and end (t2). The satellite is in a circular orbit and passes exactly over the ground-based target.

The actuator's torque requirement depends on the slew angle θ_y, the spacecraft's MoI around the slew axis I_y, and the duration of the manoeuvre Δt_{slew}. For both simplification and obtaining the worst-case required slew torque for the pitch axis, it is assumed that 1) the Earth is not rotating,

2) the pointing target on the Earth's surface passes directly underneath the satellite, and 3) the satellite is in a circular orbit. The torque requirement based on the slew manoeuvre without any resisting momenta from the other wheels is given by equation 2.28. [7]

$$\tau_{y,slew} = \frac{4\theta_y I_y}{\Delta t_{slew}^2} \tag{2.28}$$

To calculate the duration of the slew manoeuvre, equations 2.29 to 2.33 are given. [45] The slew angle θ_y is usually set as a requirement, but other requirements can also be given, such as the maximum off-nadir angle η_{max} or the effective horizon of the ground station ε_{min} (all should be computed in radians). Both the maximum slew angle and off-nadir angle are needed to calculate the slew duration, so they are expressed here in terms of one another, and the Earth's radius and orbital radius [Eq. 2.31 and 2.32].

$$\Delta t_{slew} = \frac{T_{orbit}}{180°}\text{acos}(\cos(\lambda_{max})) \tag{2.29}$$

Where:

$$\lambda_{max} = \tfrac{1}{2}\theta_y - \eta_{max} \tag{2.30}$$

$$\theta_y = 180° - 2\text{acos}\left(\left(\frac{R_{orbit}}{R_E}\right)\sin(\eta_{max})\right) \tag{2.31}$$

$$\eta_{max} = \text{asin}\left(\cos\left(\tfrac{1}{2}\left(180° - \theta_y\right)\frac{R_E}{R_{orbit}}\right)\right) \tag{2.32}$$

$$\varepsilon_{min} = 90° - \tfrac{1}{2}\theta_y \tag{2.33}$$

Finally, the total angular momentum change that builds up over half the slew period can be determined using equation 2.34. It cancels itself out over the course of the manoeuvre. This is then added to the total angular momentum requirement of the actuator in equation 2.25.

$$H_{slew} = \tau_{y,slew}\,\tfrac{1}{2}\Delta t_{slew} \tag{2.34}$$

2.2 Fundamentals of Fluid Dynamics

To complete the theoretical framework for sizing and optimizing a fluid loop, the dynamics of its inertial mass and its characterizing component, the fluid, should be described. The word *fluid* originates from *fluere*, the Latin verb for *to flow*. [46] Fluid dynamics studies the behaviour of flowing substances in motion – both gases and liquids. In the context of this dissertation, density and compressibility are the main differences between the two. Although it is expected that a dense, incompressible substance in the liquid state of matter will be used in the fluid loop, the term *fluid* will be used, because the liquid's most important and shared characteristic here is its ability to flow.

Flow and deformation of liquids and solids is studied in the field of rheology (similarly originating from the Greek word *rhéō* for *flow*). [47] A distinction to be made in this area is between Newtonian and non-Newtonian fluids, and is briefly addressed in the next section. In this dissertation only the linearly behaving Newtonian fluids are considered.

2.2.1 Basic principles

Density

An important intrinsic property of any substance is density or specific mass ρ, and is defined as mass per volume. However, often specific weight γ is used when describing terrestrial fluid systems. This is a non-intrinsic property and depends on the local gravitational acceleration. This is problematic for attitude dynamics in a microgravity environment, so it will not be used here. However, it is used as a conversion factor for terrestrial to universal fluid dynamics equations.

$$\rho = \frac{m}{V} \qquad \gamma = \frac{W}{V} = \frac{mg}{V} = \rho g \tag{2.35}$$

Viscosity

The absolute or dynamic viscosity μ is another important intrinsic property of a fluid and is a measure of resistance against flow. When two arbitrary layers of a fluid move relative to each other, resistive van der Waals forces cause a shear stress σ proportional to the absolute or dynamic viscosity and the velocity gradient $\frac{dv}{dy}$ (Eq. 2.36; Figure 2-10 in next section). This stress causes resistive friction forces and thus energy loss through heat dissipation.

Newtonian fluids behave according to Equation 2.36 and their viscosity is only influenced by temperature, whereas the viscosity of non-Newtonian fluids is also influenced by the velocity gradient.

$$\sigma = \mu \frac{dv}{dy} \tag{2.36}$$

The kinematic viscosity υ (Greek letter *nu*) is the ratio between the dynamic viscosity and density, and is sometimes referred to as momentum diffusivity [Eq. 2.37]. [48] It is a useful ratio when discussing the turbulence of a flow, and selecting a fluid for inertial attitude control.

$$\upsilon = \frac{\mu}{\rho} \tag{2.37}$$

Continuity and Energy

The continuity principle is a result of the law of conservation of mass, and means that the mass flow rate $\dot{m}$ at two points in a given continuous fluid system is always equal [Eq. 2.38]. When assuming an incompressible fluid, as is the case for the fluid loop, the density remains the same throughout the system. Consequently, the continuity of mass flow rate results in the continuity of volumetric flow rate Q. Flow rate is the product of the channel's cross-sectional area A and the fluid's average velocity v [Eq. 2.39, Figure 2-10 in next section].

$$\dot{m}_1 = \dot{m}_2, \qquad \dot{m} = \frac{dm}{\mathrm{d}t} = \rho \frac{dV}{\mathrm{d}t} = \rho A v \tag{2.38}$$

$$A_1 v_1 = A_2 v_2 \qquad Q_1 = Q_2 \tag{2.39}$$

Bernoulli's equation is a statement of the law of conservation of mechanical energy [Eq. 2.40]. It consists of the terms potential pressure energy, potential gravitational energy and kinetic energy per unit volume, respectively.

$$p_1 + \rho g z_1 + \tfrac{1}{2}\rho v_1^2 = p_2 + \rho g z_2 + \tfrac{1}{2}\rho v_2^2 \tag{2.40}$$

Bernoulli's equation does have some restrictions [49]:

1. It is only applicable to incompressible fluids;
2. It does not include energy transfer through heat;
3. It does not account for viscous friction energy losses;
4. It does not account for energy adding or removing devices in the flow path, such as pumps, obstructions or bends;

As an unintuitive result of Equations 2.39 and 2.40, when the cross-sectional area of the conduit decreases and the fluid velocity increases, the pressure in the fluid *decreases*.

Considering the fluid incompressibility in the case of the fluid loop, and considering that there will be no significant heat transfer because the pumped fluid will be assumed at ambient temperature, restrictions 1 and 2 can be disregarded. However, restrictions 3 and 4 do limit a realistic application of the equation in the case of the fluid loop.

Hence, to describe the energy balance of a fluid loop it is necessary to add terms for viscous friction energy losses in a straight tube (also called *major losses*) and friction losses due to devices in the flow path (also called *minor losses*). On the other hand, pumps add energy to the system to overcome these friction losses, and should also be accounted for. These topics are discussed in the following sections, and they are subsequently added to Equation 2.40.

2.2.2 Major Viscous Losses

Energy loss in a pipe can be seen as the conversion of useful pressure energy into useless heat by viscous friction between layers of fluid moving at different velocities. Consequently, viscous friction losses in a pipe can be expressed as a pressure drop. Because the pressure drop in a fluid loop is overcome by the pump, the pressure drop is proportional to the power consumption of the fluid loop – a major cost for satellite components.

The fluid loop is exclusively concerned with flow in full pipes, so there is no liquid-gas interface that can cause sloshing. However, the fluid-wall interface does result in a no-slip condition: the arbitrarily small layer of fluid that is in contact with the wall moves at the same speed as the wall. As a result, the fluid velocity at the wall is zero, while it is at its maximum in the centre. As mentioned in Section 2.2.1, The viscosity of the fluid causes the slower layers to pull or mix with the faster layers and vice versa, causing a shear stress, proportional to the velocity gradient [Eq. 2.35, Figure 2-10].

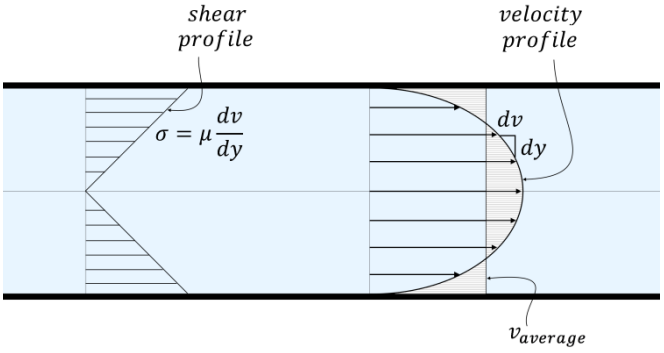

Figure 2-10 The parabolic velocity profile of a laminar flow in a pipe. The shear stress that causes viscous energy loss is proportional to the viscosity and velocity gradient. Turbulent flow has a more stub-nosed velocity profile, but an equal average velocity under continuity.

Laminar Flow

Laminar flow is an orderly layered flow. Figure 2-10 shows the velocity and shear profiles for laminar flow in an ideally long pipe. In case of the fluid loop, the pipe cannot always be considered ideally long. For instance, at the entrance region of a pipe, the velocity profile takes a different shape resulting in increased friction. The same applies to flow after obstructions or other irregularities. This should be taken into account when analysing test results. For an idealized, fully developed laminar flow, the pressure drop over a length of pipe of L with a diameter d can be calculated with the Hagen-Pouiseuille equation [Eq. 2.41].

$$\Delta p = \frac{32\mu L v}{d^2} \qquad 2.41$$

Turbulent Flow

Flow can also be turbulent instead of laminar. Turbulence causes increased friction and thus more pressure energy losses. The velocity profile from Figure 2-10 changes from parabolic to stub-nosed, but in the same system the surface under the graph (mean velocity) stays the same under continuity. To determine whether a flow is turbulent, the Reynolds number N_r can be calculated by Equation 2.42, where d is the channel diameter. Note to differentiate between the fluid velocity v in the numerator and the kinematic viscosity υ (Greek letter *nu*) in the denominator. The Reynolds number can be seen as the ratio of the inertial forces to the viscous forces of a fluid.

$$N_r = \frac{vd\rho}{\mu} = \frac{vd}{\upsilon} \qquad 2.42$$

In general:

$N_r < 2300$ = Laminar flow;

$2300 \leq N_r \leq 4000$ = Transition zone;

$N_r > 4000$ = Turbulent flow.

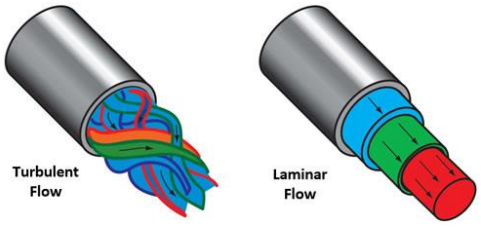

Figure 2-11 Turbulent and laminar pipe flow.

The pressure drop loss in the chaotic turbulent flow is more difficult to predict, but the Darcy equation [Eq. 2.43] can be used to obtain an accurate solution. This equation can also be used for laminar flow, and will therefore be used throughout the dissertation.

$$\Delta p = \frac{f \rho L v^2}{2d} \tag{2.43}$$

Friction Factor

Darcy's equation requires an empirically determined friction factor f. For laminar flow, the friction factor is simple and only depends on the Reynolds number, namely $f = \frac{64}{N_R}$. Entering this into Equation 2.43 results in the simple Equation 2.41. For turbulent flow, however, the friction factor is non-linear, different per situation and is catalogued empirically by many tests. The roughness of the wall relative to the diameter of the pipe ε/d also plays a role here.

The most accurate way of analytically determining the friction factor is via the implicit Colebrook equation, which requires an iterative approach because of the occurrence of f on both sides of the equation. This approach will not be used here for computational ease later in the project. Instead, the most accurate explicit approximations made by Swamee-Jain [Eq. 2.44] and Serghide [Eq. 2.45] will be used. The latter method has a maximum deviation of only 0.0031% from the original Colebrook equation. [50] The Moody diagram (Fig. 2-12) gives a graphic overview and method for determining the friction factor.

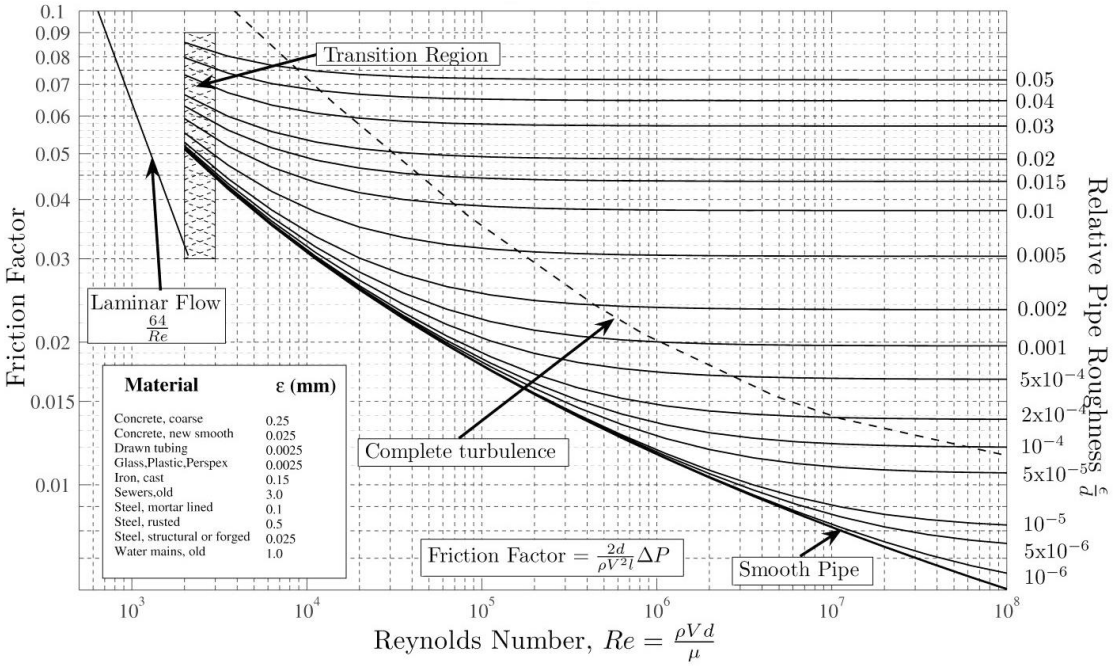

Figure 2-12 The Moody diagram shows the friction factor as a function of the Reynolds number and the relative pipe roughness. [51]

$$f = \frac{0.25}{\left(\log\left(\frac{\varepsilon}{3.7d} + \frac{5.74}{N_R^{0.9}}\right)\right)^2} \tag{2.44}$$

$$f = A - \left(\frac{(B-A)^2}{C - 2B + A}\right)^{-2} \tag{2.45}$$

Where:

$$A = -2\log\left(\frac{\varepsilon}{3.7d} + \frac{12}{N_R}\right)$$

$$B = -2\log\left(\frac{\varepsilon}{3.7d} + \frac{2.51A}{N_R}\right)$$

$$C = -2\log\left(\frac{\varepsilon}{3.7d} + \frac{2.51B}{N_R}\right)$$

Channel Cross-Section

The fluid dynamics equations in the above sections that include the pipe diameter d apply to a circular cross-section. For differently shaped cross-sections the same equations can be used, but d should be replaced by the hydraulic diameter d_h. This is obtained by Equation 2.46, where A is the cross-sectional area and per is the wetted perimeter of the cross-section. [52] For a rectangular cross-section, this results in:

$$d_h = \frac{4A}{per} = \frac{2wh}{w + h} \tag{2.46}$$

2.2.3 Minor Viscous Losses

The other category of energy losses result from irregularities and obstructions in the pipe flow caused by pipe enlargements, contractions, valves, pipe bends and other components. These losses are called minor, because in conventional terrestrial pipe systems they contribute less to the total energy losses than the viscous losses from the previous section. Because of the small scale of this project, this may well turn out the other way.

Because of the wide variety of components, there is a general notation for minor energy losses whereby velocity v stands for the velocity in the smallest pipe diameter [Eq. 2.47]. Similar to the

friction factor, K is the component-specific, empirically determined resistance coefficient, also known as the K-factor. [49]

$$\Delta p = \frac{1}{2}\rho K v^2 \qquad 2.47$$

Pipe Bends

The total friction in a pipe bend is higher than that of a straight pipe with the same length, and is comprised of three parts. The first part is the regular major loss over the length of the bend, as discussed in the previous section. The second part is losses by secondary flow due to two counter-rotating vortices perpendicular to the main flow direction, caused by centrifugal force. The third part is due to the separation of the main flow from the inner and outer radius of the bend (see Figure 2-13). [53] The "tightness" or curvature of the bend, or more specifically, the radius of the bend relative to the diameter of the pipe $\frac{R}{d}$, is a major factor here.

There are many methods to determine the bend loss, and the observations and proposed methods vary widely. [54], [55] In addition, the tests on which they are based are done only with 4-centimetre diameter pipes and larger – far from the envisaged fluid loop pipe diameter. [56] Moreover, bends can influence the flow to up to 50 pipe diameters after the bend. [57] This complicates a theoretical approach for these types of losses in the fluid loop. However, determining the corner losses must be done since the fluid loop can also take the shape of a rectangular loop. Two methods are given below for use in this dissertation.

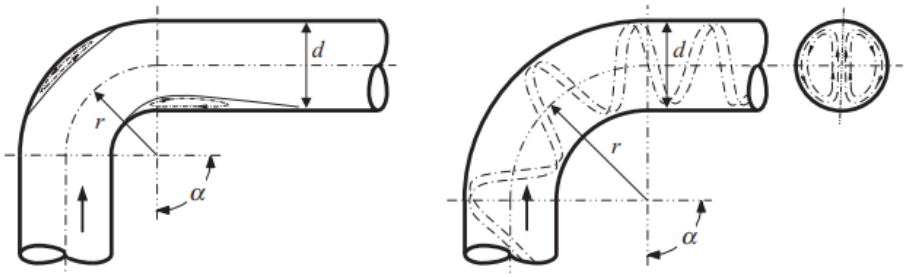

Figure 2-13 Two types of flow distortion in a bend that increase the friction loss in the pipe. [53]

One of the more universally applicable methods is proposed by Rennels and Hudson, based on observational data from various authors and applicable to all relative bend radius values. [53] It depends on the friction factor f, and has terms for all three components of the bend friction discussed above. For smooth-walled bends, K_{bend} is given by Equation 2.48, where α is the bend

angle ($0 < \alpha < \pi$). For sharp elbow bends of 90° without any rounding, the same authors propose $K_{elbow} = 1.20$. Both agree well with previous observational data of turbulent bend flows. [53] For laminar flows, it might be necessary to adjust the friction factor.

$$K_{bend} = f\alpha\frac{R_{corner}}{d_h} + (0.10 + 2.4f)\sin\frac{\alpha}{2} + \frac{6.6f\left(\sqrt{\sin\frac{\alpha}{2}} + \sin\frac{\alpha}{2}\right)}{\left(\frac{R_{corner}}{d_h}\right)^{\frac{4\alpha}{\pi}}} \quad 2.48$$

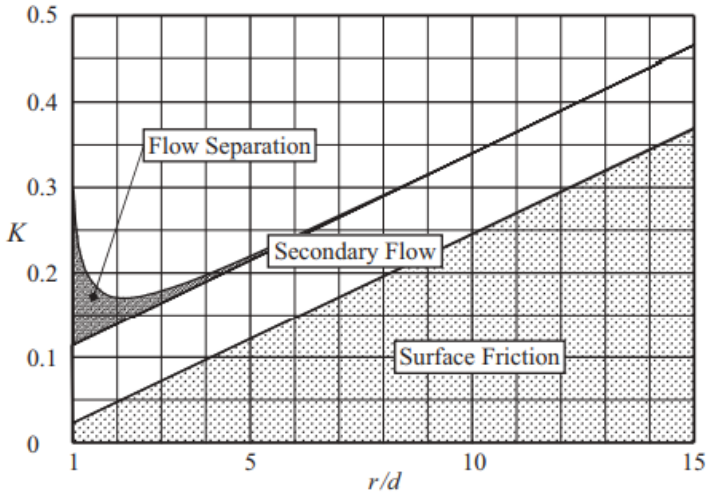

Figure 2-14 Visualization of the three components of the bend resistance coefficient as a function of the relative bend radius for a given friction factor. [53]

Helix Tube

Like bends, helixes or coils also induce counter-rotating vortices, but keep them going due to their constant curvature. The fluid loop in its circular configuration also has a constant curvature, regardless of the number of coils. Consequently, a coiled tube could prove to be a better model for the fluid loop than a straight or elbowed tube. Based on Equation 2.48, Rennels and Hudson propose an equation for determining K_{helix}, which treats the whole helix as one minor energy loss component [Eq. 2.49]. [53] The flow separation term is disregarded here, because this does happen over and over in a constantly-curved helix.

$$K_{helix} = N_{coils}\left(f\frac{\sqrt{(2\pi R)^2 + {d_{pitch}}^2}}{d_h} + 0.20 + 4.8f\right) \quad 2.49$$

A second method for determining the viscous friction in a coiled tube comes from Jove, and gives a Darcy friction factor f based on the Reynolds number and Dean number N_d – a measure for the tightness of a pipe bend [Eq. 2.50]. [58]

$$N_D = N_R \sqrt{\frac{d_h}{D}} \tag{2.50}$$

$f = \frac{64}{N_R}$ For wide curvatures $(N_d < 11.6)$;

$f = \frac{\frac{64}{N_R}}{1-\left(1-\left(\frac{11.6}{N_D}\right)^{0.45}\right)^{2.2}}$ For medium curvatures $(11.6 \leq N_d \leq 2000)$;

$f = \frac{7.0144}{N_R}\sqrt{N_D}$ For tight curvatures $(N_d > 2000)$.

Expansions and Contractions

When there is a sudden expansion or contraction in the pipe, the resistance coefficient depends on the ratio between the minor and major diameter, the cone angle, and the corner radius of the pipes to the cone. Generally speaking, the more gradual the change, the less the friction. However, if the change is too gradual, there is also a longer stretch of pipe the fluid must move through, resulting in larger major losses. For expansions the sweet spot lies around 7°, whereas the sweet spot for contractions lies anywhere between 15° and 40°. [49], [57] This type of loss is more intuitive and easy to prevent, but should nevertheless be taken into account when designing a fluid loop.

2.2.4 Pumping and Power Consumption

A pump propels the inertial mass of a fluid loop by adding kinetic and pressure energy. The viscous losses in the fluid loop described in the previous sections result in a pressure drop that, at a constant flow rate, is *always* compensated by an equal pressure addition from the pump.

$$\Delta p_{loss,total} = \Delta p_{add,pump} \tag{2.51}$$

This pressure is generated by transferring hydraulic work or power P_{hydro} from the pump's blades onto the fluid. This is the useful output power of the pump. [59]

$$P_{hydro} = \Delta p Q \tag{2.52}$$

Because the (hydraulic) power consumption is a function of the pressure drop in the fluid loop, it can be linked to the fluid dynamics equations above. For instance, the mechanical power required to pump a fluid through a given straight pipe is obtained by inserting Equation 2.43 into 2.52 [Eq. 2.53]. The term Δp can also be substituted by other pressure drop equations, resulting in the power consumption for that particular piece of pipe or component.

The hydraulic power can then further be related to the electrical input power P_{in} by Equation 2.54 and the pump efficiency η. This ratio varies strongly per pump and other characteristics of the fluid system, such as flow rate, pressure difference and fluid characteristics. [60] Nevertheless, this gives a relation between viscous fluid friction and electrical power consumption. This allows for optimization of the hydraulic power component by changing the loop geometry and fluid characteristics, within the limits of the pump capabilities and customer requirements. This principle is used for optimizing a fluid loop.

$$P_{in} = P_{hydro} + P_{pump\ losses} \tag{2.54}$$

$$= P_{hydro} + \{P_{pump\ mech\ friction} + P_{pump\ viscous\ friction} + P_{pump\ electrical\ losses}\}$$

$$\eta = \frac{P_{hydro}}{P_{elec,in}} \tag{2.55}$$

$$P_{in} = \frac{\Delta pQ}{\eta} \tag{2.56}$$

With this, the Bernoulli energy balance from Equation 2.40 can now be formulated for any two points in a fluid system, including the major and minor viscous losses, and the pressure addition by a pump [Eq. 2.56 and 2.57]. Point 2 should always lie downstream from point 1.

$$p_1 + \rho g z_1 + \frac{1}{2}\rho v_1^2 + \sum \Delta p_{pumps} - \sum \Delta p_{major\ losses} - \sum \Delta p_{minor\ losses} = p_2 + \rho g z_2 + \frac{1}{2}\rho v_2^2 \tag{2.56}$$

In case of the closed fluid loop, this works to describe the complete system when these points are chosen adjacent to one another. As is assumed throughout this dissertation, the gravity and velocity terms cancel out if the chosen points in the fluid system have the same height and cross-sectional area. This results in the general statement for the fluid loop, similar to Equation 2.51.

$$\{p_1 - p_2\}_{adjacent} = \sum \Delta p_{pumps} - \sum \Delta p_{major\ losses} - \sum \Delta p_{minor\ losses} = 0 \tag{2.58}$$

3. Requirements and Constraints

The three products that are developed by the author in this dissertation are:

- A generically applicable parametric **sizing model** for the conceptual design and optimization of a fluid loop;
- The mechanical design and development of a configurable **fluid loop prototype** to verify the sizing model;
- The design of a spherical **air bearing table** for dynamic frictionless attitude tests.

The objectives, high-level functions, requirements and constraints are set out in this chapter to ensure that each of these products appropriately fulfil their functions.

This Chapter is structured as follows. In Section 3.1 the requirements validation process is discussed. The subsequent sections of the Chapter describe the requirements and constraints for the fluid loop sizing model (Section 3.2), the fluid loop prototype (Section 3.3), and the air bearing (Section 3.4).

3.1 Requirements Validation

The validation of requirements is done to ensure that all stakeholders and end users agree on the system that is to be designed. The review team consisted of the supervisor and developers of the system: Johan Joubert (NSS engineering manager), Rudi Glatthaar (NSS electrical engineer), and the author (mechanical engineer). During the discussions, the requirements were checked for comprehensibility, redundancy, completeness, ambiguity, consistency, organisation, and conformance to standards. [61] Based on the points that came forward in the meeting, they were clarified, missing information was added and conflicting or interwoven requirements were

disentangled. The revised and validated requirements are listed in the following sections. The most important revisions are as follows.

- For the sizing model, the input values were initially limited to the fluid loop design parameters. An additional input section for "customer requirements" was added, so that the performance parameters of the fluid loop could be compared to and optimized for the desired values.
- A distinction is made between the new requirements-driven mode and the originally envisaged capability-driven mode for the model. The requirements-driven mode should allow for optimizing certain values such as angular momentum, power consumption or mass within the limits of specified requirements and budgets.
- The capability-driven mode formulates customer requirements based the orbital disturbance environment, calculated from mission and satellite parameters. This can be used to find out for what kind of missions a fluid loop would be suited. It was found that this mode increases the utility of the model significantly.

3.2 Requirements and Constraints for the Sizing Model

3.2.1 Objectives

1. To quantify the most important sizing relations for a fluid loop.
2. To identify for what type of missions a fluid loop is well-suited.
3. To accelerate the conceptual design process of a fluid loop.

3.2.2 High-Level Functions

1. Calculate fluid loop Performance Parameters (PPs) from the input design parameters.
2. Calculate disturbance rejection requirements and slew requirements from the satellite parameters and mission parameters.
3. Suggest fluid loop configurations and dimensions based on user-specified requirements.
4. Allow for quick comparison of PPs and requirements design iterations.

3.2.3 Requirements

All requirements are verifiable by demonstration of the spreadsheet *and* by measurements during tests with the prototype on either a table top or air bearing.

SM-1. The model should be as generically applicable as possible, i.e. to fluid loops of the following shapes:

a. Circular
b. Square (with sharp or rounded corners)
c. Helical/coiled

SM-2. The model should retain its functionality irrespective of the pumping method.

SM-3. The model should have a parametric *requirements-driven* mode and a parametric *capability-driven mode*.

SM-4. The model should calculate the following fluid loop performance parameters (PPs) **(output)**

a. Angular momentum capacity
   i. With a maximum deviation of ±20% from the measured values in tests.
b. Torque authority
c. Mechanical power consumption due to viscous friction
d. Electrical power consumption of fluid loop (at an assumed pumping efficiency)
e. Pressure drop over the pipe due to viscous friction
   i. With a maximum deviation of ±20% from the measured values in tests.
f. Fluid mass
g. Fluid volume
h. Mass of fluid loop
i. Pointing accuracy of momentum wheel (if applicable)

SM-5. The model should allow for specifying the following fluid loop design parameters **(input)**:

a. Shape
   i. Circular/square loop
   ii. Circular/rectangular channel cross-section
b. Dimensions
   i. Loop diameter
   ii. Channel diameter
   iii. Corner radius (if applicable)
c. Number of coils
d. Pump properties
   i. Flow rate
   ii. Flow rate acceleration
   iii. Maximum pressure differential

iv. Overall electrical efficiency
v. Mass

e. Pipe properties
   i. Surface roughness
   ii. Mass per unit length

Requirements-Driven Mode

The requirements-driven mode can be used to find a suitable fluid loop configuration based on customer requirements. It can also be used to compare the fluid loop's performance to conventional reaction wheel performance, by setting the customer requirements to the reaction wheel's performance values.

SM-6. The model should allow for the customer requirements **(input)** to be set:
   a. Angular momentum capacity requirement
   b. Torque requirement
   c. Power budget
   d. Mass budget
   e. Volume budget/allowable outside dimensions

Capability-Driven Mode

The capability-driven mode is used to (1) formulate requirements in the absence of customer requirements, and (2) to identify for what missions a fluid loop could be well-suited.

SM-7. The model should estimate the actuator's disturbance rejection and slew requirements **(output)** in terms of:
   a. Angular momentum capacity
   b. Torque authority

SM-8. These disturbance rejection and slew requirements [req. 7] should be based on:
   a. The orbital disturbances environment [req. 10 and 11].
   b. Satellite parameters [req. 9]
   c. The allowable accuracy/angle of precession of the momentum wheel (If the fluid loop is used as a momentum wheel)

SM-9. The model should take into account, and allow for specifying the satellite parameters **(input)**:
   a. Length, width, height
   b. Mass

SM-10. The model should allow for specifying the mission parameters **(input)**:
   a. Orbital altitude

b. Orbital inclination

SM-11. The model should allow for the input of environmental disturbance parameters **(input)** (assumed, informed by the findings from Section 2.1.3):

a. Area of externally mounted solar arrays
b. Reflectance coefficient; centre of solar pressure offset
c. Drag coefficient; centre of aerodynamic pressure offset
d. Angular deviation between principal and pointing axis

3.2.4 Constraints

1. The model is only applicable to one axis.
2. The model is only applicable to Newtonian fluids.
3. The disturbance rejection and slew requirements are only applicable to Earth-orbiting, Earth-pointing satellites.
4. The disturbance rejection and slew requirements are only applicable to satellites in a (near) circular orbit.
5. The disturbance rejection and slew requirements are only applicable to satellites with the shape of a cube/rectangular prism.
6. The disturbance rejection and slew requirements are only applicable to satellites with a homogeneous mass distribution.
7. The environmental disturbance torques are based on many educated assumptions and simplified equations, so they lack in accuracy. Hence, this part of the model only serves for getting an order of magnitude for the actuator requirements.

3.3 Requirements and Constraints for the Fluid Loop Prototype

3.3.1 Objectives

1. To verify and validate the developed design model described above, with special attention to the unknown factors:
    a. Pressure drop in the loop due to viscous friction;
    b. The influence of the loop shape on the PPs.
2. To experience the design and development process of a fluid loop.
3. To experience the functioning of a fluid loop.

3.3.2 High-Level Functions

1. Contain fluid

2. Propel fluid
3. Vary loop geometry
4. Vary flow rate
5. Measure flow rate
6. Measure pressure drop in loop
7. Measure pump power consumption
8. Measure angular position/velocity/acceleration (when on air bearing)

3.3.3 Requirements

FL-1. The default fluid loop should fit in a 20×20×20 cm^3 box.

FL-2. The mass of the assembly should not exceed 1.5 kg.

FL-3. The prototype should allow for changing the loop geometry/input design parameters as listed in Requirement SM-5 (except for channel roughness, helix pitch and channel mass).

a. Reconfiguration time should be minimized.

b. The various configurations should be reproducible.

FL-4. The pump should produce a flow rate of at least 0.5 L/min to ensure significant results.

FL-5. The flow rate should be measured or deducible from other measurements.

a. With an accuracy of ±5%.

FL-6. The pressure drop in the loop should be measured or deducible from other measurements.

a. With a range equal or bigger than the operating pressure of the pump.

b. With an accuracy of ±5%.

FL-7. The power consumption of the pump should be measured.

FL-8. The fluid loop should have no leaks.

FL-9. The fluid should not contain visible bubbles.

FL-10. The prototype should include a robust, reusable filling mechanism.

FL-11. The prototype should include a pump priming mechanism (if required by the pump).

FL-12. The prototype mounting plate should interface physically with the air bearing.

FL-13. Measurements during tests on the air bearing should be done without physical contact to eliminate disturbance forces.

3.3.4 Constraints

1. It is expected that the flow path is not an ideal pipe of the desired actuator shape, due to the need for a filling mechanism, bends, measurement ports, etc. This results in unknown viscous friction/pressure drop that cannot be approached analytically. Consequently, this

friction should be empirically determined by tests and subtracted from the measured pressure drop over the fluid loop in the complete setup.

2. The flow in the prototype is not analysed using computational fluid dynamics software, which limits the knowledge of the flow inside the loop (for instance on velocity profiles, local turbulence, and component-specific pressure drop).
3. Only circular channels are used for ease of procurement.
4. Only mechanical pumps are considered for ease of procurement.

3.4 Requirements and Constraints for the Air Bearing

3.4.1 Objectives

1. To perform dynamic attitude tests with near-zero friction to simulate the orbital environment.
2. To obtain the angular momentum and torque produced by a fluid loop.

3.4.2 Functions

1. Provide rotational freedom at near-zero friction in the 3 DOFs.
2. Allow for adjustment of CG position of moving assembly.
3. Measure angular position/velocity/acceleration of rotating assembly.
4. Provide a stable and ergonomic position for the air bearing.

3.4.3 Requirements

AB-1. The rotating assembly should have 360° of freedom around the z-axis of the static frame in the centre of rotation (CR).

AB-2. The rotating assembly should have at least ±15° of freedom around the x- and y-axes of the CR frame.

AB-3. The rotating assembly should be rotationally symmetric around the vertical z-axis of the CR frame.

AB-4. The CG of the rotating assembly should be adjustable to coincide with the centre of rotation (CR).

AB-5. The CG of the rotating assembly should be adjustable to coincide with z-axis of the CR frame, i.e. be balanced so that the top plane of the rotating assembly is horizontal.

AB-6. The CG position should be reproducible for other tests.

AB-7. The CG position should be able to be at least 5 cm below the CR, in order to provide a long enough pendulum (potential energy well) for tests around the z-axis. This limits angular deviation from the vertical at an uneven/assymetric mass distribution of the item under test.

AB-8. The angular motion of the assembly on the spherical air bearing should be measured or deducible from other measurements.

a. Angular velocities
    i. With an accuracy of ±5%.
b. Angular accelerations of 0.01 deg/s² or smaller.
    i. With an accuracy of ±5%.
    ii. At a frequency of 10 Hz or faster.
    iii. Measurements must be logged automatically.

AB-9. The air bearing table must be able to carry 20 kg.

AB-10. The top plane of the air bearing should be at a height between 90 and 110 cm.

AB-11. The base should be able to carry 50 kg.

AB-12. The base should be stable, i.e. it should not tip under a horizontal force at the top of at least 100 N.

AB-13. An accidental kick against the base should result in a hurting toe, rather than the air bearing and item under test falling on the floor (arbitrary but clear).

AB-14. The base should allow for changing a small air bearing that is meant for testing the fluid loop and other smaller components [req. 8] for a larger air bearing with a carrying capacity of 50 kg.

AB-15. The air bearing table should be electrically grounded.

AB-16. The air bearing table should be RoHS-compliant for use in a clean room.

3.4.4 Constraints

1. The CG coincidence with the z-axis must be determined with a bulls-eye spirit level.
2. The CG position must be adjusted manually.
3. The motion of the rotating assembly must be manually halted before each test.

4. Sizing a Fluid Loop

The scalability of a fluid loop is fully expressed in the sizing and conceptual design process. For instance, a small square fluid loop for a 1U CubeSat has the same basic components as a helical fluid loop for a 4-tonne GEO satellite – a pump, a tube and a fluid. Of course, the actual used components will most definitely vary between the two given examples. Nevertheless, the entire conceptual design of the fluid loop can be defined in terms of their basic shared characteristics (pump capabilities, tube geometry, fluid properties), further referred to as the input design parameters (listed in Requirement SM-5). Based on the fundamental equations in Chapter 2, these design parameters are equated to the performance parameters (PPs) of the fluid loop. This is then brought together into a user-friendly spreadsheet that allows for quick calculations and iterations, so that the scalability of the fluid loop is fully exploited. This chapter shows how this is done. Because the approaches are slightly different for each configuration, a distinction will be made between a circular, square or helical fluid loop. Figure 4-1 illustrates the different configurations and their geometric design parameters.

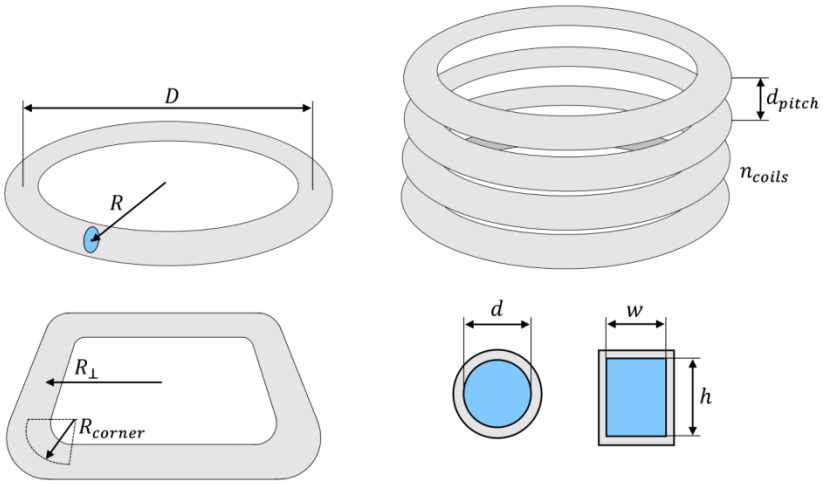

Figure 4-1 Various fluid loop configurations (circular, square, helical) and channel cross-sections (circular, rectangular) with the dimensional notation used in this analysis.

4.1 Fluid Loop Attitude Actuation

In this section, the PPs that influence attitude actuation are discussed for the fluid loop specifically: mass, angular momentum, and torque. They are calculated based on the fundamental equations from Section 2.1, and written to apply specifically to the various configurations of the fluid loop, expressed in the most fundamental design parameters (Requirement SM-5; Figure 4-1). These are then adopted in the sizing model.

4.1.1 Mass

The total mass of a fluid loop comprises the mass of the pump, electronics, channel and fluid mass. The fluid mass can be generically determined for all fluid loops by Equations 4.1 and 4.2, where it is assumed that the loop radius is much larger than the corner radius. Various fluid densities can be found in Table 4-1 in Section 4.2.1. To obtain the total fluid loop mass, the masses of the other components can be estimated with data from pumps, channels and electronics boards.

$$m_{fluid} = \rho V_{fluid} \tag{4.1}$$

$$= \rho(V_{channel} + V_{other}) = \rho(AL_{channel} + \sum V_{other\ cavities}) \tag{4.2}$$

The cross-sectional area A of a circular and rectangular channel are given by the equations below.

$$A_{circ} = \pi r^2 = \frac{\pi}{4} d^2 \tag{4.3}$$

$$A_{rect} = wh \tag{4.4}$$

The channel length $L_{channel}$ can be substituted with one of the configuration-specific channel lengths, given by the equations below.

$$L_{circle} = 2\pi R = \pi D \tag{4.5}$$

$$L_{square} = 8R_{\perp} = 4D_{\perp} \tag{4.6}$$

$$L_{square\ w/corners} = L_{straights} + L_{corners} = 4(D_{\perp} - 2R_{corner}) + 2\pi R_{corner} \tag{4.7}$$

$$L_{helix} = n_{coils}\sqrt{(\pi D)^2 + {d_{pitch}}^2} \approx n_{coils} L_{circle} \tag{4.8}$$

4.1.2 Angular Momentum

The angular momentum of a fluid loop can also be generically determined, based on the traditional angular momentum equation for a collection of point masses (Eq. 4.9). Because the channel diameter is much smaller than the loop diameter, an infinitesimally thin slice of fluid i can be considered a point mass. The sum of the angular momentums of these slices is the total angular momentum of the fluid loop.

$$|H_z| = \sum_{i=1,n}^{n} m_i v_{z,i,\perp} R_{z,i} = \int_o^m v_{z,\perp} R_z dm \tag{4.9}$$

Circular Fluid Loop

For a circular fluid loop the simplified Equation 4.10 can be used, because it represents all point masses at a radius R, moving at a velocity v perpendicular to the radius (see Figure 4-3). Their integration can be done by multiplication with the total mass m, because these variables are the same for all point masses along the length of the fluid loop.

$$H = I\omega = mv_{\perp}R \tag{4.10}$$

Next, this can be expressed in terms of the fluid loop design parameters. The mass of the inertial fluid m can be obtained by the configuration-specific Equations 4.1 to 4.8, and depends on the fluid density, the channel length and the channel cross-sectional area. The fluid velocity is dictated by the system's continuity, or the volumetric flow rate of the pump Q over the cross-sectional area A. The radius of the loop is a design parameter itself, so this can stay in place. The two cross-sectional areas cancel each other out, which results in the general notation for a fluid loop's angular momentum [Eq. 4.11], and that specifically for a circular fluid loop [Eq. 4.12].

It can be seen that the angular momentum is proportional to the density of the inertial fluid, the radius of the loop *squared*, and the flow rate of the pump. Put differently, a heavy fluid pumped through a loop as large as possible at a high flow rate produces a high angular momentum.

$$H = \rho AL\frac{Q}{A}R = \rho LRQ \tag{4.11}$$

$$H_{circle} = 2\pi\rho R^2 Q \tag{4.12}$$

This relation has some far-reaching consequences for the sizing process of the fluid loop. Traditionally, the angular momentum capacity of a reaction wheel is increased by increasing the inertial mass of the rotating wheel. The most intuitive way of doing this in the case of the fluid loop is to increase the channel diameter, so there is more fluid mass that can be rotated.

However, due to continuity this will *not* lead to a higher angular momentum of the fluid loop. At a given pump flow rate, increasing the cross-sectional area results in a mass increase, but the fluid velocity *decreases* by the same amount (see Figure 4-2). The mass flow, and thus the angular momentum stay the same in the end.

This also means that, ceteris paribus, the channel diameter of a fluid loop can be made arbitrarily small, while retaining its angular momentum. This allows for optimizing the actuator's mass. Decreasing the diameter does increase the viscous friction, so where the optimum diameter lies must be weighed off with the theory developed in this dissertation and assessed on a case per case basis.

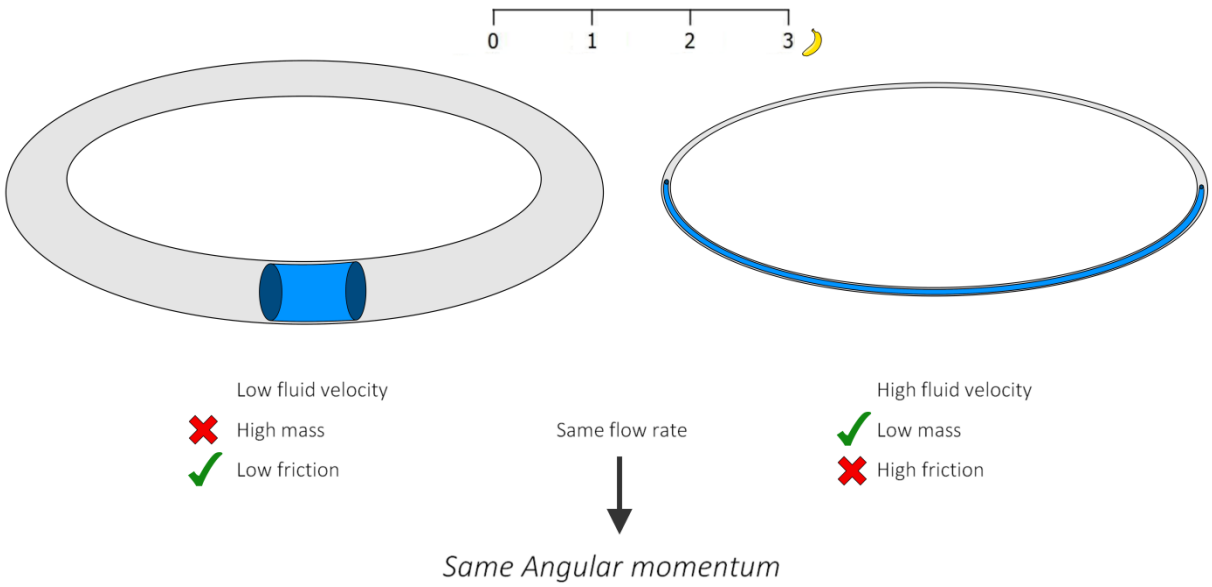

Figure 4-2 Two fluid loops with different masses and channel diameters, but equal angular momentums.

Square Fluid Loop

In theory, a square fluid loop should work according to the same principles as a circular fluid loop. However, as opposed to a circular fluid loop, the point masses along the perimeter of a square fluid loop have constantly changing perpendicular velocities and radii to the axis of rotation as they move along the channel, so at first sight the simple Equation 4.10 cannot be used here. However, a similar simple angular momentum equation is possible here, too.

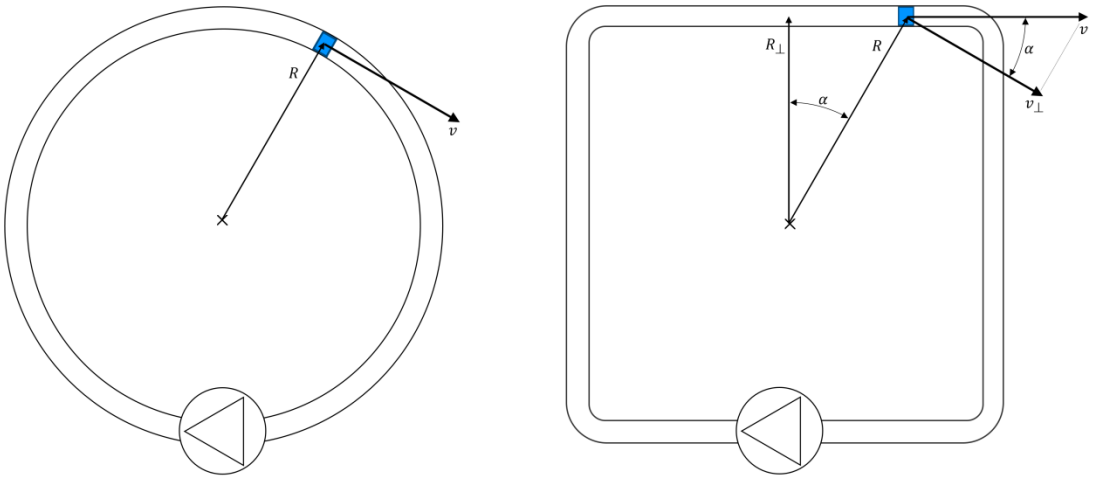

Figure 4-3 The radius and velocity of an arbitrary fluid slice point mass in a circular and square fluid loop. These variables dictate the point mass' angular momentum.

Figure 4-3 shows that the radius of the point mass is a factor $\cos\alpha$ *higher* than the perpendicular radius $R_\perp$ (which does remain the same throughout the loop). Conversely, the perpendicular velocity $v_\perp$ of that point mass is a factor $\cos\alpha$ *lower* than the fluid velocity v (which also remains the same throughout the loop). Hence, the two cosine factors cancel each other out which results in a similar equation that applies to all point masses along the square perimeter [Eq. 4.13]. Because the variables are the same for all point masses, the equation can be used for all point masses, resulting in a very similar equation to that of a circular fluid loop, where the only difference is the channel length ($2\pi R$ versus $8R_\perp$) [Eq. 4.14].

$$H_{square} = mv_\perp R = mv\cos\alpha\frac{R_\perp}{\cos\alpha} = mvR_\perp \qquad 4.13$$

$$H_{square} = \rho L R_\perp Q = 8\rho R_\perp^2 Q \qquad 4.14$$

In reality, however, the square loop will most likely have (slightly) rounded corners to reduce fluid friction. Unlike in a square, the radius and perpendicular velocity of a point mass in a rounded corner is not a simple function of α (see image 4.4). Although Equation 4.15 is a good approximation and computationally easier, it is not strictly correct.

$$H_{sq.round\ corners} = \rho L R_\perp Q = (8R_\perp - 8R_{corner} + 2\pi R_{corner})\rho R_\perp Q \qquad 4.15$$

Hence, integration of the point masses' angular momentums in the four corners is required. As usual, the angular momentum of a point mass around the fluid loop's central axis is given by:

$$H_i = m_i v_\perp R \tag{4.16}$$

Where, in this case:

$$v_\perp = v\cos\beta \tag{4.17}$$

$$R = c = \sqrt{a^2 + b^2 - 2ab\cos\gamma} \tag{4.18}$$

Where:

$$a = R_{corner} \tag{4.19}$$

$$b = \sqrt{2}(R_\perp - R_{corner}) \tag{4.20}$$

$$\beta = \frac{b\sin\gamma}{c} \tag{4.21}$$

$$\gamma = 135° + \theta \tag{4.22}$$

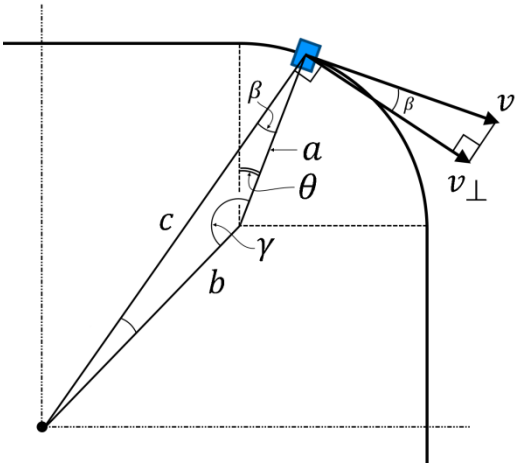

Figure 4-4 The geometry of the angular momentum of a point mass in a rounded corner of a FLIA.

The above formulation is verified with multiple numerical examples whereby the fluid mass of all corners was split into 36,000 slits of $d\theta = 0.01°$ (See Appendix 3) and integrated for angular momentum. It was found that the deviation of the approximate Equation 4.15 from the exact method above depends on the ratio of R_{corner} and $R_\perp$, and always has a maximum deviation of –5.8% at a corner ratio of $\frac{R_{corner}}{R_\perp} = 0.5$. Depending on the required accuracy, either the simple approximation or the more complex exact method can be used.

Helical Fluid Loop

As opposed to increasing the channel diameter, each extra coil *should* increase the effective flow rate, as illustrated in Figure 4-5. This makes coiling a key insight to scaling up the fluid loop. A helical fluid loop can be seen as multiple small fluid loops acting in parallel, but with the benefit of being pumped by only one pump. With each winding, the angular momentum capacity of the fluid loop is multiplied, within approximately the same constraints of the satellite envelope and pump flow rate. The extra coils do come at the expense of extra mass and viscous friction. This can be weighed off using the theory developed in this dissertation.

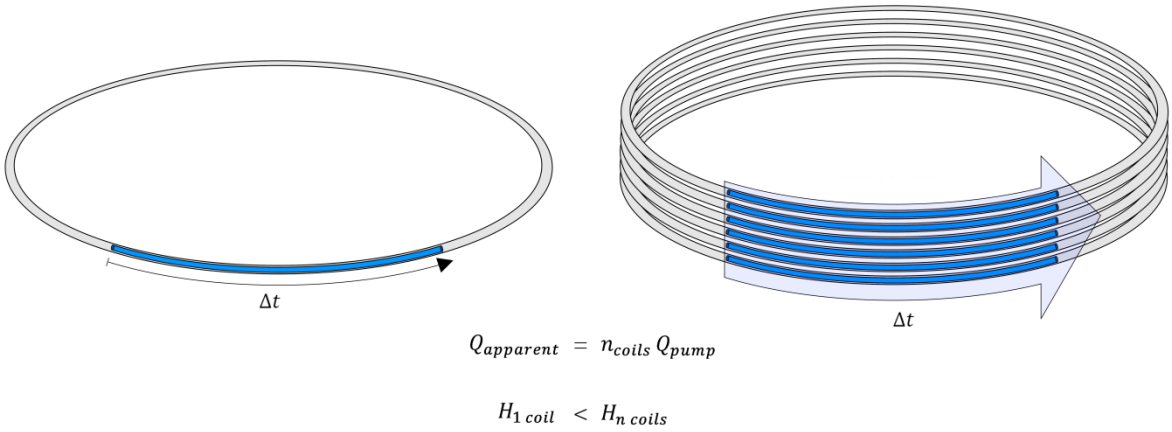

Figure 4-5 The angular momentum of the fluid loop can be scaled up by winding it in coils, thus increasing the effective flow rate. It can be seen as multiple small fluid loops working in parallel, actuated by a single pump.

$$H_{helix} = n_{coils}\sqrt{(\pi D)^2 + {d_{pitch}}^2}\,\rho RQ \approx n_{coils} H_{single\ loop} \tag{4.23}$$

$$H_{helix} = n_{coils}\rho LRQ \tag{4.24}$$

4.1.3 Torque

In general, the torque that a mass exerts on its environment depends on the rate of change of its angular momentum. Hence, the actuator's control torque depends on the same variables as the angular momentum, but instead of the flow rate Q it is multiplied by the *acceleration* of the flow rate $\dot{Q}$ [Eq. 4.25]. How strongly the flow rate is accelerated depends on many factors, such as the pump characteristics, pressure differential and fluid speed. Hence, a generic approach is difficult, if at all possible. With Equation 4.25, some $\dot{Q}$ values of MHD-pumped fluid loops are obtained from previous work and are shown in Table 4-3 in Section 4.2.3 (derivation in Appendix 4). These can be used for assuming realistic values for $\dot{Q}$ in the sizing process. This is verified as described in Section 5.3.2.

$$\tau_{control} = \dot{H} = \rho LR\dot{Q} \tag{4.25}$$

4.2 Fluid Loop Fluid Dynamics

Naturally, the performance of a fluid loop depends largely on the dynamics of the fluid inside the pipe. This section elaborates on the relevant fluid dynamics aspects specific to the conceptual design process of a fluid loop: fluid properties, pressure drop equations, and pumping and power consumption. These relations and data are used in the fluid loop sizing model. References will be made to equations in Section 2.2 to avoid repetition.

4.2.1 Fluid Properties

The fluid properties play a central part in the sizing process of a fluid loop. Firstly, the density influences many important PPs, namely angular momentum, torque, mass and volume. Second, the dynamic viscosity determines the pump pressure requirement and power consumption due to viscous friction. Third, the kinematic viscosity is a useful ratio between the two. It determines the Reynolds number, and it indicates how much angular momentum you get per unit power of friction loss. Kinematic viscosity is sometimes aptly referred to as momentum diffusivity. [48] In the case of the fluid loop, it could be called the *angular* momentum diffusivity.

Table 4-1 shows the properties of various eligible working fluids for a fluid loop. Two authors suggest refrigerator fluids, although they do not appear to be very suitable options – Ethylene Glycol [26] has a high viscosity resulting in high friction losses, and Freon-11 [16] has a boiling point of only 23.7 °C. [62] More suitable fluids are the liquid metals Galinstan and Mercury. They have a high density, a low viscosity, and can be actuated by MHD pumping. Mercury is much denser, but is toxic and less electrically conductive (which makes MHD pumping less efficient).

Table 4-1 The properties of various liquids at room temperature (25 °C).

Fluid	Density [kg/m³]	Dynamic Viscosity [Pa s]	Kinematic Viscosity [m²/s]
Water [49]	997	8.91 E-4	9.0 E-7
Ethylene Glycol [26], [49]	1100	1.62 E-2	1.5 E-5
Freon-11* [16]	1459	5.0 E-4	3.4 E-7
Sodium Polytungstate (62 %) [63]	2000	5.0 E-3	2.5 E-6
Sodium Polytungstate (76 %)	2500	9.0 E-3	3.6 E-6
Sodium Polytungstate (84 %)	3000	4.3 E-2	1.4 E-5
Galinstan (20 °C) [64]	6440	2.4 E-3	3.7 E-7
Mercury (20 °C) [65], [66]	13545	1.55 E-3	1.1 E-7

Sodium Polytungstate (SPT) is an aqueous solution that has been chosen for use in the fluid loop prototype for its high density, Newtonian properties, non-toxicity and solubility in water, so the density and viscosity can be varied. [63], [67]

4.2.2 Pressure Drop

As recognized by some authors, the viscous friction in a fluid loop has considerable influence on its performance. [16], [26] Similar to the friction in reaction wheel bearings, viscous friction dictates the power consumption and the limit on the inertial mass' speed, and thus the angular momentum and saturation limit of the actuator. In addition, viscous friction decreases the energy efficiency of the actuator. The viscous friction is expressed in pressure drop over the fluid loop, much like a voltage potential drop over an electrical component. In steady state, an equal amount of pressure is added by the pump, like the voltage addition of a power supply.

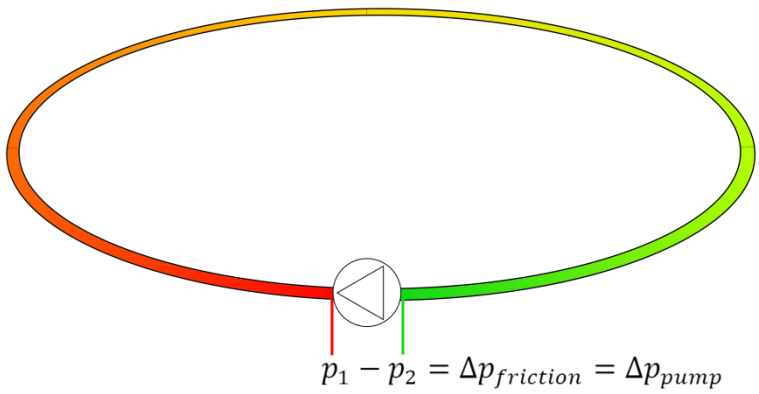

Figure 4-6 Viscous friction in the loop results in a pressure drop that is compensated by the pump.

As seen in Chapter 2, there are various factors that influence the pressure drop in a fluid loop: the fluid density, viscosity, velocity, the channel diameter and the channel length. Because a fluid loop is a loop rather than a simple straight tube, the pressure drop for bends and coils should also be considered. In addition, the flow channel might not always be smooth and homogeneous, so turbulence and flow characteristics might differ within the same actuator. This is especially the case in the non-ideal pump and filling channels of the fluid loop prototype developed for this dissertation. These imperfections make it plausible for the pressure drop to lie in a certain bandwidth that is quantified by the equations in the fluid dynamics Section 2.2 and below. The correct approaches are identified in tests with the prototype as described in the verification, validation and testing discussed in Chapter 5.

The Reynolds number N_r determines whether the flow is in the laminar ($N_r < 2000$), transitional or turbulent domain ($N_r > 4000$) (Eq. 4.26). For a fluid loop with a *circular* channel cross-section it is given by Equation 4.27. Notably, this shows that the substitution of velocity v by the flow rate over the cross-sectional area $\frac{Q}{A}$ has moved the channel diameter term d from the numerator to the denominator. Consequently, if the channel cross-section of a fluid loop is increased, ceteris paribus, the lower is the tendency of the flow to be turbulent.

$$N_r = \frac{\rho d_h v}{\mu} = \frac{d_h v}{\upsilon} = \frac{d_h Q}{\upsilon A} \tag{4.26}$$

$$N_r = \frac{4Q}{\pi \upsilon d} \tag{4.27}$$

The Reynolds number is then used to calculate the friction factor for use in Equation 4.28. For laminar flow, the linear function $f = \frac{64}{N_r}$ applies. For turbulent flow, it is given by the explicit formulations of the Colebrook equation [Eq. 2.44 and 2.45], and is influenced by the roughness of the channel wall. For this prototype, a channel roughness of 0.0015 mm for a plastic tube is assumed (see Table 4-2). Initial calculations indicate that the surface roughness at this scale only has a marginal effect on the pressure drop, so this assumption will not have a large impact on the accuracy of the solutions.

Table 4-2 Surface roughness values of various channel materials. [51], [53]

Channel material	Absolute roughness ε [mm]
Glass, Perspex	0.0015 - 0.0025
Drawn tubing (Aluminium, brass, etc.)	0.0015 – 0.0025
PVC and plastic	0.0015 – 0.006
Stainless steel (structural, commercial)	0.025 – 0.045

Finally, the pressure drop can be calculated for the different shapes of a fluid loop using the approaches discussed below. The differences in outcome will often be minor, but they should nevertheless all be evaluated to see which approach is in principle most suitable for sizing a fluid loop.

Straight Tube Approach

This method is the easiest to compute, but is technically not correct due to the inherent curve of a fluid loop. The simplified laminar variant of Equation 4.28 is used in previous work that makes mention of viscous friction. [16], [26] When used for both laminar and turbulent flow, this method could have merit here because of its simplicity. It also serves as a baseline for quick calculations and comparisons. $L_{channel}$ is substituted for any of the configuration-specific lengths (Eq. 4.5 to 4.8).

$$\Delta p = \frac{f \rho L v^2}{2d} = \frac{8 f \rho L_{channel} Q^2}{\pi^2 d^5} \tag{4.28}$$

Pipe Bend Approach

The pipe bend approach could be the most generically applicable to all fluid loop configurations. Technically it only applies to turbulent flows and calculates a loss coefficient K [Eq. 2.48] that can be inserted in Equation 2.47. For sharp elbows, $K = 1.20$ is proposed. [53] This can then be combined with Equation 4.28 for the straight pipes in between the bends, and the total pressure loss is obtained with Equation 4.29.

$$\Delta p = \sum \Delta p_{straights} + \sum \Delta p_{bends} \tag{4.29}$$

Obviously, this approach could be used for a square fluid loop with four corner bends and four straight sides. In addition, it could be argued that this method can also be used for a circular fluid loop, because it comprises four 90°-bends with no straight sides in between them.

Helix Approach

The helix approach could be more realistic for circular and coiled fluid loops, because of their constant curvature. Unlike the bend approach, the helix approach disregards the flow separation loss. After all, this does not happen again and again with a continuous curve. There are two methods that can be followed, as described in Section 2.2.3.

4.2.3 Pumping and Power consumption

As discussed in Section 2.2.4, the pressure drop in the channel as a result of viscous friction is directly proportional to the power consumption to overcome viscous friction in the channel, also known as hydraulic power. With this, the electrical power consumption of the fluid loop can also be obtained by assuming an overall pumping efficiency η [Eq. 4.30].

$$P = \frac{P_{hydro}}{\eta} = \frac{\Delta p Q}{\eta} \tag{4.30}$$

In the case of a circular fluid loop with a circular channel cross-section, the electrical power consumption of the actuator is given by Equation 4.31. It is to clarify the basic power relation, so it assumes there is no friction induced by the curvature of the loop.

$$P = \frac{\frac{8 f \rho L_{channel} Q^2}{\pi^2 d^5} Q}{\eta} = \frac{8\pi\, f \rho D Q^3}{\pi^2 \eta d^5} = \frac{128}{\eta} \frac{\upsilon \rho D Q^2}{d^4} \tag{4.31}$$

A pumping efficiency cannot be assumed very accurately, since efficiencies depend on the type of pump, its speed, the pressure differential and other variables in the system. Large mechanical pump efficiencies can exceed 90%. [68], [69] However, the smaller mechanical pumps that are more suitable for the fluid loop have worse efficiencies in the range of 40%-70% near their rated pumping speed. [70]–[72] When not operating at the nominal speed and pressure this number drops even further. Consequently, when designing the fluid loop, it must be realized that pumping is generally quite inefficient. The maximum measured efficiency of the small gear pump that was used in the fluid loop prototype is only 10%. From data sheets of the pumps considered for the fluid loop, the input power, pressure and flow rate data can serve as a base for approximating the efficiency with Equation 4.30. This shows that all small mechanical pumps also have a fairly low efficiency of 10% or less. These values can be found in Table 5-7 in section 5.5.2.

There are no data available on the efficiency of MHD pumps. Appendix 4 shows how efficiencies are reverse-calculated with the help of the theory developed above, based on published values of the FDA-6 (the TechnoSat actuator [28]), the FDA-2 (its smaller laboratory predecessor [27]), and three simulated examples [22]. Unfortunately, the results show discrepancy. The first two examples by Noack result in very low efficiencies at their nominal operating speed (3% and 0.3%, respectively), while the last ones by Curti have much higher efficiencies (81%, 55% and 48%).

Practically, the overall efficiency can be assumed as either a worst-case scenario based on Noack's results (In the range of 0.5% to 5%), or as a best-case scenario based on Curti's results (around 50%). Efficiency measurements from the used fluid loop prototype show a maximum efficiency of around 10%. This, and the fact that Noack's results are from physical tests, indicate that the lower estimates are likely the most accurate.

Since there is a difference of one to two orders of magnitude, this assumption is a large weakness in the estimation of the overall electrical power consumption of the fluid loop. However, irrespective of the pumping method, the fluid loop can still be sized to optimize the viscous friction and its power consumption component. This can be matched to a characterized pump, or used to size and pick the appropriate pump.

Table 4-3 Data of two physical and three simulated magnetohydrodynamic fluid loops, respectively, and their reverse-calculated flow rate accelerations and overall efficiencies.

Actuator	Ø [mm]	Flow rate (nominal) [L/min]	Angular Momentum [Nms]	Maximum Torque [Nm]	Flow rate acceleration [m^3/s^2]	Overall efficiency
FDA-A6 (flown) [28]	300	2.31	35 E-3	0.100	0.110 E-3	3.2 %
FDA-A2 (lab) [27]	80	0.09	100 E-6	0.40 E-3	6.18 E-6	0.29 %
MHD wheel S (sim) [22]	88	0.066	180 E-6	0.18 E-3	1.09 E-6	82 %
MHD wheel M (sim) [22]	86	0.14	360 E-6	0.36 E-3	2.29 E-6	56 %
MHD wheel L (sim) [22]	84	0.21	530 E-6	0.53 E-3	3.53 E-6	48 %

4.3 Fluid Loop Sizing Relations

The above equations are brought together in an Excel spreadsheet that allows for calculating the fluid loop PPs based on the most fundamental design parameters. Although the theory has at this point not been verified yet, some basic sizing relations can be identified.

The best indicator of the fluid loop's overall capability is angular momentum, which is closely related to the torque by Equation 4.25. On the other hand, mass and power consumption are costs and should be minimized during the sizing of a fluid loop. The ratio between the capability (angular momentum) and cost (mass or power) is a measure for the efficiency of the fluid loop, or "bang for your buck".

The angular momentum per unit mass ratio (H/m ratio, or "mass efficiency") is obtained by simply dividing Equation 4.11 by Equation 4.2. This results in Equation 4.32 (valid for

circular/helical loops and circular channels), and shows the following rule-of-thumb relations. Figure 4-7 on the next page shows these relations graphically.

- It is mass-efficient to have a large loop diameter.
- It is mass-efficient to have a high flow rate.
- It is *not* mass-efficient to have a large channel diameter (squared).

$$H/_m = \frac{n_{coils} 2\pi R^2 Q}{n_{coils} A L_{channel}} = \frac{2}{\pi} \frac{DQ}{d^2} \tag{4.32}$$

The angular momentum per unit power ratio (H/P ratio, or "power efficiency") is obtained by dividing equation 4.11 by equation 4.31. Equation 4.33 (valid for circular/helical loops and circular channels) and the graphs in Figure 4-7 show the following rule-thumb-relation for power efficiency. Note the hike in the lines where the flow transitions from laminar to turbulent.

- It is power-efficient to have a large loop diameter.
- It is *very* power-efficient to have a large channel diameter (to the power 4).
- It is *not* power-efficient to have a high kinematic viscosity.
- It is *not* power-efficient to have a high flow rate.

$$H/_P = \frac{(n_{coils} 2\pi\rho R^2 Q)}{\left(\frac{n_{coils} 128 \upsilon \rho D Q^2}{\eta d^4}\right)} = \frac{\pi \eta}{256} \frac{D d^4}{\upsilon Q} \tag{4.33}$$

When looking at Figure 4-7 on the next page, the mass and power efficiencies (i.e. the top graphs versus the bottom graphs) seem almost inversely related. Unfortunately, this complicates the sizing process of the fluid loop. Except for having a large loop diameter, there are no "more-is-better" relations. For instance, when increasing the channel diameter the power efficiency increases (a wider opening for the water), but at the same time the mass efficiency suffers under more unnecessary fluid mass. For the flow rate, a similar inverse relation exists.

Consequently, a fairly complex trade-off must be made specific to each mission, depending on the angular momentum requirement, the available pumps, and the mass, volume and power budgets. A fluid loop can only compete with a reaction wheel if the right balance is struck between mass efficiency and power efficiency. Achieving this with minimal design time is the goal of the sizing model developed in this dissertation.

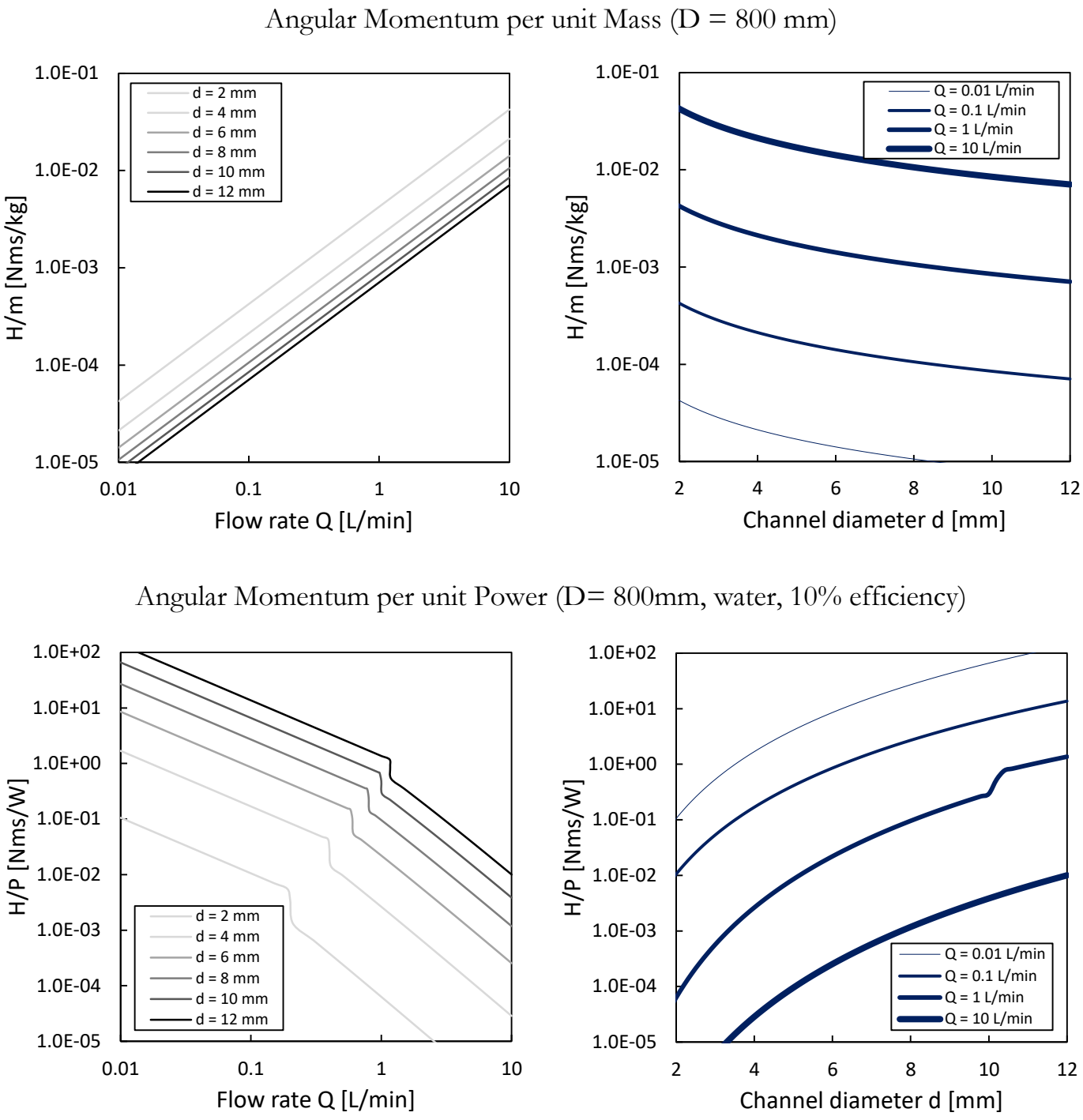

Figure 4-7 The angular momentum per unit mass ("mass efficiency"), and per unit power ("power efficiency"), as a function of flow rate and channel diameter. The graphs are specific to one configuration, but similar trends apply to all fluid loops. This configuration is for a circular fluid loop (D= 800 mm) with a circular channel cross-section, using water as working fluid and an overall efficiency of 10%. The inverse relation between the two efficiencies visualized in these graphs complicates the sizing process.

5. Verification, Validation and Test

This chapter describes the verification, validation and test (VV&T) activities of the three developed products: the fluid loop prototype, the air bearing, and the sizing model. At the same time, this discussion doubles as a description of the systems, instruments and measurement methods, and various design considerations.

The verification activities confirm whether the product meets the technical requirements ("done right"). The different types of verification activities are, in order of increasing rigor: Inspection (I), Demonstration (D), Test (T) and Analysis (A). [73] These activities happen before and during integration. The tables in the following sections show how the verification is done for each requirement. In obvious cases, the requirements listed in Chapter 3 can be ticked off after a brief inspection or demonstration. In other cases, however, additional tests or analyses are required. These non-obvious cases are discussed here in more depth.

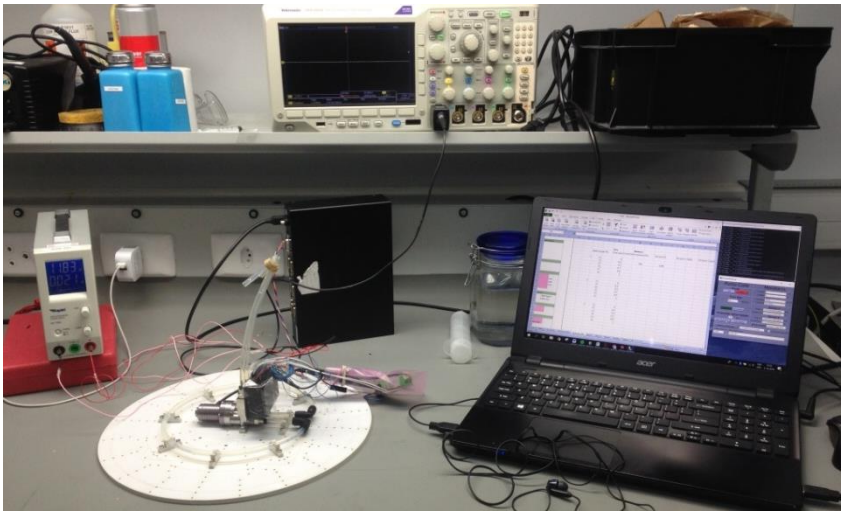

Figure 5-1 The fluid loop prototype VV&T setup on table-top. Software on the laptop sets the control voltage for the pump controller, and reads out electronic pressure measurements. The pump speed is be verified with the oscilloscope.

Validation activities confirm whether the broader operational objectives and stakeholder expectations are met ("does it right"). They also serve to prove robustness of the system, and to build confidence in the system. Here, this is done by evaluating the operating experience and discussions with the stakeholders.

Physical tests are an integral part of both phases, and fulfil various functions. Tests are done to characterize the test equipment, verify that the measurements are correct, sufficiently accurate, and that other parameters can be derived from the measurements. Finally, they are performed to verify the correctness of the theory that was developed in this dissertation, which can then be used with confidence for sizing a fluid loop. The verified model is then validated and tested by optimizing fluid loops for various satellite missions ranging from 1 kg to 3000 kg, which serves as the base for the conclusions and recommendations.

5.1 Fluid Loop Prototype VV&T

A fluid loop prototype has been designed by the author to verify the sizing theory. The verification and validation process of the fluid loop prototype results in a product that is ready to use for verifying the pressure drop and power consumption aspects of the sizing model on the table top, and for verifying the angular momentum aspects on the air bearing. It is focused on handling the reconfiguration and filling of the fluid loop, and setting up the measurement methods for flow rate, pressure drop, and power consumption. This is done entirely on the table top. Table 5-1 shows how the requirements are verified. The requirements that are marked with an asterisk are discussed in more depth in the following subsections.

Table 5-1 Requirements verification of the fluid loop prototype. The different types of verification activities are, in order of increasing rigor: Inspection (I), Demonstration (D), Test (T) and Analysis (A).

Requirement	I	D	T	A
FL-1.	✓			
FL-2.	✓			
FL-3.*		✓		
FL-4.	✓	✓		
FL-5.*			✓	✓
FL-6.*		✓		
FL-7.*		✓		
FL-8.	✓			
FL-9.		✓		
FL-10.*		✓		
FL-11.		✓		
FL-12.	✓			
FL-13.	✓			

5.1.1 Reconfiguration of the Fluid Loop (Requirement FL-3)

In order to verify the performance parameters (PPs) of the many possible shapes and sizes of a fluid loop, the prototype was designed to assume multiple configurations, while minimizing the reconfiguration time and retaining reproducibility.

Figure 5-2 shows various (but not all) configurations of the fluid loop prototype. The channel consists of a flexible polyurethane tube that can be bent in various shapes. The elbows, reducers and other fittings are all standard pneumatic parts. Laser-cut clips keep the tube in the desired shape with a tight fit that minimally deforms the tube, so that the fluid flow is not affected. The white mounting plate has threaded holes in it to screw in the tube clips in a reproducible manner. The plate is also engraved to show where the loops of various configurations run for easy reference during assembly.

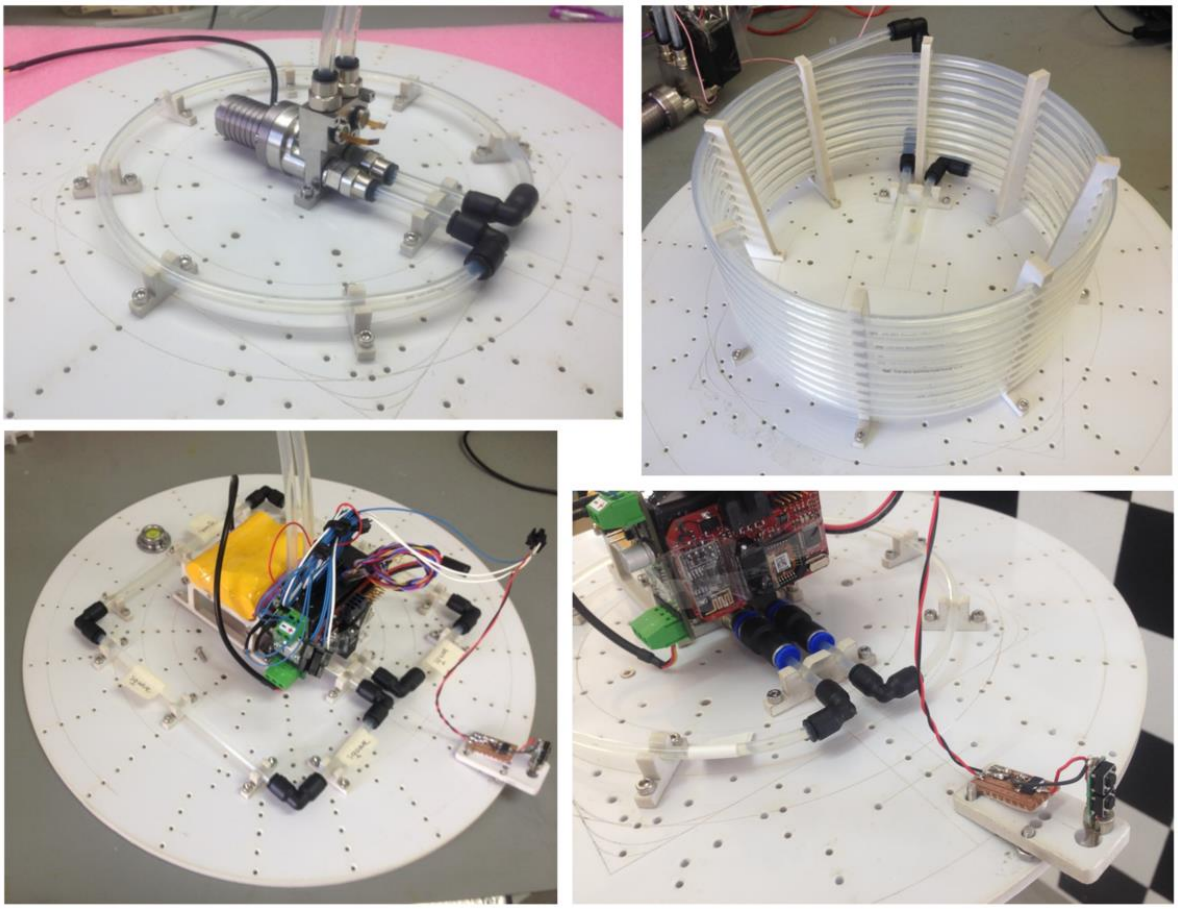

Figure 5-2 Some of the configurations of the fluid loop prototype in various stages of integration, all with a loop diameter of D = 180 mm. In clockwise order, starting top-left: the default configuration (no electronics, d = 4 mm); the helical configuration (tubing only; d = 4 mm; 10 coils); the square configuration with sharp elbows (d = 4 mm); the thin tube configuration (d = 2.5 mm).

5.1.2 Filling Mechanism (Requirement FL-10)

In order to fill the fluid loop in a reliable and reusable manner, to interface with the various components, and to minimize the occupied volume, the filling mechanism consists of a custom CNC-milled stainless steel manifold and two hollow screws.

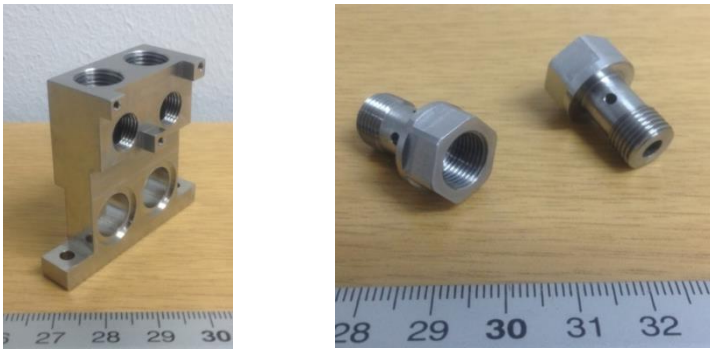

Figure 5-3 The custom-designed filling housing and screws.

Figure 5-4 shows a section view of one of the two identical cavities of the filling mechanism. On top of the filling housing (green), there are threads for the standard fittings for the filling tubes. One of the tubes allows for the insertion of liquid, while the one on the other of the loop end lets the air escape that is present in the loop. These can then be sealed off before pumping, most easily done by buckling and tying the tubes with a rubber band. Below that, two small button-like pressure sensors with threads are inserted (one on each side), that measure the static pressure at the beginning and at the end of the fluid loop. This enables the pressure drop to be measured, and thus the viscous friction losses (further explained in section 5.1.4). The two hollow screws (orange) allow fluid to flow through them, and are screwed into the inlet and outlet of the pump. This screwing action compresses the O-rings (black) and seals the assembly, while four perpendicular holes in the screws allow for the free flow of fluid between the filling housing cavity and the fluid loop. Standard tube fittings are then screwed into the custom hollow screws.

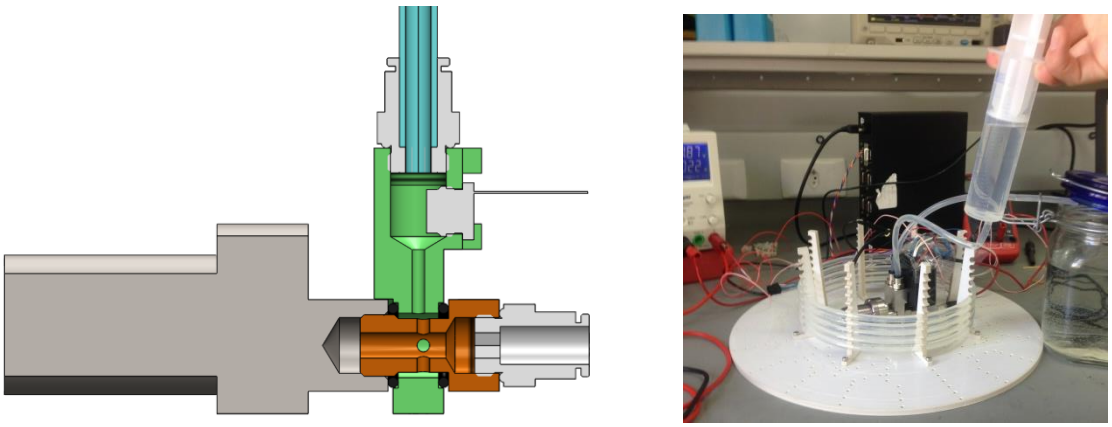

Figure 5-4 Left: A section view of one of the two filling cavities that hydraulically connects a pump port to the loop, pressure sensor and filling tubes. Right: Filling the fluid loop with a syringe.

When filling the loop, air pockets in the cavities of the pump and the filling housing end up in the stream in the form of bubbles. After some trial and error with syphoning, it was found that filling the tubes is most easily done with a large syringe that fits tightly inside the standard tubing (see Figure 5-4). This allows the air bubbles to be pushed out of the other end of the loop with force, resulting in a bubble-free, sealed off loop ready for pumping and testing.

5.1.3 Flow Rate Measurement and Characterization (Requirement FL-5)

In order to relate the theory to the measurements, the flow rate in the loop must be measurable at all times. Instead of placing a flow meter in the loop that is bulky, flow-intrusive, or non-intrusive but complicated and expensive, the pump has been chosen strategically so that it can also be used for flow rate measurements.

As opposed to the more obvious choice for a centrifugal pump because of its high flow rate and light weight, positive displacement pumps (such as the external gear pump used here) displace a fixed volume of liquid with each rotation, because they trap the liquid between the rotating gear's teeth and expel it. There are some leakage paths between the gears that transport liquid back down the flow direction, but these leakages are usually constant and the flow rate is insensitive to pressure differences. [74] Consequently, the rotational frequency (or RPM) of the pump's rotor is directly proportional to the flow rate, allowing for measurement of the flow rate by knowing the pump's RPM. This was verified by measuring the frequency of the induced current of the non-active stator coils of the pump with an oscilloscope.

The TCS MGD1000F external gear pump that is chosen for this prototype comes with a controller circuit that controls the RPM proportional to a certain control voltage between 0 and 5 V. When the pump is subjected to higher pressures, it will draw more current to increase its torque. This also means that the control voltage of the pump is directly proportional to the flow rate of the pump. This allows for flow rate measurements by the control voltage.

The characteristic relation of the flow rate and the control voltage is determined by setting the control voltage somewhere between 0 and 5 V, and measuring the respective flow rate by pumping water from a reservoir, through the pump, into a volumetric flask of 300 ml that is standing in an empty basin to catch spills. A stopwatch is started the moment the fluid reaches the 100 ml line, and stopped when it reaches the 300 ml line. For each set control voltage, this procedure is repeated 3 to 4 times and the average flow rate is taken. Equation 5.1 and Figure 5-5 shows the linear characteristic, which is integrated into the simple graphical user interface (developed by NSS) that sets the control voltage for a desired flow rate.

$$U_{control} = 0.004304 * Q_{set} - 0.06254 \quad 5.1$$

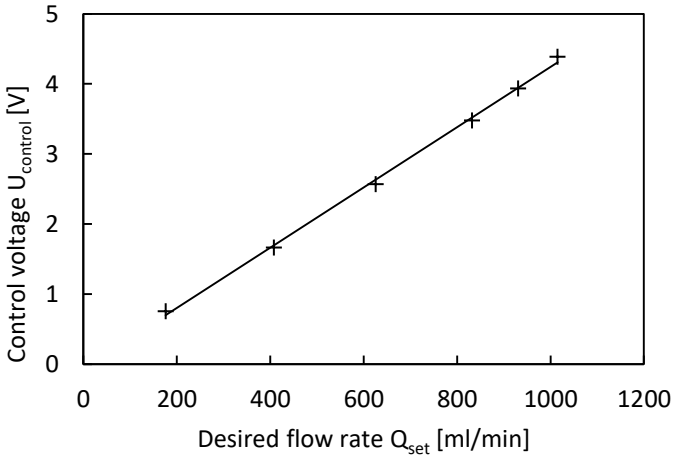

Figure 5-5 Test results that show the relation between the control voltage and the flow rate. This is used by the interface software to control the pump speed.

5.1.4 Pressure Drop Measurement (Requirement FL-6)

Next, the pressure drop over the fluid loop should be measured. The two 89BSD pressure sensors (range: 0-6 bar; accuracy: ±0.018 bar) mentioned in section 5.1.2 measure the static pressures in the fluid near the inlet and outlet of the pump. Subtracting the pressure measured at the end of the loop from the pressure at the beginning gives the pressure drop over the entire loop, shown as green plus red in Figure 5-6.

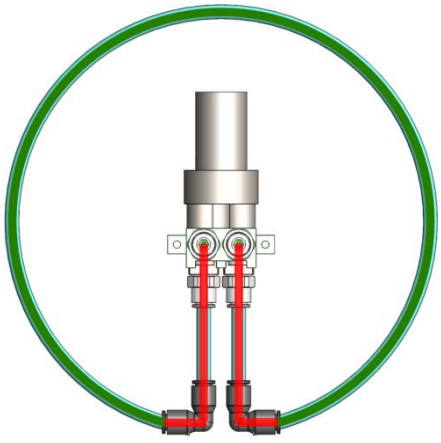

Figure 5-6 A top view of the fluid loop. The pressure drop theory is only concerned with the green part of the loop, so the red part must be isolated and deducted from the test results.

However, the developed theory is only concerned with the friction in the outer ring of the loop (green), rather than the whole loop including the entrance region (red). In order to isolate the pressure drop over the outer loop, the pressure drop in the entrance region is characterized by connecting the two elbow fittings to one another, so that only the red loop exists. This entrance pressure drop is then later subtracted from the pressure drop measurements over the entire loop (green plus red) to arrive at the pressure drop over just the outer loop. This is characterized for the default 4 mm channel diameter configuration, and for the thin (2.5 mm) and wide (5 mm) channel configurations that differ in pressure drop due to their different channel diameter and the in-line reducer fittings in the latter two cases.

Because the pressure fluctuates somewhat during steady operation, all pressure measurements are done by computer to eliminate human error. The software allows for the automatic logging of pressure values at a frequency of 50 Hz. For each measured flow rate, pressure drop is logged for a couple of seconds during steady operation, from which the average is taken. This results in smooth well-fitting relations for the pressure drop over the entrance as a function of flow rate.

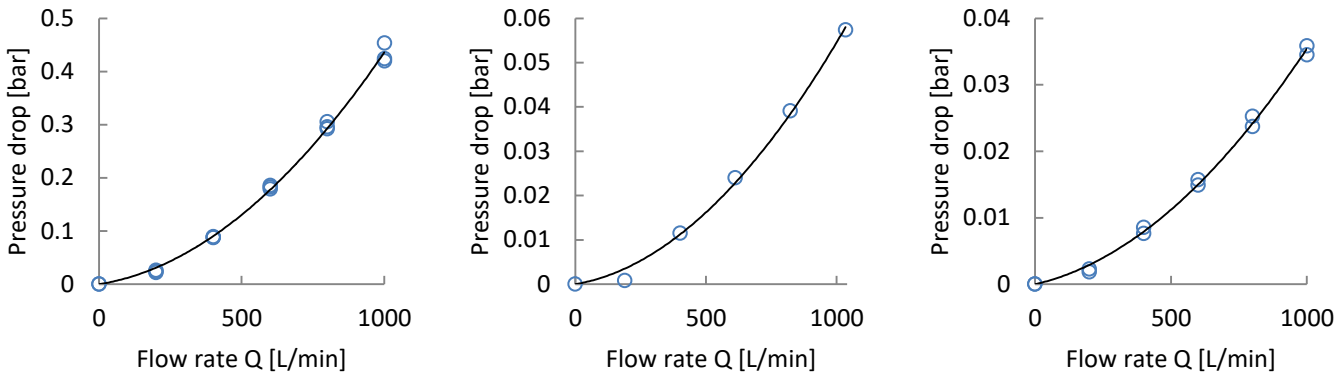

Figure 5-7 The pressure drop over the entrance regions of the three different channel diameters: 2.5, 4 and 5 mm, respectively. The 2.5mm and 5mm entrances include the reducer fittings to adapt the diameter.

$$\begin{aligned} \Delta p_{2.5mm\ entrance} &= 3.500 \cdot 10^{-7} Q^2 + 8.591 \cdot 10^{-5} Q \\ \Delta p_{4mm\ entrance} &= 4.435 \cdot 10^{-8} Q^2 + 1.026 \cdot 10^{-5} Q \\ \Delta p_{5mm\ entrance} &= 2.605 \cdot 10^{-8} Q^2 + 9.366 \cdot 10^{-6} Q \end{aligned} \qquad 5.2$$

Another correction is made for the small offset of the two pressure sensors. Even when not pumping or not exposed to a fluid, the pressure sensors measure a slightly different pressure, within the rated accuracy (0.004 - 0.008 bar). This offset is also influenced by how full the filling

tubes are and how tightly they are sealed. Therefore, for each set of measurements this offset is subtracted from the final pressure drop, as if they start at the same base pressure.

The method described in this section has one known technical error, but this is not significant in the final results. The flow separation that occurs in the elbows (as described in section 2.2.3) occurs twice in the real loop (entering and exiting the loop), whereas in the 180° bend of the two directly connected elbows it occurs only once. [53] This could be corrected by subtracting the separation component from Equation 2.48 from the each individual pressure drop measurement. Fortunately, calculations and further well-fitting test results (described in section 5.3) indicate that the separation component is so small here that it is negligible.

5.1.5 Power Consumption Measurement (Requirement FL-7)

The power consumption of the pump and the supporting electronics is measured by placing a calibrated multimeter in the current-setting in series with one of the power supply lines. The current is recorded and multiplied with the supply voltage to obtain the power consumption.

It was intended to follow a similar approach as described in Section 5.1.4 to get the power consumption of *only* the outer loop, by subtracting the entrance power consumption from the total power consumption. However, this turned out not to be possible. Because the total loop produces a higher pressure drop than only the entrance region, the power consumption values and pump efficiencies were not consistent or comparable between the two configurations, and hence not fit for subtraction.

The power consumption can only be measured on the bench, because it requires voltage and current readout, which has not been implemented in the software. The current fluctuates slightly, which makes the readout susceptible to human error. However, it is not too difficult to estimate a mean value. Multiple tests are done to find an average value.

Another test was done to see if a different supply voltage changes the performance of the pump, to see if a changing battery voltage would influence the results. This turned out not to be the case – a lower supply voltage is met by a higher current being drawn to the pump to maintain the RPM the control voltage dictates. This confirms that tests on the air bearing will be consistent regardless of the exact battery voltage level.

5.2 Air Bearing VV&T

A spherical air bearing was designed by the author to verify the angular momentum aspects of the sizing model. The verification and validation process of the air bearing results in a product that is ready to use for testing, in combination with the verified fluid loop prototype. The VV&T activities are focused on accounting for disturbances, balancing the rotating assembly and setting up a method for measuring the angular momentum. Table 5-2 shows how the requirements are verified. The requirements that are marked with an asterisk are discussed in more depth in the following subsections.

Table 5-2 Requirements verification of the air bearing. The different types of verification activities are, in order of increasing rigor: Inspection (I), Demonstration (D), Test (T) and Analysis (A). Requirement AB-8.b (acceleration measurement) was not met due to a missing inertial measurement unit.

Requirement	I	D	T	A
AB-1.	✓			
AB-2.	✓			
AB-3.	✓			
AB-4.*				✓
AB-5.*				✓
AB-6.	✓			
AB-7.	✓			
AB-8.*	–		✓	✓
AB-9.				✓
AB-10.	✓			
AB-11.	✓			
AB-12.	✓			
AB-13.		✓		
AB-14.	✓			
AB-15.	✓			
AB-16.	✓			

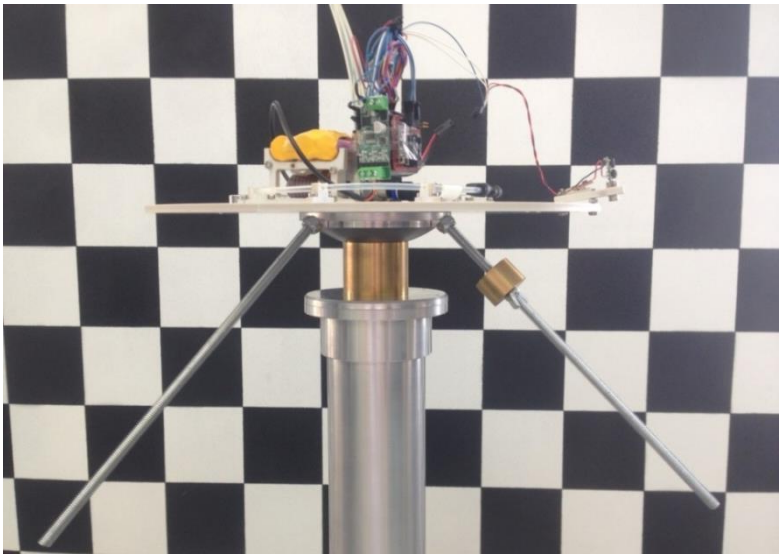

Figure 5-8 Side view of the air bearing that was designed for attitude tests with the fluid loop. The background grid squares are 10×10 cm².

5.2.1 Balancing the Rotating Assembly (Requirement AB-4 and AB-5)

A spherical air bearing allows rotational motion in all three degrees of freedom at close to zero friction, thus simulating the orbital environment. It does this by pumping compressed air between a spherical static concave surface and a rotating spherical convex surface. The sub-millimetre air film suspends the rotating assembly that can swing freely around its centre of rotation (CR), as if it were a pendulum. The CR coincides on the shared centre point of the two spherical surfaces ($R_{bearing} = 81\ mm$).

Figure 5-9 shows a section view of the static air bearing (beige) and the rotating assembly (silver). The centre of gravity (CG) is shown as a black-white cross, "hanging" from the CR. Like a pendulum, the air bearing aligns the CG with the CR and the direction of gravity. The primary axis of rotation (green) is therefore always vertical.

However, the fluid loop prototype was designed to rotate around the axis of symmetry of the air bearing (blue), in order to reduce wobbling from an asymmetric mass distribution. To align the axis of symmetry with the axis of rotation, three threaded rods are attached to the rotating assembly to which masses can be attached with a wing nut. This makes it possible to shift the CG onto the axis of symmetry, which aligns the two axes. This is reproducible by registering the configuration, mass and distance of the weight to the central ring. A bulls-eye spirit level (accuracy: ±2mm/m) is mounted on the prototype plate to confirm a properly aligned axis. Balancing is found to be fairly easy, but not completely accurate due to human error, and uncertainty in flatness of the plate and mounting surface. However, the minimal wobble of less than 1° during even the most abruptly rotating tests proves that it is sufficient.

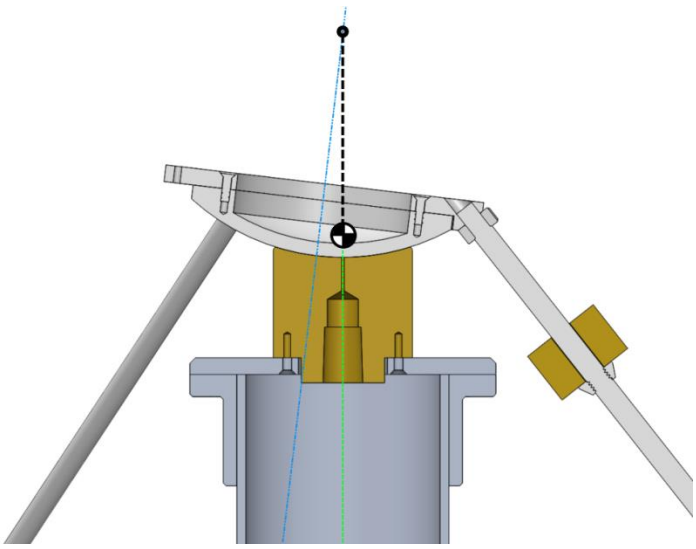

Figure 5-9 Section view of the air bearing with the centre of gravity (black/white) aligned with the axis of rotation (green), with which the blue axis of symmetry should coincide. This can be approached by shifting the balancing weight.

5.2.2 Angular Motion Measurement (Requirement AB-8)

The most important objective of the air bearing in this project is verifying whether the various configurations and unusual shapes of the fluid loop achieve their expected angular momentum and torque, so that the fluid loop can be easily designed, scaled and shaped to suit the satellite and mission requirements with confidence.

To measure angular motion, it was initially intended to use an electronic inertial measurement unit (IMU). Unfortunately, this could not be realized due to schedule overruns.

To nonetheless take angular motion measurements, a laser pointer and a graduated in degrees on the floor are used to indicate the position. A cheap laser pointer is taken apart and powered by the same battery that is used to power the pump. By recording the angular position of the laser point on video and pausing it exactly on the second (with a special function in the VLC mediaplayer), the average angular velocity and angular acceleration can be deduced between two points in time. The angular position can be accurately read from the video to 0.5°. The minimal one second timestep does constrain the accuracy and resolution of the angular acceleration measurement, which is more short-lived than the steady state angular velocity.

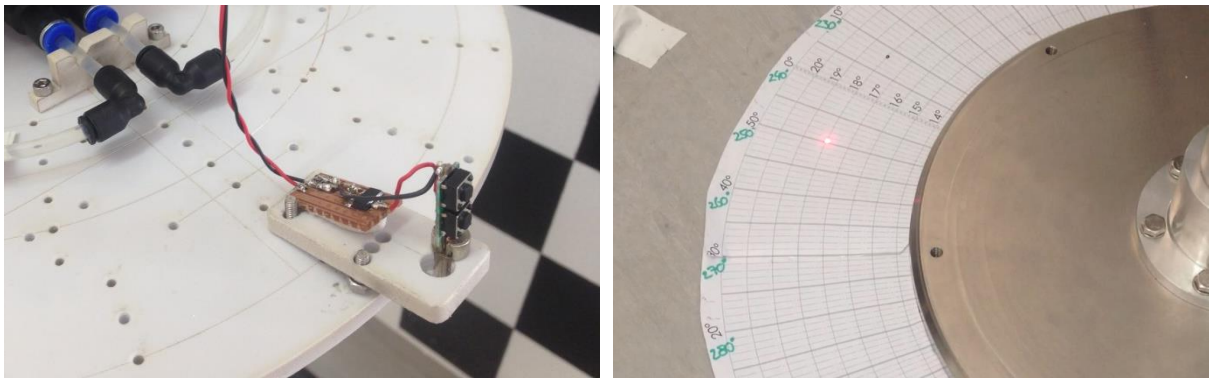

Figure 5-10 The laser diode mounted on the rotating assembly pointing the angular position on a degree arc on the floor. The angular velocity is then derived from a video recording.

Air Bearing Disturbances

Taking reliable and accurate measurements proved to be more difficult than expected, due to the many different disturbances that work on the sensitive air bearing. The air bearing was first put in the clean room at NSS, where it started spinning up by itself. After some head scratching, it was found that the draught from a nearby computer fan spun up the assembly. Because the whole

cleanroom was rather draughty, the air bearing was moved to another room with no draught. However, many more disturbance torques were found that could not be circumvented.

The torques are surprisingly similar in nature to the environmental disturbance torques discussed in section 2.1.3, and they too are either secular or cyclic. Just like in orbit, the secular torques result in an increase or decrease of angular momentum over one rotation. The cyclic torques, however, do not result in a net zero angular momentum build-up after one rotation – the amount of time the cyclic torques work on the assembly constantly varies, because the disturbances are constantly changing the angular velocity of the rotating assembly. This results in a varying angular momentum build-up of the cyclic torques.

Firstly, there is a cyclic magnetic disturbance torque that works to align the magnetic field lines of the pump's magnetic rotor with the field lines of the geomagnetic field, much like a compass needle. This is verified by changing the orientation of the pump relative to the convex of the air bearing, and seeing the pump point in the same direction – due North.

Second, there is a secular air drag torque that slows down the rotating assembly. This is verified by measurements taken over multiple rotations, seeing a higher deceleration at a higher angular velocity (Figure 5-11).

Third, there is a secular component that spins up or slows down the air bearing due to its own air flow. The compressed air from the small hole in the concave diffuses past the convex, the attached rods, and the plate of the fluid loop prototype. Any miniscule geometric asymmetries in any of those parts lead to the rotating assembly working as a mill in the wind. This effect is not understood completely, but is verified by the air bearing spinning itself up (without the fluid loop assembly attached, in a windless room). This effect also turned out to vary with the air pressure set at the compressor, which resulted in the fixing of the pressure regulator at 2 bar for all tests.

Fourth, there is a not completely understood disturbance torque due to the misalignment of the axis of rotation (on which the CG lies), the axis of symmetry of the concave, and the axis of symmetry of the convex. This was verified by tilting the static base of the air bearing, and changing the position of the CG of the rotating assembly, all resulting in slightly different behaviours.

Measurements were made in an attempt to characterize the disturbances, so that the test data could be corrected (see Figures 5-11 and 5-12). The air bearing was spun up, and every 10 seconds a velocity measurement was taken. The graph shows that the secular torque gradually

brings the average velocity down, while the cyclic torque causes fluctuations around the average. Because the air bearing slows down, the rotational period becomes longer, which means that the torques have a longer time to work, resulting in a larger angular momentum change. In the graph, this can be seen by the growing of the amplitude of the cyclic angular velocity changes.

This method turned out not to be reliable. It required the velocity of the actual test being set equal to the velocity of the characterizing test, and subtracting the secular angular momentum decrease over one rotation. However, at the moment of equal velocities between the two tests, the angular position was always different, resulting in a different torque distribution over time.

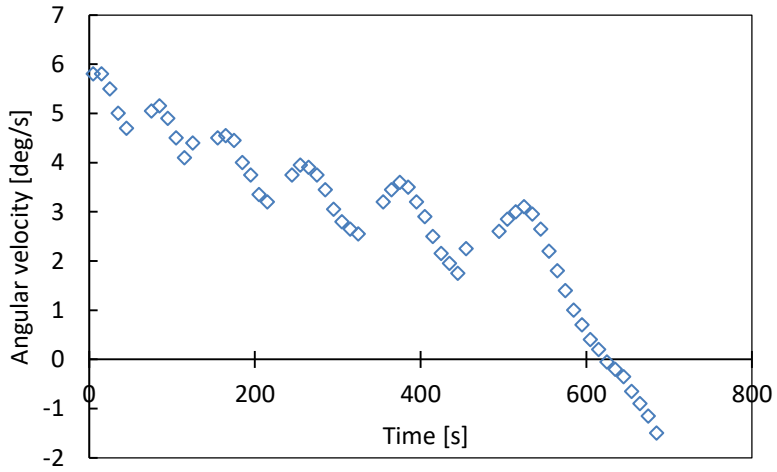

Figure 5-11 The variation of the air bearing's rotation over time. A cyclic and secular disturbance can be distinguished; the latter eventually brings the velocity down enough that the assembly stops making full rotations and starts oscillating around the point of stable equilibrium.

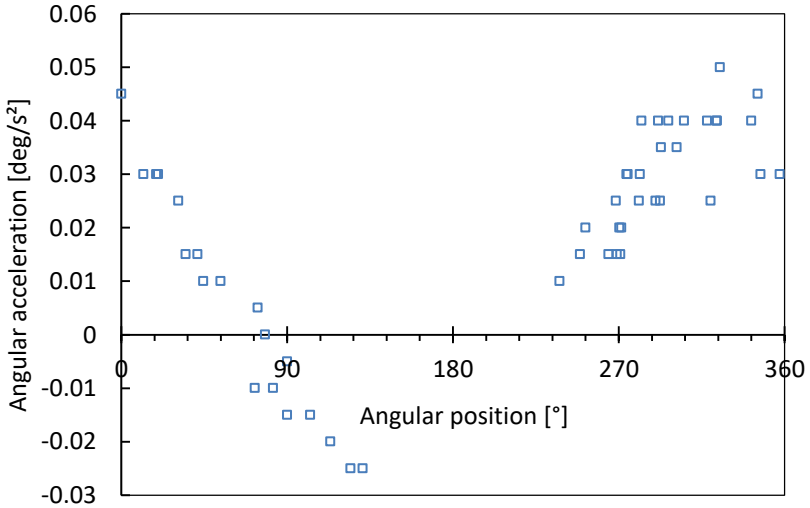

Figure 5-12 The variation of the disturbance accelerations on the rotating assembly as a function of its angular position, measured over multiple rotations. The points of equilibrium are around the intersections with the horizontal axis.

Measurement Method

The strategy used for measuring angular momentum minimizes the above disturbances in such a way that they can be neglected. It turns out to be surprisingly accurate and reproducible. It makes use of the fact that the rotating assembly has two "dead points", where the acceleration (and thus the disturbance torque) is zero. As can be seen in Figure 5-12, these points lie around the 60° and 240° marks on the arc on the floor. The gap in the data is because the points behind the air bearing pedestal could not be captured.

Indeed, after some fiddling, the points were found to be 58±5° for the "low" point of stable equilibrium (comparable to a ball in a bowl), and 232±1° for the "high" point of unstable equilibrium (comparable to a ball on a smooth hilltop). The low point can be determined with less accuracy, due to a wandering effect with an unknown cause.

Figure 5-12, the disturbance accelerations/torques near these two points are very close to zero. So, by taking an angular velocity measurement near a dead point, the disturbance is minimized. When the measurement is taken over a very short amount of time, right after the fluid spins up, the time the disturbance torque can act to affect the angular velocity is also minimized.

To test the sizing theory, the measured angular velocity ω is compared to the theoretical value, obtained by Equation 5.4 (all in SI units!). All values here are known or set, except for the inertia of the rotating assembly. So, the inertia I of each configuration is determined analytically with the 3D CAD software SolidWorks. For this, each component in the CAD model is given a custom material density, obtained by dividing the weighed mass of the real component by the volume in the CAD model. This is done for all parts, including the electronics, tubes with liquid, screws, nuts and clips. This proved to be rather time-consuming, but accurate. The only uncertainty here is the location of the CG of the parts, since the approximation is made that the mass distribution in all parts are homogenous. This uncertainty is largest in the electronics assembly, pump and battery, but will be neglected.

$$H = I\omega = \rho LRQ \tag{5.3}$$

$$\omega = \frac{\rho LRQ}{I} \tag{5.4}$$

Initial tests showed that this method corresponds very well with the theoretical predictions of the default circular fluid loop configuration, a configuration that already proved to behave as theory predicts by Noack [28]. They also showed that results are reproducible, and more so around the

more clearly-defined "high point". Hence, this method is used for all angular momentum measurements. It is repeated 3 or 4 times, both clockwise and counter-clockwise, the average is taken and compared to the theoretical value.

The air bearing also has some limitations.

- The air bearing only yields accurate angular momentum measurements when the velocity is measured over a short period of time, close to one of the dead points. For longer attitude tests, the disturbance torques should be characterized much better, and a method for accounting for the disturbances should be set up. There was no time to do this during this project.
- The pressure drop tests cannot be taken effectively on the air bearing, because the wireless connection does not allow for more than one message per second. Therefore, the fluctuating pressure cannot be gauged enough to get a good average.

5.3 Sizing Model Verification

One of the main objectives of this dissertation is to develop a theoretical model for the sizing of fluid loops that can be used with confidence. This includes verifying the relationships of how shape (circular, square, helical), dimensions (channel and loop diameter), and fluid properties affect the angular momentum and power consumption due to viscous friction. Rotational dynamics and fluid mechanics provide the theory base for these relations, but these specific cases have never been empirically verified since there are very few other uses for endlessly pumping a fluid around in a loop.

Table 5-3 shows how the requirements are verified. The fluid loop design part of the sizing model (requirement SM-1 to SM-5) is verified by comparing configuration-specific angular momentum and pressure drop predictions to the values measured with the test setup according to the methods described in the previous sections. With these results, the torque and power consumption aspects of the sizing model can indirectly be verified.

The auxiliary disturbance environment part of the sizing model (requirement SM-7 to SM-11) is verified by feeding values of real missions into the model, and comparing the resulting actuator requirements from the model to the PPs of the actual reaction wheels on board the satellite. An order-of-magnitude approximation is deemed sufficient here for verification, because these early estimates are usually not very accurate as there are many assumptions involved in the disturbance environment calculations.

Table 5-3 Requirements verification of the fluid loop sizing model. The different types of verification activities are, in order of increasing rigor: Inspection (I), Demonstration (D), Test (T) and Analysis (A).

Requirement	I	D	T	A
SM-1.	✓			
SM-2.	✓			
SM-3.	✓			
SM-4.		✓	✓	
SM-5.	✓			
SM-6.	✓			
SM-7.		✓		
SM-8.	✓			
SM-9.	✓			
SM-10.	✓			
SM-11.	✓			

5.3.1 Angular Momentum

The tests to verify the angular momentum have been done according to the method described in Section 5.2.2. Table 5-4 shows the most important parameters of the various configurations, the theorized angular velocity as described in Section 4.1.2, and the measured angular velocity. All configurations have a diameter of 180 mm.

As can be seen in Table 5-4, the deviation of the measured value from the expected is minimal. The small deviations can be attributed to uncertainty in CG positions and inertia, geometric imperfections and the very small disturbance torques. Therefore, it can be concluded that the angular momentum sizing equations from Chapter 4 can be applied with confidence.

Because square and helical fluid loops work as expected, these results are beneficial for the case of the fluid loop. A square shape is extremely useful for design and implementation, because most satellite buses are rectangular. It also implies that any other loop shape, such as rectangular or hexagonal, can be calculated based on the same method as described in Section 4.1.2. This increases the versatility and applicability of the fluid loop. In addition, the fact that a helix works as expected means that scaling can also be done by coiling the loop (in any shape!), instead of only by changing the fluid, loop diameter or pump capabilities. This also eases the design significantly.

Table 5-4 the measured angular velocities of various configurations of the fluid loop (average of four tests) versus the expected theoretical values. The minimal deviation verifies the theory.

Configuration	Inertia [kgm²]	Flow rate [ml/min]	Expected angular velocity [deg/s]	Measured angular velocity [deg/s]	Deviation
Default	0.01287	1000	3.70	3.81	+ 3.1%
Square w/elbows	0.01324	1000	4.60	4.63	+ 0.6%
10 coils	0.01440	1000	33.60	34.61	+ 2.9%
Thin tube 2.5 mm	0.01392	1000	3.36	3.17	– 6.1%
Default with SPT (3000 kg/m³)	0.01299	500	5.51	5.53	+ 0.4%

5.3.2 Torque

Because torque is the time derivative of angular momentum, any changes in angular momentum (i.e. flow rate) per definition result in a torque. Therefore, the verification of the angular momentum equations for a fluid loop indirectly means that the torque equations for a fluid loop are also correct. The question remains whether specific pumps can manage a high enough flow rate acceleration $\dot{Q}$. This should be determined for each individual pump.

Table 4-3 in Section 4.2.3 can be used to assume a value for pump flow rate acceleration for initial torque sizing purposes of the fluid loop. Unfortunately, this list is not exhaustive, because pumps are only rated on steady state flow rate rather than flow rate *acceleration*. Hence, there are only MHD pumps in this list used for fluid loops. This limits the estimation of the torque of a fluid loop.

It appears that MHD pumps have a very high torque capability [28], whereas centrifugal pumps have a mediocre torque capability. [26] It is expected that gear pumps (and positive displacement pumps in general) have a reasonably good torque capability, because they generate more pressure and the coupling with the fluid is more direct than centrifugal pumps. Despite the lack of acceleration measurements, this is confirmed by comparing the performed tests. For instance, the default configuration and the configuration with 10 coils both take approximately the same time (~1 second) to speed up to their maximum angular velocity, making the torque in the latter case 10 times higher, as expected per Equation 4.25.

5.3.3 Pressure Drop

To verify which pressure drop equations should be used in which case, tests are done using the method described in Section 5.1.4. The findings are presented by comparing four different theoretical pressure drop predictions to the measured values. The measurements will point out which of the calculation approaches as described in Section 2.2 and 4.2 work best for which configuration. The four calculation methods are:

- **Straight tube approach**: most simple approach; as if the loop were one straight pipe.
- **Bend approach**: for square loop configurations; gives a K-factor for the pipe bends and uses Darcy's equation for the straight pieces.
- **Helix approach 1**: gives a K-factor for the entire helix.
- **Helix approach 2**: based on the Dean number; gives a friction factor for the entire helix that is used in Darcy's equation.

All approaches use the equations for turbulent flow in the transition area. All configurations of the prototype have a diameter of 180 mm. The test results are discussed per configuration, and a short conclusion on when to apply which calculation method is given at the end of this section.

Default Configuration

Figure 5-13 shows that the measured values of the default configuration correspond very well to all four approaches. Especially the second helix approach seems to follow the somewhat flatter imaginary curve of the measurements the best, also in the middle transition area. One of the measurements jumps out from the rest, and can be attributed to a measuring mistake or the unpredictable behaviour in the transition state between laminar and turbulent. Because there are no similar anomalies in any of the tests, it will be disregarded. The theoretical point where the state of flow goes from laminar to transition/turbulent can also be seen in the sudden hike of the three bottom curves, changing the pressure increase with flow rate from linear to exponential. This is verified by the higher-than-laminar results at $Q = 400\ ml/min$, after the hike.

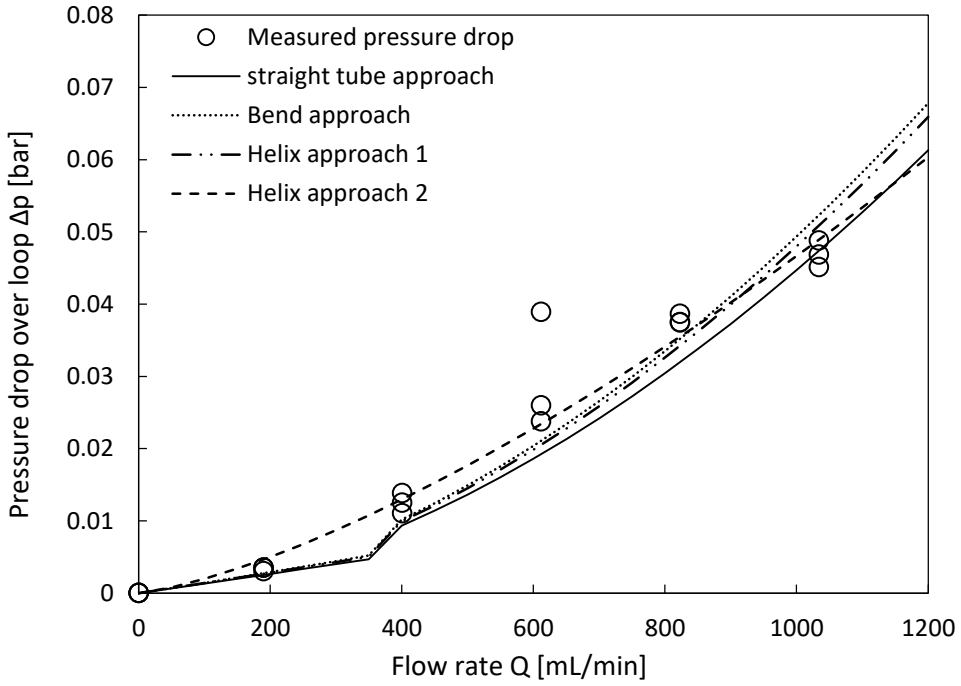

Figure 5-13 The measured pressure drop over the fluid loop as a function of flow rate versus the four theoretical predictions. Default configuration, circular loop, D= 180 mm, d= 4 mm. Corrected for entrance region friction. The sole discrepant measurement is disregarded; see text for further interpretation.

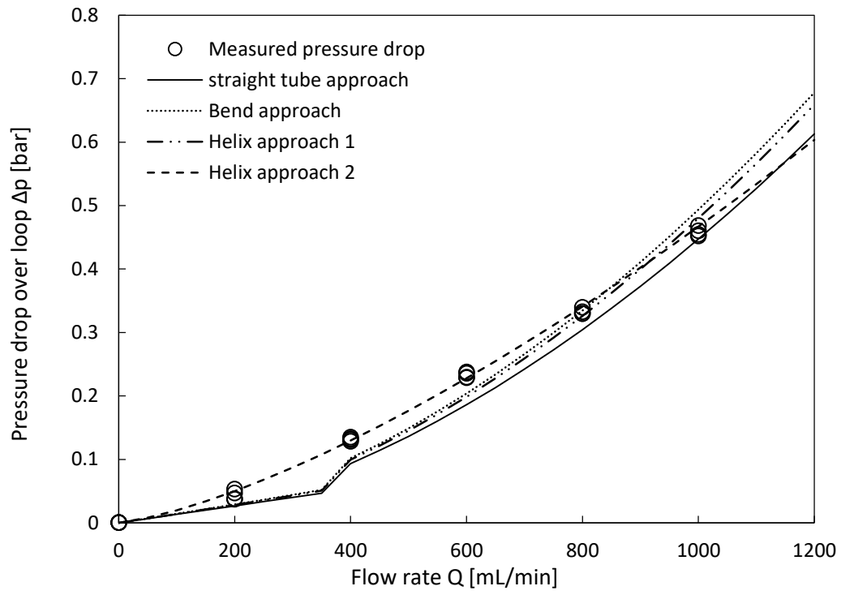

Figure 5-14 The measured pressure drop over the fluid loop as a function of flow rate versus the four theoretical predictions. Thin tube configuration, circular loop, D= 180 mm, d= 2.5 mm. Corrected for entrance region friction.

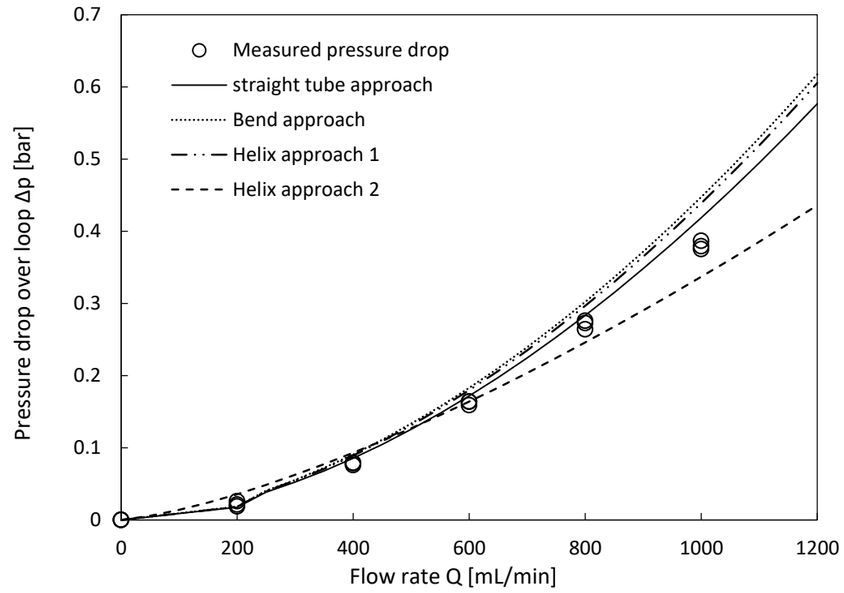

Figure 5-15 The measured pressure drop over the fluid loop as a function of flow rate versus the four theoretical predictions. 10 coil helix configuration, circular loop, D= 180 mm, d= 4 mm. Corrected for entrance region friction.

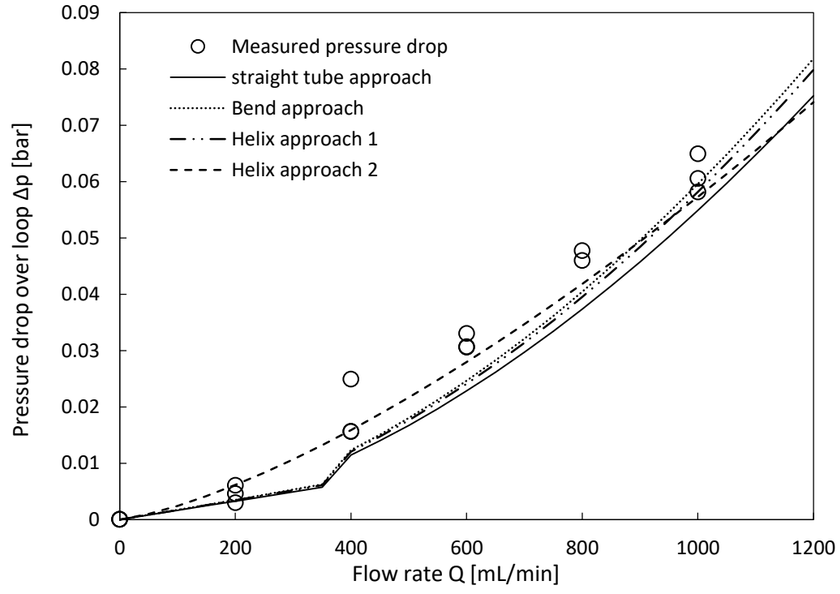

Figure 5-16 The measured pressure drop over the fluid loop as a function of flow rate versus the four theoretical predictions. Square loop with rounded corners, D= 180 mm, d= 4 mm, R_{corner}= 15 mm. Corrected for entrance region friction.

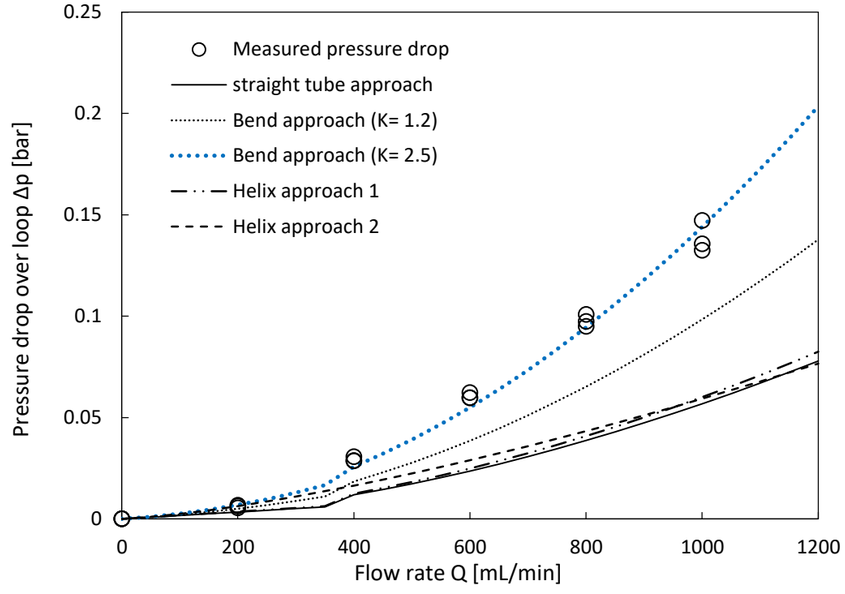

Figure 5-17 The measured pressure drop over the fluid loop as a function of flow rate versus the four theoretical predictions fitted curve that shows the K-factor of the non-ideal elbows. Square loop with sharp elbows, D= 180 mm, d= 4 mm, R_{corner}= 15 mm. Corrected for entrance region friction.

Thin Tube Configuration (2.5 mm)

The measurements of the thin tube configuration correspond well with all theoretical values, especially the second helix approach (Figure 5-14). Although decreasing the channel diameter does not affect the angular momentum capacity, this confirms that decreasing the channel diameter too much (for mass optimization, for instance) has a huge effect on the pressure drop and power consumption of the actuator. When comparing the 2.5 mm channel to the default 4 mm channel, the pressure drop is a factor 10 higher.

Helix Configuration (10 coils)

The measurements of the coiled configuration follow all theoretical predictions well at lower flow rates (Figure 5-15). However, at higher flow rates the second helix approach diverges from the others, while the measurements lie somewhere in between the two. It is likely that the Helix Approach 2 is the more accurate approach, because the subtracted friction losses of the entrance region as described in 5.1.4 only account for two elbows – the friction in the extra elbow and tube unique to the helix configuration can account for the difference with the Helix Approach 2, because they were not measured and subtracted from the total measurement.

Square Configuration with 15mm Rounded Corners

The measurements from the square configuration with 15 mm-radius round corners follow all four approaches too, although they are generally a little higher (Figure 5-16). This can be explained by the fact that the flexible tube in the corners might have buckled slightly, because it is close to its minimum bending radius. This irregularity in the flow path results in losses similar to the expansions and contractions described in 2.2.3. Notably, there is no real difference between the straight tube approach and the bend approach, even though there are four bends in the loop. It seems that with a smoothly curved, continuous pipe, bends have minimal influence on the pressure drop. This is good news for applicability of the fluid loop in its square configuration – having smooth corners has a minimal effect on the power consumption. The two theoretical curves start diverging minimally at higher flow rates, but the measurements seem to tend closer to the flatter straight tube approach and the second helix approach.

Square Configuration with Sharp Elbows

The square configuration with sharp elbows has a considerably higher pressure drop than expected (Figure 5-17). This can be attributed to the fact that all used elbows are separate parts,

breaking the smoothness of the channel surface. There are 8 extra imperfect connections between the tubes and the elbows. In addition, the inside of the used elbows could also be narrower than the 4 mm channel or otherwise non-ideal. Especially in turbulent flow, this can cause eddies that can have a considerable downstream effect. The blue curve that is fitted to the measurements has a K-factor of 2.5 instead of the recommended 1.2 for elbows.

Even if the fluid loop was made with perfectly smooth elbows, the large difference (a rough factor 2) in pressure drop compared to the rounded corner configuration indicates that sharp elbows might not be the best option. Even at a K-factor of 1.2, the pressure drop curve of elbows diverges a lot from the others. Because the pressure drop is proportional to the power consumption of the actuator, smooth, rounded bends are recommended if the space in which the fluid loop is installed allows for it.

Concluding Remarks

In general, the pressure drop tests of the circular and coiled fluid loop correspond best with the second helix approach. However, differences between the various methods are generally small. For rough sizing purposes it is therefore also possible to use the approach that treats the loop as if it were a straight tube, at the penalty of roughly a 10% inaccuracy. The straight tube approach also allows for specifying the channel surface roughness, so for turbulent flow in a non-smooth channel, this method is preferred.

In this case, even for square configurations with smooth corner bends with a radius of at least ~3 times the channel diameter, the second helix approach and the straight tube approach can be applied in the same way. However, for a square configuration with sharp elbows, the bend approach should be used with the recommended K-factor of 1.2. Sharp elbows increase the viscous friction significantly (by approximately a factor 2 in this case), so they should be avoided if possible.

5.3.4 Power Consumption

The total power consumption measurements make it possible to calculate the overall electrical pumping efficiency, by dividing the useful component of the power consumption purely due to viscous friction by the total measured input power. Because the aim of this dissertation is developing a generically applicable sizing model that can be used for all types of loops, pumps and fluids, characterizing this one non-ideal gear pump is not of particular interest. They are nevertheless useful, because they confirm that pressure and power measurements were made consistently, and give an efficiency value for assumptions made in section 5.5.

The electrical efficiency curves of the pump are plotted in Figure 5-18 by inserting the measured electrical power consumption and respective pressure drop at various flow rates into equation 5.5. The graph shows that the efficiency increases faster for lower flow rates. Although the volumetric losses are comparatively high at lower flow rates, the internal viscous, mechanical and electrical losses in the pump are less, which results in a higher overall efficiency. [72]

$$\eta = \frac{\Delta p Q}{P_{elec,in}} \qquad 5.5$$

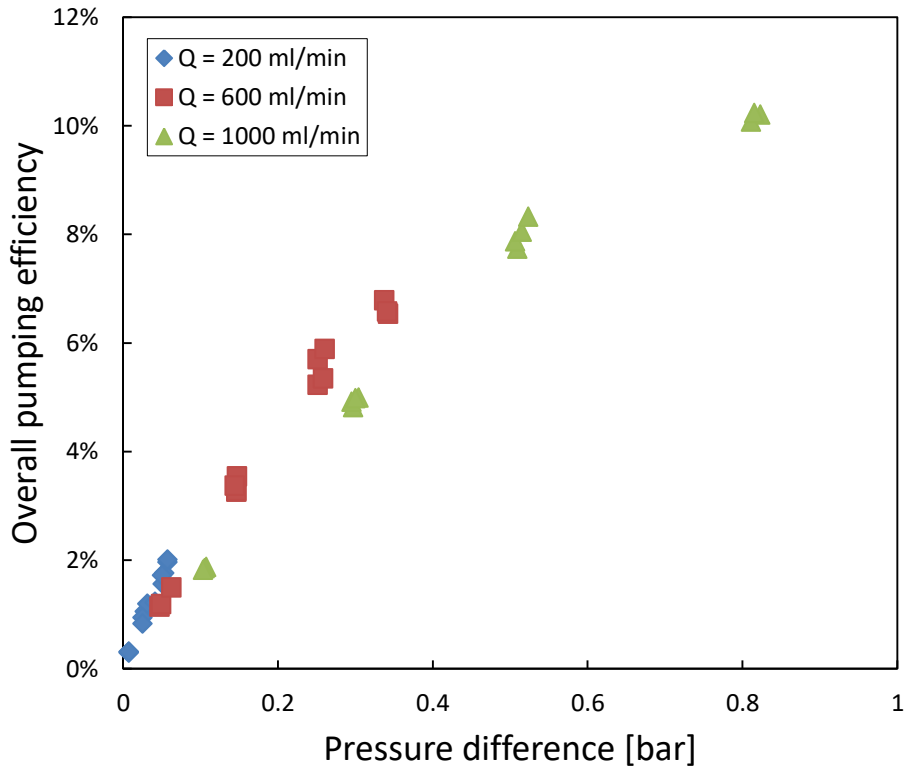

Figure 5-18 The derived pumping efficiency of the MGD1000F gear pump as a function of the pressure drop, at different flow rates.

5.3.5 Orbital Disturbance Model

The orbital disturbance model is an optional, auxiliary part of the sizing model that is developed to formulate fluid loop requirements based on the envisioned mission. The user interface is shown in Figure 5-19. Verification is done by feeding values of real missions into the model, and comparing the resulting actuator requirements from the model to the PPs of the real reaction wheels on board the satellite. This is done based on many assumptions and simplifications, so it should be treated as indicative at best. Therefore, the model is deemed verified when the results correspond to the real missions within the order of magnitude (factor 10 or less, but preferably a factor 3 or less). Table 5-5 shows the considered missions, their used reaction or momentum wheels, and the formulated angular momentum requirement by the model. Only angular momentum values are used to verify the model, because the torque values (1) are not often published, and (2) vary too much between missions under slew requirements, pointing accuracy requirements and other control torque margins, to allow for generalizing the results.

The assumptions on which the verification calculations are based are as follows.

- The formulated angular momentum requirement is based on a momentum dump manoeuvre after 10 orbits.
- The offset of the centre of solar and aerodynamic pressure to the CG is 10% of the average satellite length.
- If not available in the sources, the area of externally mounted solar panels is estimated based on images of the deployed satellite.
- The average satellite drag coefficient is set at a typical value of 2.3. [7]
- The average satellite reflectance factor is set at 0.7.

As shown in Table 5-5, the angular momentum requirements formulated by the model generally lie reasonably close to that of the actuator used; all within the same order of magnitude. Especially in the small satellite range between 10 kg and 200 kg the deviation factor is small (less than a factor of 2). Larger deviations can be caused by one or more of the following reasons:

- Any of the assumptions listed above could be incorrect; especially the amount of orbits between momentum dump moves can vary widely per mission.
- The calculated worst-case scenario could be much higher than is assumed, but can only become clear after more detailed orbital disturbance simulations.
- There could be special requirements for continuity of operations, such as for the BRITE satellite, whose mission is to make long-duration astronomical observations.

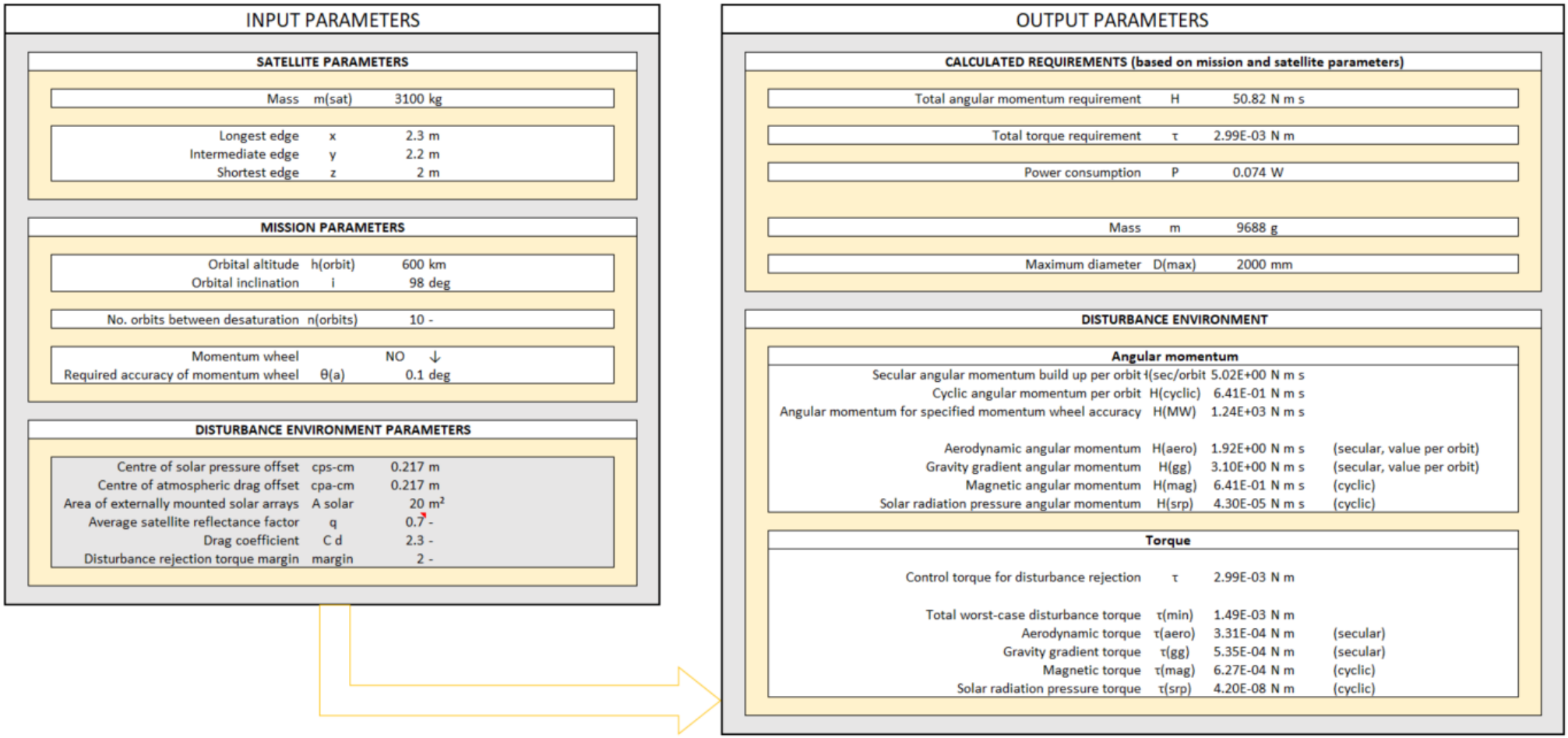

Figure 5-19 The user interface of the orbital disturbance model that calculates attitude actuator requirements based on the satellite and mission parameters. It combines all equations described in section 2.1.3.

Table 5-5 Data of various satellite missions and their reaction wheels that are used as benchmarks to verify the orbital disturbance model.

Mission	Ref	Sat. mass [kg]	Dimensions [cm³]	Solar panel area [m²]	Average altitude [km]	Inclination [deg]	Application	Angular momentum [Nms]	Suggested angular momentum [Nms]	Deviation factor
Zacube-1		1.2	10x10x10	0	640	98	1 axis	0.0017	0.0005	-3.4
BRITE Poland 2		7	20x20x20	0	610	98	3 axis	0.03	0.004	-7.5
HAUSAT 2		25	40x32x32	0	650	98	Momentum[1]	0.09	0.15	+1.6
INDEX		72	72x62x62	1.5	630	98	Momentum[2]	0.5 nom, 1 max	0.42	-1.2
Skysat 1 & 2		83	80x80x80	0	580	98	3 axis	0.18	0.24	+1.3
Orbcomm 2		172	103x84x50	2	750	52	3 axis	0.65	1.26	+1.9
Quickbird 2		1100	300 x Ø160	5	450	97	3 axis	20	104	+5.2
Fermi Telescope		4300	290x200x200	10	530	26	3 axis	50	179	+3.58
Turksat 3A		3100	230x220x200	20	35,786	0	3 axis	12	N/A[3]	N/A[3]

[1] Mounted on the pitch axis, with a yaw/roll accuracy of 3 degrees.

[2] Mounted on the roll axis, with a /pitch/yaw accuracy of 0.1 degrees.

[3] GEO satellites yield invalid results.

GEO missions are also assessed, but the results are not satisfactory. Firstly, an unrealistically large gravity gradient torque remains, while it should be around 2 orders of magnitude smaller than the solar radiation torque (which is the dominant disturbance at this altitude). Second, the angular momentum build-up due to the solar radiation torque is not properly translated into the angular momentum requirement, because the model unrealistically assumes an ideally cyclic solar radiation torque that cancels out after an orbit. Hence, the model cannot be used for GEO missions. However, this is not seen as a huge shortcoming, because (1) there are far fewer GEO missions than LEO missions, and (2) the used actuators in GEO have very little variation among them (all in the range of 10 – 50 Nms), which makes it easier to estimate a requirement based on comparable previous missions.

In conclusion, the disturbance model is deemed useful for early sizing purposes. As validated by NSS, customers often do not know exactly what their requirements should be. This model helps to determine the order of magnitude of the requirement, and to see what components and variables make up the requirement. It can also help to understand what products are suitable for which target satellite market.

5.4 Sizing Model Validation

The validation of the sizing model is done in two ways. Firstly, a meeting was held with the potential end users at NSS, to discuss whether the user interface meets the expectations. This was done with James Barrington-Brown (CEO), Leehandi De Witt (sales), and Johann Joubert (engineering manager). Second, it is tested by applying it to various missions.

In general, the model and its interface (Figure 5-20) had the functionality that was expected, although some improvements were made as a result of the meeting. Firstly, a user manual was made to guide the inexperienced user through the process (see Appendix 5). Minor tweaks were made to make the user interface clearer and easier to use. This included separating the fluid loop design model, the orbital disturbance environment model, and all the intermediate parameters on different worksheets. Also, winding the loop in a helix is no longer given as an option, since it is found that it is an integral part of the sizing process of a fluid loop. When a simple design with one coil is required, this can be constrained.

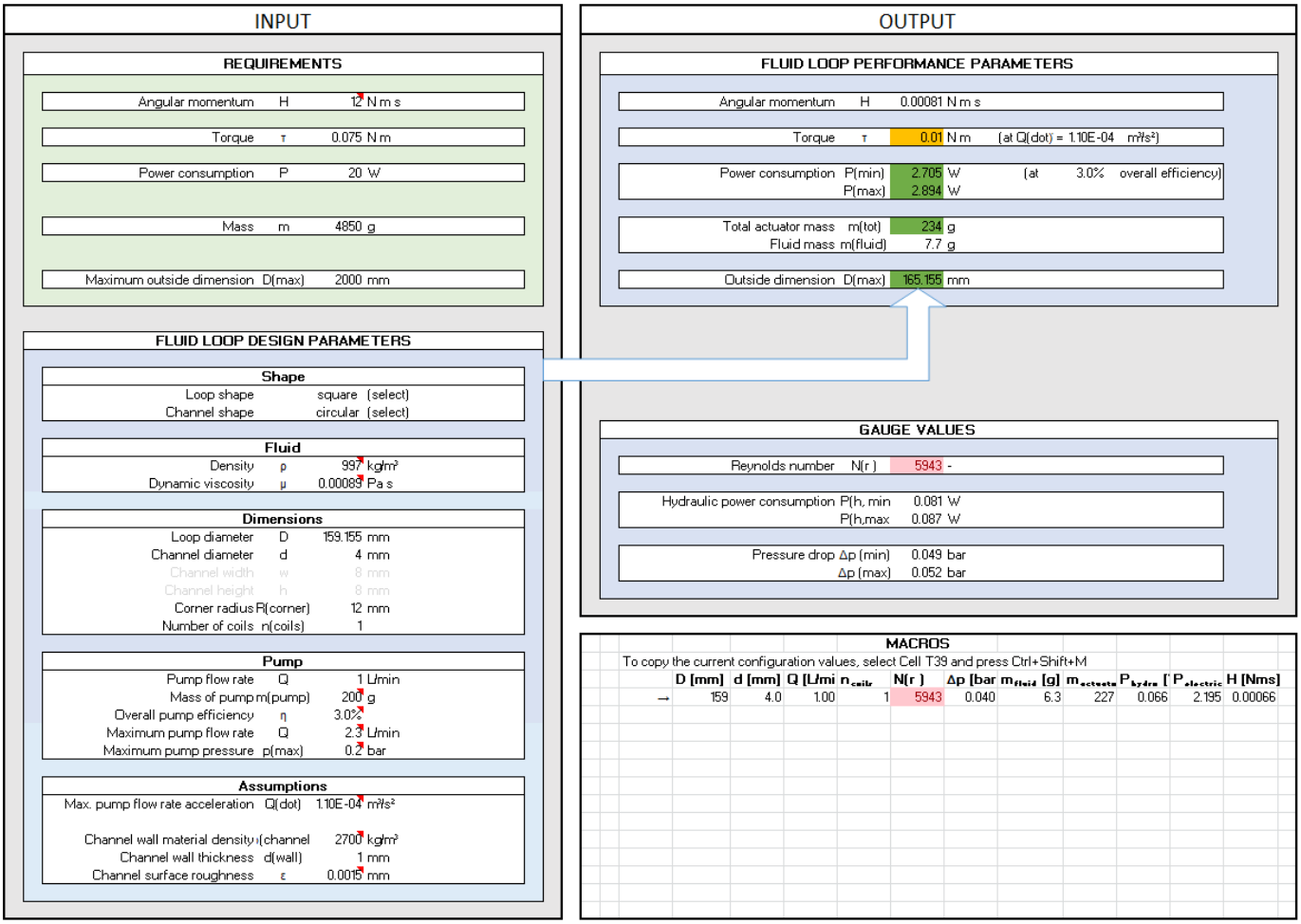

Figure 5-20 The user interface of the fluid loop sizing model. The user can input design parameters that result in the performance parameters of the fluid loop, which can then be compared to the set requirements. Using the Excel Solver function allows for optimization of the design parameters.

Validation was also done by applying the sizing model on various missions listed in Table 5-6, in order to gain user experience, to discover and resolve bugs, and to create many cases where the PPs of various fluid loops can be realistically compared to reaction wheels on actual missions. For each mission, a fluid loop was sized to meet the angular momentum and power consumption of the used reaction wheel, and optimized for mass using the Solver function in the Excel model. The results are described in Section 5.5. This exercise revealed some improvements to be made.

Some of the improvements were made to save time. Looking up reference values for the properties of reaction wheels, fluids and pumps has been simplified by introducing a lookup table in the comments of the relevant cells that appears when hovering over the cell. Copying down the configuration details after an optimization also costs much time (especially when dozens of scenarios are made). The Excel Macro feature was used to record the copying and formatting values into a table.

In particular, the optimization process with the Excel Solver function was found to be susceptible to bugs, and requires a workaround and the user's critical attention. The Solver optimizes a cell by changing the specified variable cells until it arrives at the best result. This means that also negative values are tried in these cells, which leads to mathematically invalid results and an error. This bug is (largely) resolved by setting a constraint for these values to be larger than zero. Simply entering the constraint "A1 >= 0" also results in a bug, because Excel automatically changes it to "A1 >= 1". To work around this, a cell *on the same sheet* is given an arbitrarily small number (e.g. A2=0.00001) and used as the constraining value, resulting in the constraint "A1 >= A2". This must be done for the parameters Loop diameter, Channel diameter, and Pump flow rate. On the very few occasions that negative values still end up in the variable cells (for some unknown reason), random realistic values should be entered in the respective cells until the Solver arrives at a solution.

There are cases in which the Solver cannot find a viable solution, because the constraints are fundamentally too tight. This occurs when, for instance, the pump pressure, flow rate and allowable dimensions are constrained to a small pump and a Nano satellite form factor while trying to match the specifications of a large reaction wheel. This is solved by relaxing the constraints.

The final implementation may have to be coded in Python to avoid these Excel bugs.

The made improvements have resulted in a verified and validated sizing model. Final validation is done by the end user at NSS, but this will take place after the writing of this dissertation.

5.5 Sizing Model Test

Finally, the verified and validated sizing model is applied to assess the fundamental potential of the fluid loop as a concept.

5.5.1 Method

The sizing model was used to optimize fluid loops for various real satellite missions (Table 5-6), so that they could potentially substitute the reaction wheel used. In the optimization scenarios, the satellite's reaction wheel's nominal or maximum angular momentum was matched by the fluid loop, within the respective power consumption of the wheel, while optimizing the mass of the fluid loop. The performance of the fluid loop is then compared to the used reaction wheel.

The optimizations were done within the pressure and flow rate capabilities of various COTS centrifugal pumps, gear pumps, and the custom MHD pump used for the flown FDA-A6 fluid loop actuator. For the smaller and bigger satellites, two hypothetical scaled MHD pumps were used as a substitute for the original. See Table 5-7 for the used pumps and their capabilities.

For each pump, scenarios were made for four different working fluids. It was assumed that the mechanical pumps can pump all the considered liquids, whereas the MHD pumps can only pump the conducting liquid metals Galinstan and mercury. Gear pumps are known to pump very high viscosities, but even the less-forgiving centrifugal pumps seem suitable for all considered fluids – Their kinematic viscosities (viscosity over density) are all well below the point where viscosity starts playing an appreciable role (9 cP versus 40 cP). [75] The lower kinematic viscosity of the liquid metals compared to water could even improve the pumping efficiency. Pumping liquid metals with mechanical pumps might bring some (electro-) chemical implications, but these were neglected in this analysis. The difference in electrical conductivity between Galinstan and mercury and thus the effectiveness of the MHD pump (mercury being three times less conductive) was also neglected for simplicity. The latter simplification reduces the accuracy of the mercury results significantly (because the considered pump is used with Galinstan), so this should be taken into account during assessment.

The scenarios initially had channels of 1 mm thick aluminium, with a smooth channel roughness of 0.0015 mm. The most promising scenarios with the least mass were individually optimized again in an attempt to further reduce the mass and are discussed in the next section. This was only done for the smaller variants and those with more than five coils; the others stay the same.

Table 5-6 Data of various missions that serve as requirements and boundaries for the fluid loop optimizations.

Satellite	Satellite Mass [kg]	Satellite Dimensions [cm³]	Used reaction wheel	Angular momentum [Nms]	Power consumption [g]	Actuator mass [g]
Zacube-1	1.2	10x10x10	CubeWheel S	0.00044 (0.00177)	0.08 (0.32*)	60
BRITE Poland-2	7	20x20x20	RW-0.03	0.03	0.3	185
Skysat-1	83	80x80x80	Microwheel 200	0.18	7	940
Turksat-3A	3060	280x220x200	Teldix 12	12	20	4850
Quickbird	1100	300x Ø160	Teldix 25*	25	20	6300

Table 5-7 Data of various COTS mechanical pumps and MHD pumps that serve as boundaries for the fluid loop optimizations.

	Max. flow rate [L/min]	Max. pressure [bar]	Overall Efficiency	Max. power [W]	Mass [g]	Assumed to be compatible with	Ref.
Centrifugal pump 1 (small)	0.4	0.1	6%	1.1	12	Water, SPT, Galinstan, mercury	[76]
Centrifugal pump 2 (medium)	1.5	0.17	6%	7.1	50	Water, SPT, Galinstan, mercury	[77]
Centrifugal pump 3 (large)	5	0.25	10%	20.8	200	Water, SPT, Galinstan, mercury	[78]
Gear pump 1 (small)	0.01	0.7	2%	0.6	40	Water, SPT, Galinstan, mercury	[79]
Gear pump 2 (pressure)	0.2	7	10%	23.3	200	Water, SPT, Galinstan, mercury	[80]
Gear pump 3 (flow)	1	1.5	10%	25.0	200	Water, SPT, Galinstan, mercury	[81]
MHD pump 1 (scaled down flow rate)	0.5	0.04	3%	1.0	25	Galinstan, mercury	
MHD pump 2 (used in flown FDA-A6)	2.3	0.04	3%	5.1	100	Galinstan, mercury	[28]
MHD pump 3 (scaled up pressure)	2.3	0.2	3%	25.6	200	Galinstan, mercury	

Smaller loops can have their wall thickness reduced to 0.5 mm aluminium, because their short length is assumed to provide enough rigidity. Loops with more than five coils are changed to an arbitrary plastic that is suitable for space, because (1) the lighter plastic reduces the mass of the many coils, and (2) plastic tubing is seamless for longer lengths, which reduces the chance of leaks. Preventing leaks is considered to be the single most important part of the design of a pumped fluid loop for space applications. [82] The issue of rigidity and micrometeoroids puncturing the plastic could be resolved by wrapping the bundle of coils in an impact-resistant material, such as Kevlar. The mass of this is neglected, but some extra margin should be taken into account for this. Figure 5-21 shows how this configuration would fit in the satellite structure.

The details of all first-iteration optimizations are compiled in tables in Appendix 6. The second-iteration optimizations are discussed in Section 5.5.2 below.

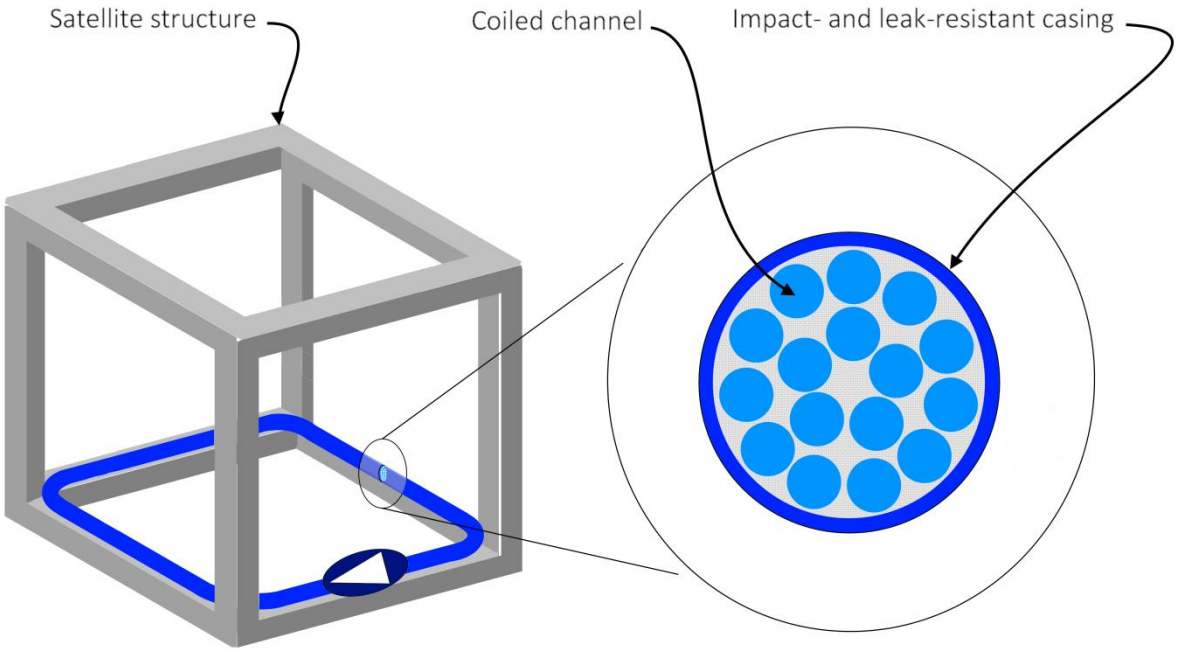

Figure 5-21 A suggested fluid loop configuration – a coiled square loop with rounded bends along the outer perimeter of the satellite. It has optimized geometry, light channel walls, and an impact- and leak-resistant outer casing, making it mass-efficient and safe from leaks.

5.5.2 Optimizations

This section presents the best results of the optimizations done for a variety of missions ranging from 1 to 3000 kg. All optimizations can be found in Appendix 6. It was also attempted to optimize fluid loops to replace momentum wheels, but their inherently high angular momentum compared to the satellite dimensions make it impossible for the fluid loop to be a viable competitor to momentum wheels.

Zacube-1

#	Pump	Fluid	D [mm]	D [mm]	Q [L/min]	n_{coils}	Nr	Δp [bar]	m_{fluid} [g]	m_{total} [g]	P_{hydro} [W]	$P_{electric}$ [W]	H [N m s]
Reaction wheel for comparison: CubeWheel S										60		0.320	0.00177
1	Centr. 1	H2O	96	2.1	0.12	7	1354	0.096	9.2	41	0.019	0.320	0.00177
2	MHD 1	Gal.	96	2.6	0.10	3	2228	0.040	38.5	78	0.007	0.227	0.00177

The optimizations above show that using a fluid loop on a 1U CubeSat is achievable within the power and mass constraints. Because CubeSats often have a lifetime in the order of weeks or months, even using the small COTS centrifugal pump with a lifetime of one year is feasible, provided that it can survive the launch and orbital environment. However, besides mass and power budgets, a satellite this small has very stringent volume constraints. Therefore, on this scale the small reaction wheel (28x28x26 mm) is deemed more useful than a fluid loop that has to be coiled multiple times, which takes up too much space. Lower or very specific angular momentum requirements that cannot be met by the COTS reaction wheels could improve the eligibility of the scalable fluid loop.

BRITE Poland-2

#	Pump	Fluid	D [mm]	D [mm]	Q [L/min]	n_{coils}	Nr	Δp [bar]	m_{fluid} [g]	m_{total} [g]	P_{hydro} [W]	$P_{electric}$ [W]	H [N m s]
Used reaction wheel: RW-0.03										185		0.3	0.03
1	Centr. 1	H2O	193	4.8	0.39	8	1951	0.028	105.9	410	0.018	0.300	0.03

The reaction wheels used in the BRITE constellation have a high angular momentum relative to their low power consumption of only 0.3 W. To match this, a fluid loop needs a large channel diameter to produce as little viscous resistance as possible, while it requires many coils to match the angular momentum – both increase the mass above the acceptable level. Therefore, there are no fluid loop configurations that could realistically replace the reaction wheels of the satellites in

the BRITE constellation. At this scale, a fluid loop can hardly compete with a reaction wheel, because the loop diameter (which is quadratically responsible for the angular momentum) is too constrained by the small satellite. A fluid loop could still work for other similarly-sized missions with a lower angular momentum requirement, but faces the same volume challenges as mentioned for the Zacube-1.

Skysat-1

#	Pump	Fluid	D [mm]	D [mm]	Q [L/min]	n_{coils}	Nr	Δp [bar]	m_{fluid} [g]	m_{total} [g]	P_{hydro} [W]	$P_{electric}$ [W]	H [N m s]
Used reaction wheel: Microwheel 200										940		7	0.18
1	Centr. 2	H2O	794	3.7	0.35	5	2201	0.170	172.2	480	0.098	1.632	0.18
2	Gear 3	H2O	796	2.0	0.18	7	2091	1.500	68.9	832	0.438	4.375	0.18
3	MHD 2	Gal.	793	4.9	0.15	3	1737	0.040	1144.5	1717	0.010	0.332	0.18
4	MHD 3	Gal.	794	4.2	0.33	2	7031	0.200	562.8	1041	0.112	3.722	0.18

The prospects for a fluid loop on the Skysat-1 look much better. Twelve out of the twenty initial scenarios have a lower total mass than the used reaction wheel, and thirteen have a lower power consumption. In this case, the luxurious situation exists where all considered pumps have a feasible solution, the most interesting of which are shown in the table above.

Configuration 1 has the lowest overall mass, at close to half the mass of the used reaction wheel; 0.5 kg of the mass budget is left for leak prevention or pump improvements. It also has a power consumption that is almost four times lower, so the uncertainty in the pumping efficiency assumption would need to be very large if it were to decrease the fluid loop's eligibility.

Configuration 2 has the lowest fluid mass, and uses the gear pump that was used in the fluid loop prototype. The gear pump's higher pressure can push liquid through a much narrower channel, which reduces the fluid mass significantly. The higher pump mass and more coils do have a negative effect on the total mass.

The first two configurations are based on COTS pumps that are not meant for space. The strength of configuration 3, however, is that it is based on an existing, space-qualified MHD pump. [28] Hence, it is possible to realize this configuration on a relatively short term, with the least research, development and qualification costs. It also has no moving parts, which makes it a reliable and long lifetime pump. However, reverse calculations show that this pump does not provide a very high pressure differential. Hence, the channel diameter is somewhat large, and with it the fluid mass. The low pressure differential puts a limit on the hydraulic power it can produce, and therefore its electric power consumption. At 0.332 W, there is a lot of room for

increasing the pressure by increasing the voltage and current, within the power budget of the used reaction wheel. This means that this mass can be optimized further, depending on the produced pressure at higher voltages.

Alternatively, configuration 4 proposes a similar MHD pump, but with a five times higher pressure capability. This pump does not exist, but could be scaled up from the existing pump. Although this scaling will come at a mass penalty, the channel diameter and thus the fluid mass can be reduced significantly. This configuration could therefore compete with the used reaction wheel on all fronts.

Turksat-3A

#	Pump	Fluid	D [mm]	D [mm]	Q [L/min]	n_{coils}	Nr	Δp [bar]	m_{fluid} [g]	m_{total} [g]	P_{hydro} [W]	$P_{electric}$ [W]	H [N m s]
Used reaction wheel: Teldix 12										4850		20	12
1	Gear 2	H2O	1996	2.4	0.19	22	1888	6.390	765.5	3003	2.000	20.000	12
2	Gear 3	H2O	1994	3.7	0.36	16	2299	1.500	1346.5	3604	0.889	8.887	12

Quickbird

#	Pump	Fluid	D [mm]	D [mm]	Q [L/min]	n_{coils}	Nr	Δp [bar]	m_{fluid} [g]	m_{total} [g]	P_{hydro} [W]	$P_{electric}$ [W]	H [N m s]
Used reaction wheel: Teldix 25										6300		20	25
1	Gear 2	H2O	1595	2.6	0.19	39	1764	6.162	1339.3	4650	2.000	20.000	25
2	Gear 3	H2O	1594	4.1	0.38	28	2219	1.500	2296.4	5608	0.947	9.473	25

As can be seen in both of the above examples, the only eligible configurations for missions with a high angular momentum requirement are actuated by high pressure pumps. The above configurations match the used reaction wheel well in power consumption and mass; any mass budget surpluses (approximately a kilogramme in all cases) could be used for leak prevention and pump improvements.

The optimizations show that as the fluid loop has a higher angular momentum requirement, the better configurations all tend to have a low flow rate, many coils, and a very high pressure drop. This is because increasing the number of coils increases the power consumption linearly, while increasing the flow rate increases the power consumption quadratically. Hence, at these higher requirements it is more energy efficient to scale by increasing the number of coils than by

increasing the flow rate. The length of the extra coils increases the pressure drop. The Solver then optimizes for mass by decreasing the channel diameter, which increases the pressure drop too. It does this until it runs into the pump's maximum pressure differential or power limit. In conclusion, high angular momentums can only be achieved efficiently with high pressure pumps.

5.5.3 Final Comments on Pumping

It must be noted that the considered mechanical pumps are not space-qualified – they are not designed for launch loads, their materials and bearings are not meant to operate in the orbital thermal vacuum environment, and their rated lifetime (at atmospheric pressure) does not exceed one to two continuous years of running. [81], [83] The few space-qualified mechanical pumps that do exist (mostly for thermal management systems) have an unnecessarily high flow rate, and are too large, heavy, and consume too much power to be used in a fluid loop. [84]–[87] Therefore, data of the more properly sized conventional COTS pumps are used for the optimizations. This does imply that all scenarios with mechanical pumps are less realistic than the MHD scenarios. This is taken into account by allowing a large enough margin for an increase in pump mass for improvements.

All in all, very few pumps currently exist that are suitable for both the space environment and the fluid loop. The design and qualification for use in space is a long and complicated process, especially for mechanical pumps with their many components and moving parts. MHD pumps have no moving parts and are more easily scalable, and are therefore considered a good (if not the preferred) option, despite their lesser pressure capabilities.

For the further development and widespread application of fluid loops, focus must be put on the development of efficient, reliable, high-pressure, space-worthy pumps. This would lay the necessary base for fluid loops to even compete with reaction wheels. The pumps should preferably be scalable, so that the scalability of the fluid loop concept can also be fully exploited. This would make the fluid loop and its secondary advantages (such as high torque, reduced jitter, robustness and long lifetime) suitable for a wide variety of space missions.

6. Conclusions

A fluid loop attitude actuator promises advantageous performance over reaction wheels on many areas, including high torque, low power consumption, reduced jitter and higher reliability. However, these claims are strongly contradicted by the lack of interest in the concept. Therefore, this dissertation attempts to answer the question:

What is the fundamental potential of the fluid loop as an attitude actuator?

To compare the fluid loop to its competitors, a parametric sizing model is developed. It calculates the most important performance parameters (angular momentum, torque, power consumption, mass), based on the fluid loop's design parameters (loop geometry, fluid properties, pump capabilities). The model exploits the scalability of the fluid loop and allows for optimization based on customer requirements. The developed auxiliary orbital disturbance model can also formulate initial requirements based on satellite and mission parameters.

To verify the theory that underpins the model, a fluid loop prototype is designed and developed that can be configured into a circular, square or helical loop with varying major diameters and channel diameters. To verify the theorized power consumption due to viscous friction, the prototype allows for measuring its components – the flow rate and pressure drop over the loop. To verify the theorized angular momentum of the fluid loop, in particular that of the unknown square and helical configurations, a spherical air bearing was designed and developed for dynamic near-frictionless tests.

Air bearing tests with different fluid loop configurations show that the developed sizing model can be applied with confidence. In general, the angular momentum of the fluid loop scales with loop length (among other parameters). Consequently, a square loop will have a slightly higher angular momentum than a similarly sized circular loop, and a helical loop increases the angular momentum linearly with each coil. These results improve the applicability of the fluid loop – the

loop can be fitted along the perimeter of a satellite bus in any shape, while coiling (in any shape) allows for easy scaling. Unintuitively, increasing the inertial mass by increasing the channel diameter does not have an effect on the angular momentum due to continuity.

Pressure drop measurements with different fluid loop configurations showed which calculation methods for viscous friction losses are best suited for which configuration. These losses are directly related to the power consumption of the actuator. Measurements from the circular and coiled fluid loop correspond best with the second helix approach from Jove. [58] However, differences between the various methods are generally small (up to ~10%), so all methods can be used for initial sizing. For more than 10 coils the Jove approach should be used. The Darcy approach allows for specifying the channel surface roughness, so for turbulent flow in a non-smooth channel, this method is preferred. Even for square configurations with smooth bends with a radius of at least ~3 times the channel diameter, the Jove circular helix approach and the Darcy approach can be applied in the same way. However, for a square configuration with sharp elbows, the bend approach from Rennels should be used. [53] Sharp elbows increase the viscous friction significantly, so they should be avoided if possible.

The theory points out that the mass efficiency and the power efficiency (relative to the angular momentum) are fundamentally inversely related. Therefore, there are no "more-is-better" relations in sizing a fluid loop (except for the loop diameter, which should be maximized). This necessitates and justifies the developed sizing model.

Fluid loop optimizations are done for various satellite missions from 1 kg to 3000 kg. In most cases, the optimized fluid loops can match the angular momentum of the used reaction wheels within the power and mass budgets. Momentum-bias wheels are much more difficult to match. The results show that the fundamental potential of the fluid loop is different for small, medium, and large satellites.

Fluid loops can be used in very small satellites (± <20 kg) at similar or slightly worse power or mass performance. However, the volume constraints are too stringent at this scale. Unless the overall electrical efficiency of small pumps improves significantly, or the loop can be cleverly integrated into the satellite structure, the fluid loop cannot match the angular momentum density of wheels.

Medium-sized small satellites (± 20–500 kg) are suited best for the implementation of a fluid loop. The angular momentum requirements are not inhibitively high, while the larger

outside dimension allows for an efficiently shaped loop. Optimizations show that the reaction wheel's angular momentum can be matched by fluid loops, while using significantly less power. The mass of the fluid is low, but the mass of the channel should still be carefully minimized to fit within the mass budget.

Large satellites (± >500 kg) carry wheels with a much higher angular momentum. Fluid loops can potentially replace them, but require pumps with a very high pressure capability (>1 bar, but preferably higher) to stay within the power and mass budget. This is because it is more power efficient to scale up the angular momentum by coiling (which results in a linear increase in power consumption), rather than increasing the flow rate (which results in a quadratic increase in power consumption). At this scale the fluid mass is very low, but the many coils (20+) that are required to match the angular momentum make mass optimization of the channel essential to the fluid loop's potential to replace wheel-based actuators.

6.1 Limitations

The biggest limitations in the developed design model originate from the necessary assumptions that were made. The calculation of the fluid loop torque capability is based on a few reverse-calculated examples, and is therefore not addressed much. Tests from the flown actuator do point out that torque is exceptionally high, so it is assumed that a fluid loop sized for angular momentum has a high enough torque capability. The electrical efficiency assumptions necessary for the total power consumption calculations are somewhat more accurate as they are based on data sheets of actual pumps, but they are nevertheless approximate. It is also assumed that Galinstan is a Newtonian fluid, while it is reported to have non-linear properties in lower temperature ranges.

6.2 Recommendations

All in all, fluid loops have good potential to replace reaction wheels on satellites between approximately 20 and 500 kg, if the channel mass can be sufficiently optimized. With a high-pressure pump, larger satellites can also be accommodated for. However, the most promising optimizations are based on pumps for terrestrial applications, rated for atmospheric conditions and a lifespan of less than two years – the optimizations show the *potential*, but not the currently achievable performance.

Consequently, the real challenge for the widespread application of the fluid loop lies in developing a long-life, space-worthy, mass- and power-efficient, and preferably high-pressure

pump. The few space-rated pumps that currently exist are too large and consume much power relative to their flow rate. In addition, the design and qualification of pumps for use in space is a long and complicated process, especially for mechanical pumps with their many components and moving parts. Applying COTS terrestrial pumps or developing space-rated mechanical pumps is not unthinkable, but their inherent limitations improve the case for an MHD pump.

The existing MHD pump used in the TechnoSat has a high torque capability and thus potential. In addition, its low jitter and wear-free operation could make it useful for niche applications where reaction wheels are out of the question. In addition, it seems it is the only MHD pump currently available on this scale.

However, based on the published data of its nominal operation, it cannot by far produce a fluid loop that competes with a reaction wheel on all three of the most important performance parameters at the same time, i.e. angular momentum, power and mass.

A modification is recommended that sacrifices the pump's flow rate for a higher pressure differential – all optimization scenarios show that a flow rate of only 0.4 L/min or less is required instead of the current 2.3 L/min, while the current pressure capability limits its potential. Perhaps this is already possible with the existing design by simply increasing the voltage or viscous pressure load induced by the loop, but the pump's characteristics should be investigated before dedicating too many resources.

A good option is to collaborate with an (aerospace) micro-pump manufacturer. There might be unidentified manufacturers or those that offer custom solutions. This could be the path of least resistance towards a suitable pump.

Alternatively, a new pump could be developed. Emphasis should be put on electrical pumping efficiency, pressure capability, mass, and durability in space. Exact pump requirements can be formulated by using the optimization mode in the developed sizing model. In addition, it would be beneficial if the pump design is scalable, so that it allows for fully exploiting the scalability of the fluid loop concept. The latter would be most easily achievable with an MHD pump.

Several other recommendations follow from the findings in this dissertation.

The fluid loop is best employed in the shape of the satellite bus, with a loop diameter as large as possible to maximize the angular momentum and torque. The shape is likely square or

rectangular, in which case the corner bends should be continuous and slightly rounded to reduce viscous friction.

Leaking is a concern for mission designers, as it is a one-point failure. To mitigate this, a leak-proof loop and impact-resistant casing should be designed, complemented by a risk assessment method to determine to what degree micrometeoroids and orbital debris jeopardize the mission.

For a fluid loop with multiple coils, a recommended configuration to reduce mass is a bundle of coiled tubing with very light, thin walls, encased in one protective, impact-resistant outside casing.

One of the biggest traits of inertial attitude actuators over other actuators is their pointing accuracy. A big unknown is how accurately a fluid loop can control the attitude of a satellite. In addition, direct, non-intrusive flow rate measurement is difficult, which complicates the design or control aspect. Investigating a fine pointing strategy is therefore required; especially if the low jitter capability is to be exploited.

In conclusion, the fluid loop has the fundamental potential to replace reaction wheels in a wide variety of satellite missions with a mass of above approximately 20 kg, if effort is invested in developing a suitable pump, and if the fine pointing control aspect is addressed. This should be considered worthwhile, as the actuator comes with the advantages of high torque, low jitter, robustness, and a long lifetime. The scalability of the fluid loop can be fully exploited with the sizing model developed in this dissertation.

References

[1] C. Skocik, "Looking Back as Intelsat 603 Mission Ends in Satellite 'Graveyard,'" *Spaceflight Insider*, 2015. [Online]. Available: http://www.spaceflightinsider.com/space-flight-history/intelsat-603-deorbited/ . [Accessed: 26-Nov-2018].

[2] NASA, *STS-49 Intelsat-VI Recovery "Houson, I Think We've Got a Satellite."* 1992.

[3] C. Hall, "Introduction to Attitude Dynamics and Control (Presentation)." [Online]. Available: http://www.dept.aoe.vt.edu/~cdhall/courses/aoe4140/intro2adcs.pdf. [Accessed: 26-Nov-2018].

[4] NASA Jet Propulsion Laboratory, "An Early History of Satellites." [Online]. Available: https://www.jpl.nasa.gov/infographics/infographic.view.php?id=11182. [Accessed: 26-Nov-2018].

[5] Markley and Crassidis, *Fundamentals of Spacecraft Attitude Determination and Control*. Springer Space Technology Library, 2014.

[6] NASA, "Three Shuttle Astronauts Capturing Intelsat 603." [Online]. Available: https://www.nasa.gov/sites/default/files/thumbnails/image/s49-91-029.jpg.

[7] J. R. Wertz, D. F. Everett, and J. J. Puschell, Eds., *Space Mission Engineering: The New SMAD*. Microcosm Press, 2011.

[8] Y. Chang, S.-J. Kang, and B.-H. Lee, "Attitude Control Strategy for Hausat-2 with Pitch Bias Momentum System," in *20th IAA/USU Conference on Small Satellites*.

[9] R. Haviland, "Orientation Control for a Space Vehicle," US2856142A, 1956.

[10] T. Wyatt and C. Swet, "Combined Fluid Flywheel and Propulsion System for Spacecraft," US3862732A, 1973.

[11] R. Maynard, "Fluidic Momentum Controller," 4,776,541, 1988.

[12] T. Iskenderian, "Liquid Angular-Momentum Compensator," 1989.

[13] B. Lurie, A. Schier, and T. Iskenderian, "Fluid-Loop Reaction System," 5,026,008, 1991.

[14] A. Kelly, C. McChesney, P. Smith, S. Walenta, and C. Zaruba, "A Performance Test of a Fluidic Momentum Controller in Three Axes," 2004.

[15] R. Varatharajoo, "Approach for Combining Spacecraft Attitude and Thermal Control

Systems," *J. Spacecr. Rockets*, vol. 40, no. 5, p. 657, 2003.

[16] K. D. Kumar, "Satellite Attitude Stabilization using Fluid Rings," *Acta Mech.*, vol. 208, no. 1–2, pp. 117–131, 2009.

[17] Alkhodari and Varatharajoo, "H(2) and H(inf) Control Options for the Combined Attitude and Thermal Control System (CATCS)," *Adv. Sp. Res.*, vol. 43, no. 12, pp. 1897–1903, 2009.

[18] S. Xiao-Wei, "Small Satellite Attitude Control based on Mechanically Pumped Fluid Loops," in *6th IEEE Conference on Industrial Electronics and Applications*, 2011.

[19] J. Tayebi and A. Soleymani, "A Comparative Study of CMG and FMC Actuators for Nano Satellite Attitude Control System-Pyramidal Configuration," in *7th International Conference on Recent Advances in Space Technologies (RAST)*, 2015.

[20] M. Mesurolle, "Finite Difference 2D Model of a Magnetohydrodynamic Inertial Actuator," in *NUMELEC*, 2015.

[21] A. Salvati and F. Curti, "MHD Reaction Wheel for Spacecraft Attitude Control: Configuration and Lumped Parameter Model," in *2nd IAA Conference on Dynamics and Control of Space Systems (DYCOSS)*, 2014.

[22] F. Curti, "Magneto-Hydro-Dynamics Liquid Wheel Actuator for Spacecraft Attitude," 2017.

[23] TU Berlin, "Fluid Dynamic Actuator Publications." [Online]. Available: https://www.raumfahrttechnik.tu-berlin.de/menue/forschung/aktuelle_projekte/fda/parameter/en/. [Accessed: 26-Nov-2018].

[24] NASA, "Technology Readiness Level Definitions." [Online]. Available: https://www.nasa.gov/pdf/458490main_TRL_Definitions.pdf. [Accessed: 26-Nov-2018].

[25] C. Casteras, Y. Lefevre, and D. Harribey, "MHD inertial actuator patent," US20150027244A1, 2012.

[26] Nobari, "Attitude Dynamics and Control of Satellites with Fluid Ring Actuators," McGill University, 2013.

[27] D. Noack, "Laboratory Investigation of a Fluid-Dynamic Actuator Designed for CubeSats," *Acta Astronaut.*, vol. 96, no. March-April, pp. 78–82, 2014.

[28] D. Noack, J. Ludwig, P. Werner, M. Barschke, and K. Brieß, "FDA-A6 – A Fluid-Dynamic Attitude Control System for TechnoSat," 2017.

[29] S.-Y. Tang, K. Khoshmanesh, V. Sivan, P. Petersen, and A. P. O'Mullane, "Liquid Metal Enabled Pump," *Proc. Natl. Acad. Sci.*, vol. 111, no. 9, pp. 3304–3309, 2014.

[30] "Orbital Speed," *Wikipedia*. 2018.

[31] C. Hall, "Reference Frames for Spacecraft Dynamics and Control (Presentation)." [Online]. Available: http://www.dept.aoe.vt.edu/~cdhall/courses/aoe4140/refframes.pdf. [Accessed: 26-Aug-2011].

[32] R. Fitzpatrick, "Moment of Inertia Tensor," 2011. [Online]. Available: http://farside.ph.utexas.edu/teaching/336k/Newtonhtml/node64.html. [Accessed: 26-Nov-2018].

[33] "Angular Momentum," *Wikipedia*. 2018.

[34] Mortari, "Attitude Dynamics: Disturbance Torques (presentation)." [Online]. Available: http://aeweb.tamu.edu/mortari/aero423/Chapter 8 - Part 1 (Disturbance torques).pdf . [Accessed: 26-Nov-2018].

[35] "Design Module for a Spacecraft Attitude Control System," 2003.

[36] NASA, "NRLMSISE-00 Atmosphere Model." [Online]. Available: https://ccmc.gsfc.nasa.gov/modelweb/models/nrlmsise00.php. [Accessed: 26-Nov-2018].

[37] "Properties of Standard Atmosphere." [Online]. Available: http://www.braeunig.us/space/atmos.htm. [Accessed: 26-Nov-2018].

[38] D. A. Vallado and D. Finkleman, "A Critical Assessment of Satellite Drag and Atmospheric Density Modeling," *Acta Astronaut.*, vol. 95, no. February-March, pp. 141–165, 2014.

[39] J. T. Emmert, "A Long-Term Data Set of Globally Averaged Thermospheric Total Mass Density," *J. Geophys. Res.*, vol. 114, 2009.

[40] R. O. of Belgium, "Monthly and Smoothed Sunspot Number," 2018. [Online]. Available: http://sidc.oma.be/silso/monthlyssnplot. [Accessed: 26-Nov-2018].

[41] S. A. Rawashdeh, "Cubesat Aerodynamic Stability at ISS Altitude," in *26th AIAA/USE Conference on Small Satellites*.

[42] "Diple Model of the Earth's Magnetic Field," *Wikipedia*. 2017.

[43] Federal Aviation Administration, "4.3.1 Space Vehicle Control Systems," in *Advanced Aerospace Medicine On-line*, 2018.

[44] J. C. Springmann and J. W. Cutler, "Magnetic Sensor Calibration and Residual Dipole Characterization for Application to Nanosatellites," in *AIAA/AAS Astrodynamics Specialist Conference*, 2010.

[45] A. Ketsdever, "Space Mission Geometry (presentation)." [Online]. Available:

http://eas.uccs.edu/~aketsdev/MAE 5595_files/Lesson 2.pdf . [Accessed: 26-Nov-2018].

[46] Merriam-Webster, "Fluid (etymology)." [Online]. Available: https://www.merriam-webster.com/dictionary/fluid . [Accessed: 26-Nov-2018].

[47] "Rheology (etymology)," *Wiktionary*. [Online]. Available: https://en.wiktionary.org/wiki/rheology#Etymology. [Accessed: 26-Nov-2018].

[48] Lackner, "The Concept of Viscosity." [Online]. Available: http://www.columbia.edu/itc/ldeo/lackner/E4900/Themelis3.pdf. [Accessed: 26-Nov-2018].

[49] R. L. Mott, *Applied Fluid Dynamics*. Pearson, 2006.

[50] The Chemical Engineers' Resource, "Solving the Colebrook Equation for Friction Factors." [Online]. Available: http://www.eng.auburn.edu/~tplacek/courses/3600/colebrook . [Accessed: 26-Nov-2018].

[51] S. Beck and R. Collins, "Moody Diagram," *Wikimedia Commons*. 2008.

[52] "Hydraulic Diameter," *Wikipedia*. 2018.

[53] D. C. Rennels and H. M. Hudson, *Pipe Flow - A Practical and Comprehensive Guide*. John Wiley & Sons, Inc, 2012.

[54] C. Beck, "Discussion: 'Pressure Losses in Smooth Pipe Bends,'" *J. Basic Eng.*, vol. 82, no. 1, pp. 140–142, 1960.

[55] P. L. Spedding, E. Benard, and G. M. McNally, "Fluid Flow through 90 Degree Bends," *Dev. Chem.Eng. Miner. Process.*, vol. 12, no. 1–2, pp. 107–128, 2004.

[56] Beij, "Pressure Losses for Fluids in 90-degree Pipe Bends," *J. Natl. Bur. Stand.*, vol. 21, 1938.

[57] R. P. Benedict, *Fundamentals of Pipe Flow*. John Wiley & Sons, Inc, 1980.

[58] Jove, "Piping Networks and Pressure Losses." [Online]. Available: https://www.jove.com/science-education/10389/piping-networks-and-pressure-losses.

[59] KSB, "Pump Power Output." [Online]. Available: https://www.ksb.com/centrifugal-pump-lexicon/pump-power-output/191446. [Accessed: 26-Nov-2018].

[60] M. L. Culpepper, "How a Gear Pump Works." [Online]. Available: http://web.mit.edu/course/2/2.972/OldFiles/www/report-gear_pump.html. [Accessed: 26-Nov-2018].

[61] G. Bockmann and G. Mussbacher, "Requirements Verification and Validation (presentation)." [Online]. Available: http://csis.pace.edu/~marchese/CS775/Lectures/775L12.ppt. [Accessed: 26-Nov-2018].

[62] "Trichloromonofluoromethane," *PubChem*. [Online]. Available: https://pubchem.ncbi.nlm.nih.gov/compound/Trichlorofluoromethane#section=MeSH-Entry-Terms. [Accessed: 26-Nov-2018].

[63] Geoliquids, "MSDS Sodium Polytungstate (data sheet)." 2012.

[64] "Galinstan," *Wikipedia*. 2018.

[65] Engineering Toolbox, "Mercury Properties." [Online]. Available: https://www.engineeringtoolbox.com/mercury-d_1002.html. [Accessed: 26-Nov-2018].

[66] A. M. Turdakozhaeva, "Temperature Dependence of the Dynamic Viscosity of Liquid Mercury," *Russ. J. Phys. Chem. A*, vol. 87, no. 9, pp. 1595–1597, 2013.

[67] "Email correspondance with Dr. Sebastian Kamps of TC-Tungsten Compounds GmbH." .

[68] B. Casey, "Hydraulic Pumps and Motors: Considering Efficiency," *Machinery Lubrication*, 2011. [Online]. Available: https://www.machinerylubrication.com/Read/28430/hydraulic-pump-motors-maintenance.

[69] Landwise, "Pump Efficiency Guidelines." [Online]. Available: http://www.landwise.org.nz/wp-content/uploads/EEC1427-Pump-Efficiency-Guidelines-2_0.pdf. [Accessed: 26-Nov-2018].

[70] T. Shigemitsu, J. Fukutomi, K. Kaji, and T.Wada, "Performance and Internal Flow Condition of Mini Centrifugal Pump with Splitter Blades," *Int. J. Fluid Mach. Syst.*, vol. 6, no. 1, 2013.

[71] ROTECH, "What Factors Affect the Efficiency of a Centrifugal Pump?" [Online]. Available: http://www.rotechpumps.com/what-factors-affect-the-efficiency-of-a-centrifugal-pump. [Accessed: 26-Nov-2018].

[72] Z. Zeleny, "Gear Pump for Low Power Output IRC - an Efficiency Analysis," *Energy Procedia*, vol. 129, no. September, pp. 1002–1009, 2017.

[73] NASA, "Verification Module - Space Systems Engineering, v1.0 (presentation)." [Online]. Available: https://webcache.googleusercontent.com/search?q=cache:Lr8haCUN9HcJ:https://spacese.spacegrant.org/SEModules/Verifications/23.Verification_Module_V1.0.ppt+&cd=15&hl=en&ct=clnk&gl=za.

[74] B. Casey, "Hydraulic Pumps an Motors: Considering Efficiency," *Machinery Lubrication*, 2011. [Online]. Available: https://www.machinerylubrication.com/Read/28430/hydraulic-pump-motors-

maintenance. [Accessed: 26-Nov-2018].

[75] R. W. Whitesides, "Selecting a Centrifugal Pump to Handle a Viscous Liquid," 2008. [Online]. Available: https://pdhonline.com/courses/m102/m102content.pdf . [Accessed: 26-Nov-2018].

[76] TCS Micropumps, "M200 Series - Data Sheet." [Online]. Available: https://micropumps.co.uk/DATA/pdf/DS03 - M200 Data Sheet REV 5.compressed.pdf. [Accessed: 26-Nov-2018].

[77] TCS Micropumps, "M410 Series - Data Sheet." [Online]. Available: https://micropumps.co.uk/DATA/pdf/DS26 - M410 Data Sheet REV 1 SMALL.pdf.

[78] TCS Micropumps, "M510 S - Data Sheet." [Online]. Available: https://micropumps.co.uk/DATA/pdf/DS32 - M510 S Data Sheet REV 2 SMALL.pdf. [Accessed: 26-Nov-2018].

[79] I. Flight Works, "C-Series MODEL 2012-C25/C31." [Online]. Available: http://products.flightworksinc.com/Asset/Product-Data-Sheet--2012-C25-C31-.pdf. [Accessed: 26-Nov-2018].

[80] TCS Micropumps, "MG1000 P - Data Sheet." [Online]. Available: https://micropumps.co.uk/DATA/pdf/DS30 - MGD1000 P Data Sheet REV 2.pdf. [Accessed: 26-Nov-2018].

[81] TCS Micropumps, "MG1000 F - Data Sheet." [Online]. Available: http://micropumps.co.uk/DATA/pdf/DS31 - MGD1000 F Data Sheet REV 2.pdf. [Accessed: 26-Nov-2018].

[82] P. Bhandari and NASA Jet Propulsion Laboratory, "Mechanically Pumped Fluid Loops for Spacecraft Thermal Control: Past, Present & Future (presentation)," in *15th Annual Thermal 7 Fluid Analysis Workshop*, 2004.

[83] TCS Micropumps, "M100 range." [Online]. Available: http://micropumps.co.uk/TCSM100range.htm. [Accessed: 26-Nov-2018].

[84] CASCON, "DI Water Pump for International Space Station." [Online]. Available: https://www.casconpump.com/product/international-space-station/. [Accessed: 26-Nov-2018].

[85] PDT, "Aerospace Pumps." [Online]. Available: https://www.pd-tech.com/products/thermal-management-components/pumps/. [Accessed: 26-Nov-2018].

[86] KNF USA, "KNF Pumps Launched into Space," 2018. [Online]. Available: https://blog.knfusa.com/2018/10/18/knf-pumps-launched-into-space/.

[87] KNF USA, "KNF Pumps Launched into Space," 2018. [Online]. Available: https://www.knf.com/?type=5600&fileref=5087%0A. [Accessed: 26-Nov-2018].

[88] A. Scholz, "Implementation of Advanced Attitude Determination and Control Techniques into a Nanosatellite," National Cheng Kung University.

[89] J. Armstrong, C. Casey, G. Creamer, and G. Dutchover, "Pointing Control for Low Altitude Triple Cubesat Space Darts," in *Small Satellite Conference*, 2009.

[90] T. Inamori, N. Sako, and S. Nakasuka, "Magnetic dipole moment estimation and compensation for an accurate attitude control in nano-satellite missions," *Acta Astronaut.*, vol. 68, no. 11–12, pp. 2038–2046, 2011.

[91] D. Noack, J. Ludwig, P. Werner, M. F. Barschke, and K. Brieß, "FDA-A6 - A Fluid-Dynamic Attitude Control System for TechnoSat (presentation)," in *31st ISTS, 26th ISSFD & 8th NSAT*, 2017.

[92] PumpPortalen.se, "Gear Pump (image)." [Online]. Available: http://www.pumpportalen.se/pumphandboken/kugghjulspump/figur-3_94/. [Accessed: 26-Nov-2018].

[93] OEMPanels, "Centrifugal Pump (image)." [Online]. Available: http://www.oempanels.com/vfd-variable-frequency-drive-and-centrifugal-pump. [Accessed: 26-Nov-2018].

[94] Z. Ismail, "Spacecraft Dynamic and Controls (presentation)," 2016. [Online]. Available: https://www.slideshare.net/zuliana26/satellite-dynamic-and-control . [Accessed: 26-Nov-2018].

Appendices

- Appendix 1: Altitude - Atmospheric Density Relation
- Appendix 2: Satellite Mass – Residual Magnetic Moment Relation
- Appendix 3: Integration of Angular Momentum in Rounded Corners
- Appendix 4: Reverse-Calculation of MHD Pumping Efficiencies
- Appendix 5: User Manual for the Sizing Model
- Appendix 6: Mass Optimizations of Fluid Loops for Various Missions

Appendix 1: Altitude - Atmospheric Density Relation

NRLMSISE-00 Atmosphere Model

This page enables the computation and plotting of any subset of MSIS parameters: neutral temperature, exospheric temperature, densities of He, O, N2, O2, Ar, H, N, and total mass density.

Select Date (1960/02/14 - 2018/03/17 New: End date updating monthly) and Time
Year 2001 **Month:** March **Day(1-31):** 20
Time Universal **Hour of day** (e.g. 1.5): 12
Select Coordinates
Coordinates Type Geographic
Latitude(deg.,from -90. to 90.): 0 **Longitude**(deg.,from 0. to 360.): 0
Height (km, from 0. to 1000.): 100.
Select a Profile type and its parameters:
Height,km [0. - 1000.] Start 200 Stop 1000. Stepsize 50.

Optional Input parameters:
Note :If user does not specify these parameters,they will be taken from real data base
F10.7(daily) **F10.7(3-month avg)** 200 **ap(daily)**

Select output form:
- List model data
- Create model data file in ASCII format for downloading
- Plot model data

Note 1: The first selected parameter below always will be along the X-axis, the other selections will be along Y-axis. (e.g. if you want a Height profile, you may specify Height as the first parameter in the listing below.)
Note 2: User may get scatter plot if he specifies any two parameters below and changes the "connect type" in the "Advanced plot selections" to "show points only"

Submit Clear

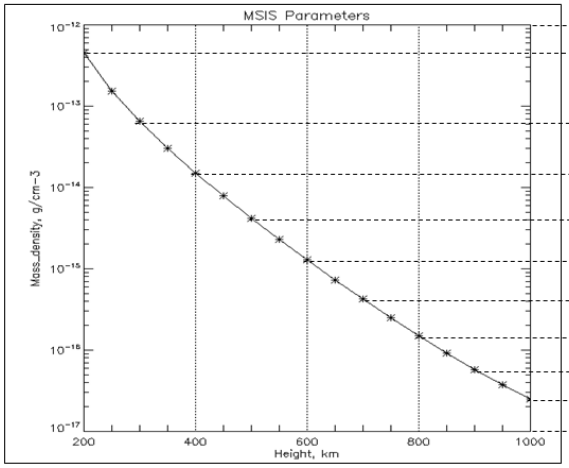

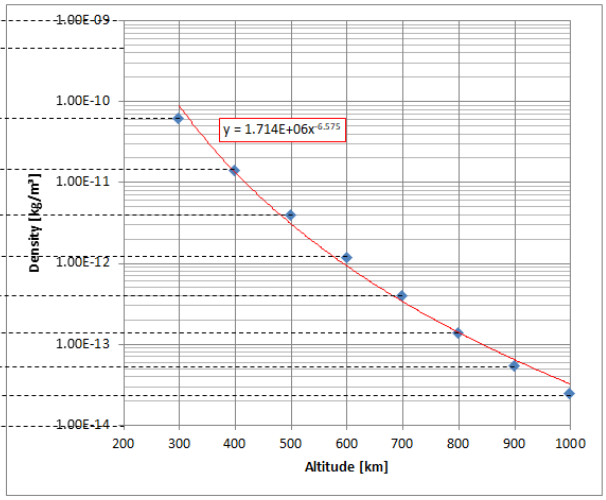

Datapoints from MSIS-E-00 (graphically determined)		
height (km)	**density [g/cm³]**	**density [kg/m³]**
200	4.50E-13	4.50E-10
300	6.30E-14	6.30E-11
400	1.40E-14	1.40E-11
500	4.00E-15	4.00E-12
600	1.20E-15	1.20E-12
700	4.00E-16	4.00E-13
800	1.40E-16	1.40E-13
900	5.50E-17	5.50E-14
1000	2.50E-17	2.50E-14

Given by Excel		
$\rho = 1.714E6\ h^{-6.575}$	**dev from MSIS**	**|dev| from MSIS**
1.2E-09	175.44%	175.44%
8.6E-11	36.53%	36.53%
1.3E-11	-7.46%	7.46%
3.0E-12	-25.40%	25.40%
9.0E-13	-25.08%	25.08%
3.3E-13	-18.49%	18.49%
1.4E-13	-3.27%	3.27%
6.2E-14	13.43%	13.43%
3.1E-14	24.76%	24.76%

Appendix 2: Satellite Mass – Residual Magnetic Moment Relation

Satellite	Mass (kg)	Magnetic moment (Am^2)	Ref.
Pace	2	5^E-4	[88]
Dart	3	9^E-3	[89]
PRISM	8.5	0.06	[90]
Nano-JASMINE	35	0.1	[90]
FireSat (smad)	130	0.5	[7]
SCS (smad)	215	1	[7]

m [kg]	D [Am²]	D=0.00441m	dev
2	0.0005	0.00882	-1664.00%
3	0.009	0.01323	-47.00%
8.5	0.06	0.03749	37.53%
35	0.1	0.15435	-54.35%
130	0.5	0.5733	-14.66%
215	1	0.94815	5.19%

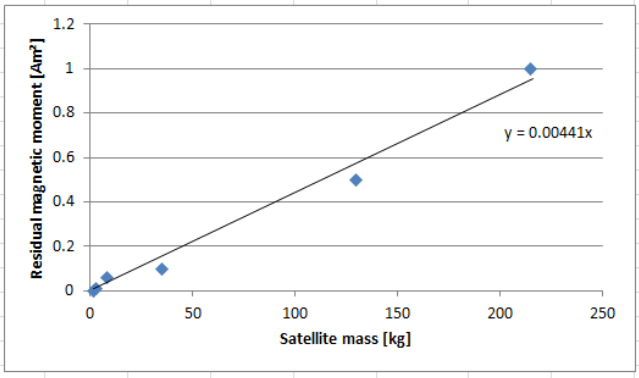

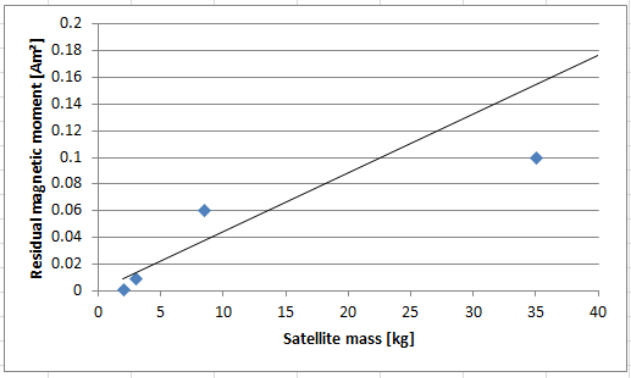

Appendix 3: Integration of Angular Momentum in Rounded Corners

Note that the screenshot below is of only one case, but has been done for multiple cases that all yield the same result – a maximum deviation of 5.8%. at R(corner)/R(perp) = 0.5.

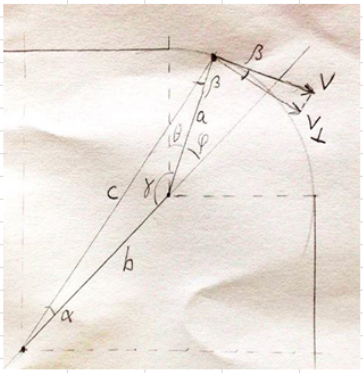

Q	1	L/min
d	0.004	m
rho	3000	kg/m³
A	1.26E-05	m²
v	1.33	m/s
R(corner)	0.01	m
R(perp)	0.1	m
L straights		
m(4 corne	2.37E-03	kg
m(4cnr ch	2.37E-04	kg
a	0.01	m
b	0.127	m

1.67E-05 m³/s

H EASY		
H straight	3.60E-03	N m s
H corners	3.14E-04	N m s
H added	3.91E-03	N m s
H(tot)	**3.91E-03**	**N m s**

H INTEGRATED		
H straight	3.60E-03	N m s
H corners	3.95E-04	N m s
H (tot)	**4.00E-03**	**N m s**

R(perp) 0.1 m

R(corner)/R(perp)	R(corner)	H easy	H integrat	% difference
0	0	4	4	0.000%
0.1	0.01	3.91	4	2.250%
0.2	0.02	3.83	3.97	3.526%
0.3	0.03	3.74	3.93	4.835%
0.4	0.04	3.66	3.87	5.426%
0.5	0.05	3.57	3.79	5.805%
0.6	0.06	3.48	3.69	5.691%
0.7	0.07	3.4	3.58	5.028%
0.8	0.08	3.31	3.45	4.058%
0.9	0.09	3.23	3.3	2.121%
1	0.1	3.14	3.14	0.000%

theta	m(i)	gamma	R = c	beta	v(perp)	H(i)
0						
0.005	6.58E-08	135.005	0.1345	38.3	1.04048	9.21E-09
0.015	6.58E-08	135.015	0.1345	38.3	1.04058	9.21E-09
0.025	6.58E-08	135.025	0.1345	38.3	1.04068	9.21E-09
0.035	6.58E-08	135.035	0.1345	38.3	1.04078	9.21E-09
0.045	6.58E-08	135.045	0.1345	38.3	1.04088	9.21E-09
0.055	6.58E-08	135.055	0.1345	38.3	1.04098	9.22E-09
0.065	6.58E-08	135.065	0.1345	38.3	1.04108	9.22E-09
0.075	6.58E-08	135.075	0.1345	38.3	1.04118	9.22E-09
0.085	6.58E-08	135.085	0.1345	38.3	1.04128	9.22E-09
0.095	6.58E-08	135.095	0.1345	38.3	1.04139	9.22E-09

Appendix 4: Reverse-Calculation of MHD Pumping Efficiencies

FDA-A6

Table 2. Characteristics of the FDA-A6

Parameter	Values
Angular momentum capacity	0.035 Nms
Max. torque	0.100 Nm
Max. Power consumption	5 W
Working medium	Ga-In-Sn
Loop diameter	300 mm
Total mass	1085 g
Databus	CAN 2.0 – with 1 Mbit/s

m(fluid)	390 gram	
FDA-A6		
Max T	0.1	N m
Max H	0.035	N m s
Max P	4.7	W
m	0.39	kg
D	0.3	m
rho	6440	kg/m³
mu	2.40E-03	Pa s
nu	3.73E-07	
R	0.15	m
A	6.42551E-05	m²
w=b	0.008015928	m
r	0.0045	m
d(h)	0.008015928	m
d	0.00905	m
d	9.05	mm
v(max)	0.598290598	m/s
Q	3.84E-05	m³/s
Q	2.31	L/min
Q(dot max)	1.10E-04	m³/s²
Nr (max)	12869	
P(hydro, max)	0.149	W
P(elec)	4.7	W
efficiency	**3.2%**	

FDA-A2

Table 1
System parameters of FDA-A2.

Angular momentum[a]	180×10^{-6} N m s
Maximum torque[a]	400×10^{-6} N m
Power consumption[b]	94 mW
Working fluid	Galinstan
Fluid mass	20 g
Fluid ring diameter	80 mm
Total mass[c]	106 g

[a] At 3.3 V.
[b] Actuator only.
[c] Excluding battery.

Table 2
Comparison of the RW1 flight model and the FDA-A2 laboratory prototype.

Parameter	RW1	FDA-A2
Angular momentum[a] (N m s)	100×10^{-6}	100×10^{-6}
Maximum torque (N m)	4×10^{-6}	400×10^{-6}
Power[a,c] (mW)	620	90
Max. power[b,c] (mW)	720	140
Total mass[c] (g)	57	106

[a] Nominal.
[b] Max. torque.
[c] Incl. electronics.

FDA-A2		
Max T	4.00E-04	N m
Max H	1.00E-04	N m s
Max P	0.09	W
m	0.02	kg
D	0.08	m
rho	6440	kg/m³
mu	2.40E-03	Pa s
nu	3.73E-07	
R	0.040	m
A	1.23568E-05	m²
w=b	0.003515217	m
r	0.00198	m
d(h)	0.003515217	m
d	0.00397	m
d	3.97	mm
v(max)	0.125	m/s
Q	1.54E-06	m³/s
Q	0.09	L/min
Q(dot max)	6.18E-06	m³/s²
Nr (max)	1330	
P(hydro, max)	0.000259	W
P(elec)	0.09	W
efficiency	**0.29%**	

H=rho L R Q

3 SIMULATED EXAMPLES

	CubeWheel S	CubeWheel M	CubeWheel L
Weight	55 g	130 g	200 g
Lenght	28 mm	46 mm	57 mm
Width	31 mm	46 mm	57 mm
Height	26 mm	31.5 mm	31.5 mm
Torque	0.23 mNm	1.0 mNm	2.3 mNm
Angular Momentum	1.7 mNms	10 mNms	30 mNms
Power	< 600 mW	< 1000 mW	< 2200 mW
	MHD Wheel S	MHD Wheel M	MHD Wheel L
Weight (Liquid)	64 g	124 g	181 g
Outer Radius	45 mm	45 mm	45 mm
Inner Radius	43 mm	41 mm	39 mm
Height	10 mm	10 mm	10 mm
Torque(@1A/s)	0.18 mNm	0.36 mNm	0.53 mNm
Angular Momentum(@1A)	0.18 mNms	0.36 mNms	0.53 mNms
Power(@1A)	0.55 mW	0.54 mW	0.52 mW

Table 8.1: *Comparison between classical Reaction Wheels for Cubesats and Liquid Wheels*

	S	M	L	
m	0.64	0.124	0.181	kg
OR	0.045	0.045	0.045	m
IR	0.043	0.041	0.039	m
h	0.01	0.01	0.01	m
T	1.80E-04	3.60E-04	5.30E-04	N m
H	1.80E-04	3.60E-04	5.30E-04	N m s
P	5.50E-04	5.40E-04	5.20E-04	W
rho	13545	13545	13545	
mu	1.55E-03	1.55E-03	1.55E-03	
nu	1.14E-07	1.14E-07	1.14E-07	
w	0.002	0.004	0.006	m
R	0.044	0.043	0.042	m
m (A L)	0.075	0.146	0.214	kg
d(h)	0.00333	0.00571	0.00750	mm
Q	1.09E-06	2.29E-06	3.53E-06	m³/s
Q	0.066	0.137	0.212	L/min
Q(dot,max)	1.09E-06	2.29E-06	3.53E-06	m³/s²
P(hydro, max)	0.00045	0.0003	0.00025	W
P(elec)	5.50E-04	5.40E-04	5.20E-04	W
efficiency	**81.82%**	**55.56%**	**48.08%**	

Reynolds number N(R) 3675

Appendix 5: User Manual for the Sizing Model

Welcome to the fluid loop sizing model!

- The model can be used in two different modes:
    - Manual mode (1)
    - Optimization mode (2)
- There is also an auxiliary function for formulating requirements based on the disturbance environment of the satellite. This is not explained as this is self-explanatory.
- The model has some important limitations (3).
- The model has been verified by tests with a fluid loop prototype.
- This manual refers to the Excel worksheet "Fluid Loop Sizing Model.xml".

1. Manual Mode

The Manual Mode gives the fluid loop's performance parameters based on manually specified design parameters. It can be used to:

- Manually and iteratively size a fluid loop and compare its performance to the given requirements.
- Tweak the design after the Solver (2) has found optimized results.

1.1 Instructions

1. **[Optional]** Fill in the REQUIREMENTS fields, to compare the fluid loop to the required specifications. This can be based on:
    a. Customer requirements;
    b. Reaction wheel specifications;
    c. Other specifications that need to be matched.
2. Fill in the FLUID LOOP DESIGN PARAMETERS fields.
    a. For unknown values, there are suggested values in the respective cell comments.
    b. For most missions, a square loop shape is advised, because it fits best along the outer edges of the satellite bus. A corner radius of at least 3 times the channel diameter is advised, in order to prevent friction losses associated with sharp elbows. This can be automated by entering in cell J34 "=3*J31".

c. The loop diameter should be chosen as large as possible, so that the angular momentum and torque are maximized.
d. The "Assumptions" fields do not have to be changed often. Each cell has a comment with some suggested typical values.
    i. The "Maximum pump flow rate acceleration" determines the torque capability of the fluid loop. Unfortunately, pumps are only rated for flow rate rather than acceleration. Some reverse-calculated values can be used here. However, since fluid loops generally have a high torque capability it can be assumed that a fluid loop sized for a certain angular momentum will also fulfil the torque requirements. Based on previous research, centrifugal pumps may not fulfil the torque requirements [26], whereas MHD [91] and gear pumps (Section 5.3.2; or other positive displacement pumps) do have a high acceleration/torque capability, so most likely will.
    ii. The channel wall thickness and material density are used to calculate the total mass of the actuator. This can be tweaked according to the expected channel properties. Suggested values are 0.5 – 1 mm thick Aluminium (2700 kg/m³) or plastic (1100 kg/m³).
    iii. The channel surface roughness can remain on smooth (0.0015 mm) for standard plastic tubing. It marginally influences viscous friction losses in turbulent flow.

3. Assess the resulting FLUID LOOP PERFORMANCE PARAMETERS.
    a. If unrealistic values turn up, check the design parameters for correctness.

2. Optimization Mode

The Optimization Mode finds optimal FLUID LOOP DESIGN PARAMETERS based on given REQUIREMENTS and constraints. This mode uses the Solver function in Excel. It can be used to:

- Optimize the mass, angular momentum or power consumption of a fluid loop, while matching the customer requirements

2.1 Setting up the Solver

1. Install Solver: File > Options > Add-ins > Manage > Excel Add-ins > Go > OK
2. Open Solver: Data tab > Analysis > Solver.

3. Set Objective Cell to be optimized.
    a. Maximize (e.g. angular momentum of fluid loop)
    b. Minimize (e.g. mass or power consumption of fluid loop)
4. Set Variables. Select the cells that should be changed by the Solver until it arrives at the optimal solution. Typically, the variables are:
    a. Loop diameter
    b. Channel diameter
    c. Number of coils
    d. Pump flow rate
5. Set constraints by clicking "Add". Constraints set the boundaries between which the Solver will allow solutions. This ensures that requirements are met and values remain realistic. The constraints below are used for optimizing mass, while matching the angular momentum requirement, within the power budget. Slightly different constraints should be used for other optimization modes!
    a. Add constraints so that the customer requirements are met.
        i. Fluid loop angular momentum should match the required angular momentum (X6 = J6).
        ii. Fluid loop power consumption should be smaller than the power budget (X10 >= J10). The smallest calculated power is used here, because the tests found that these are the most accurate (except for sharp elbows, in which case the maximum value should be used).
        iii. Fluid loop outside dimension should be equal to the Maximum outside dimension (X16 = I16). Using a "<=" instead of a "=" is technically correct, but should not be done because this results in the Solver giving a near-zero loop diameter with thousands of coils (because this optimizes the mass).
    b. Add constraints so that the values remain realistic.
        i. Number of coils should be a whole number (J25 = int).
        ii. Number of coils should be larger than 1 (J25 >= 1).
        iii. Loop diameter should be larger than 0 (J30 >= BM4).
        iv. Channel diameter should be larger than 0 (J30 >= BM4).
        v. Pump flow rate should be larger than 0 (J30 >= BM4).
        vi. The corner radius should be smaller than half the loop diameter (J34 <= J16/2)

c. Add constraints between which values the solver can attempt solutions.
    i. The Pressure drop Δp(min) should not exceed the Maximum pump pressure (X31 <= J42)
    ii. The Pump flow rate should be not exceed the Maximum pump flow rate (J38 <= J41)

2.2 Instructions

6. Fill in the REQUIREMENTS fields with, for instance:
    a. Customer requirements;
    b. Reaction wheel specifications;
    c. Other specifications that need to be matched.
7. Set a loop shape.
    a. For most missions, a square loop shape is advised, because it fits best along the outer edges of the satellite bus. If it is square, a corner radius of at least 3 times the channel diameter is advised, in order to prevent friction losses associated with sharp elbows. This can be automated by entering in cell J34 "=3*J31".
8. Set the Channel shape to "circular".
    a. The "rectangular" channel option can only be used in Manual mode.
9. Set fluid properties (values in the cell comments).
10. Set the pump properties (suggested values in the cell comments).
    a. The Maximum pump flow rate and Maximum pump pressure serve as constraints, so are useful to fill in. If this is not done, it is possible that the Solver suggests very high flow rates or pressures that no spacecraft-sized pump can match.
11. Set the Channel wall material and Channel wall thickness.
    a. These values can be tweaked after solving to optimize the mass further.

12. Open Solver.
13. After setting all boundary conditions (step 1–5 and 6–11), click Solve.
14. Assess whether the results are realistic.
    a. If negative values are given, enter a positive value and try solving again.
    b. Sometimes, Solver gives an error message. This can be the result of too stringent requirements or constraints. Adjust accordingly.
15. If satisfied with the results, copy the desired parameters into a table. Register parameters that are interesting or necessary to recreate the configuration, such as:

a. Type of fluid
b. Loop and channel diameter; number of coils
c. Angular momentum, mass, power consumption (and used efficiency)
d. Flow rate, pressure drop

16. Repeat this process for different fluids, pumps, dimensional constraints, etc. Register results.
17. Compare the results of all configurations to one another.
18. Pick the best one for further design or analysis.

3. Limitations

1. The calculation of the fluid loop torque is based on an assumed flow rate acceleration, obtained from reverse-calculated reported values of MHD-pumped fluid loops. This means that the model is not very useful for torque sizing. However, based on reported results, the torque of (MHD-pumped) fluid loops is expected to be much higher than a reaction wheel with a similar angular momentum. Gear pumps too appear to have a high torque capability. Centrifugal pumps less so. This means that a fluid loop sized for angular momentum will most likely also fulfil the torque requirement (except for centrifugal pumps, which should be assessed separately).
2. The electrical power consumption of the fluid loop is based on an assumed overall pump efficiency. The suggested efficiency values are based on typical values of mechanical pumps, reverse-calculated values from existing and simulated MHD pumps. Although the suggested values are quite accurate, the real values vary widely with pump and system parameters. More accurate results can be obtained by characterizing individual pumps. The power component that is needed to push the liquid through the channel (hydraulic power consumption) does remain correct, because it only depends on flow rate and pressure drop.
3. The orbital disturbance environment calculation is based on many assumptions and simplifications. It can therefore only give rough order-of-magnitude requirements. The results resemble real mission values most accurately for 10 - 200 kg satellites.
4. The orbital disturbance environment requirement calculation only works for LEO satellites.

Appendix 6: Mass Optimizations of Fluid Loops for Various Missions

Excel Solver settings

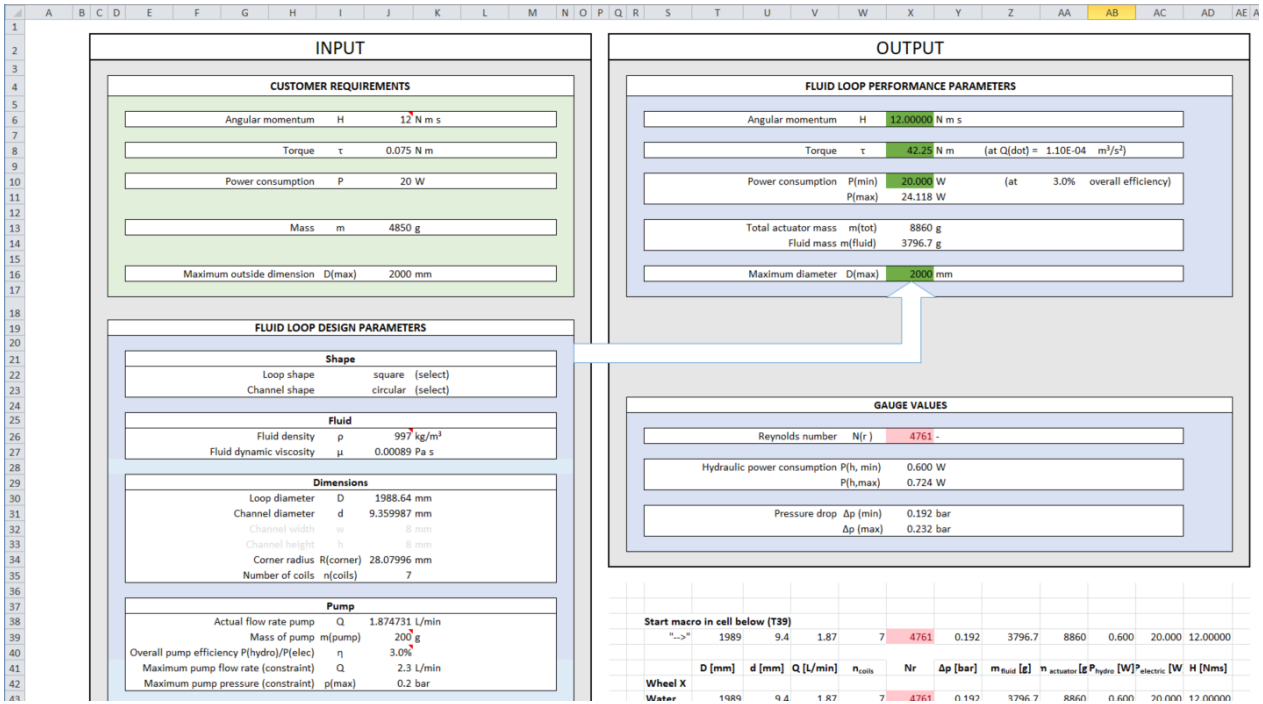

INPUT

CUSTOMER REQUIREMENTS

Angular momentum	H	12 N m s
Torque	τ	0.075 N m
Power consumption	P	20 W
Mass	m	4850 g
Maximum outside dimension	D(max)	2000 mm

FLUID LOOP DESIGN PARAMETERS

Shape		
Loop shape		square (select)
Channel shape		circular (select)
Fluid		
Fluid density	ρ	997 kg/m³
Fluid dynamic viscosity	μ	0.00089 Pa s
Dimensions		
Loop diameter	D	1988.64 mm
Channel diameter	d	9.359987 mm
Channel width	w	8 mm
Channel height	h	8 mm
Corner radius	R(corner)	28.07996 mm
Number of coils	n(coils)	7
Pump		
Actual flow rate pump	Q	1.874731 L/min
Mass of pump	m(pump)	200 g
Overall pump efficiency P(hydro)/P(elec)	η	3.0%
Maximum pump flow rate (constraint)	Q	2.3 L/min
Maximum pump pressure (constraint)	p(max)	0.2 bar

OUTPUT

FLUID LOOP PERFORMANCE PARAMETERS

Angular momentum	H	12.00000 N m s		
Torque	τ	42.25 N m	(at Q(dot) =	1.10E-04 m³/s²)
Power consumption	P(min)	20.000 W	(at	3.0% overall efficiency)
	P(max)	24.118 W		
Total actuator mass	m(tot)	8860 g		
Fluid mass	m(fluid)	3796.7 g		
Maximum diameter	D(max)	2000 mm		

GAUGE VALUES

Reynolds number	N(r)	4761	-
Hydraulic power consumption	P(h, min)	0.600	W
	P(h,max)	0.724	W
Pressure drop	Δp (min)	0.192	bar
	Δp (max)	0.232	bar

Start macro in cell below (T39)

	D [mm]	d [mm]	Q [L/min]	n_{coils}	Nr	Δp [bar]	m_{fluid} [g]	$m_{actuator}$ [g]	P_{hydro} [W]	$P_{electric}$ [W]	H [Nms]
"-->"	1989	9.4	1.87	7	4761	0.192	3796.7	8860	0.600	20.000	12.00000
Wheel X											
Water	1989	9.4	1.87	7	4761	0.192	3796.7	8860	0.600	20.000	12.00000

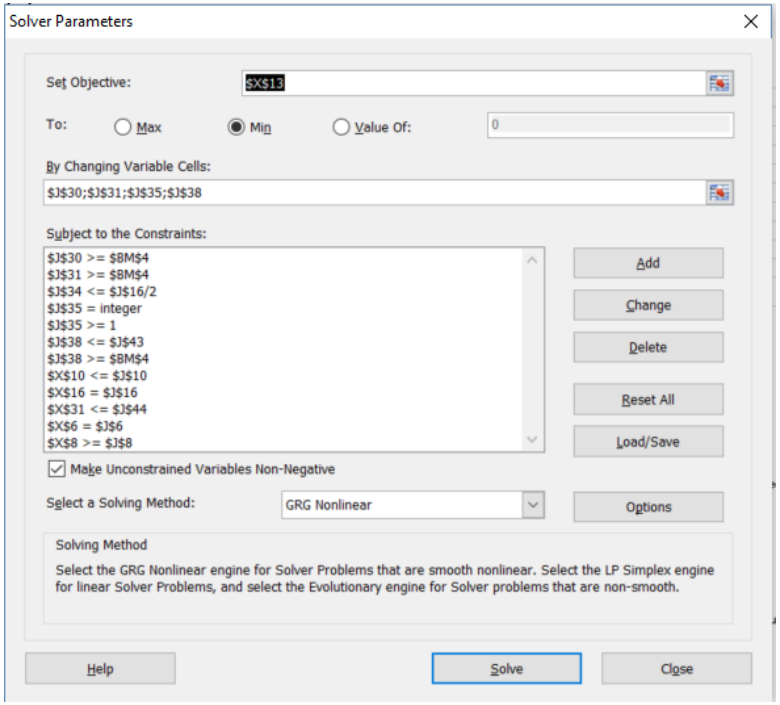

ZAcube-1

		D [mm]	d [mm]	Q [L/min]	n_{coils}	Nr	Δp [bar]	m_{fluid} [g]	$m_{actuator}$ [g]	P_{hydro} [W]	$P_{electric}$ [W]	H [Nms]
	CubeWheel S								60		0.320	0.00177
Centrifugal pump 1	Water	96	2.1	0.12	7	1364	0.095	9	90	0.019	0.320	0.00177
	SPT (2500 kg/m³]	95	3.2	0.10	5	180	0.100	37	114	0.016	0.275	0.00177
	Galinstan	96	2.4	0.10	3	2450	0.100	33	77	0.017	0.288	0.00177
	Mercury	96	2.4	0.11	2	8412	0.100	47	81	0.019	0.308	0.00177
Gear pump 1	Water	97	1.1	0.01	24	217	0.384	8.6	212	0.006	0.320	0.00177
	SPT (2500 kg/m³]	96	1.7	0.01	16	32	0.420	33.5	211	0.006	0.320	0.00177
	Galinstan	97	1.1	0.01	10	476	0.431	21.9	129	0.006	0.320	0.00177
	Mercury	97	0.9	0.01	7	1853	0.448	21.1	103	0.006	0.320	0.00177
MHD 1	Galinstan	95	2.6	0.10	3	2271	0.040	38.3	97	0.007	0.232	0.00177
	Mercury	95	3.0	0.11	2	6976	0.040	70.3	120	0.008	0.252	0.00177

BRITE

		D [mm]	d [mm]	Q [L/min]	n_{coils}	Nr	Δp [bar]	m_{fluid} [g]	$m_{actuator}$ [g]	P_{hydro} [W]	$P_{electric}$ [W]	H [Nms]
	Wheel X								185		0.3	0.03
Centrifugal pump 1	Water	193	4.8	0.39	8	1951	0.028	105.9	410	0.018	0.300	0.03000
	SPT (2500 kg/m³]	193	4.9	0.12	9	148	0.088	317.4	666	0.018	0.300	0.03000
	Galinstan	195	3.0	0.10	6	1996	0.100	204.8	371	0.017	0.289	0.03000

	Mercury	195	3.3	0.11	4	6206	0.096	363.4	488	0.018	0.300	0.03000
Gear pump 1	Water	196	1.6	0.01	49	148	0.366	74.3	947	0.006	0.300	0.03000
	SPT (2500 kg/m³]	195	2.5	0.01	31	23	0.361	296.8	1048	0.006	0.300	0.03000
	Galinstan	196	1.6	0.01	20	334	0.394	191.0	568	0.006	0.300	0.03000
	Mercury	197	1.3	0.01	14	1303	0.408	183.5	433	0.006	0.300	0.03000
MHD 1	Galinstan	194	4.0	0.15	5	2154	0.035	311.2	498	0.009	0.300	0.03000
	Mercury	194	4.1	0.11	4	5177	0.040	530.7	685	0.008	0.252	0.03000

Skysat

		D [mm]	d [mm]	Q [L/min]	n_{coils}	Nr	Δp [bar]	m_{fluid} [g]	$m_{actuator}$ [g]	P_{hydro} [W]	$P_{electric}$ [W]	H [Nms]
	Microwheel 200								940		7	0.18
Centrifugal pump 2	Water	794	3.7	0.35	5	2201	0.170	172.2	856	0.098	1.632	0.18000
	SPT (2500 kg/m³]	791	6.7	0.87	2	772	0.170	544.7	1001	0.247	4.117	0.18000
	Galinstan	792	6.3	1.35	1	12272	0.170	623.4	867	0.383	6.382	0.18000
	Mercury	793	4.9	0.64	1	23981	0.170	817.4	1026	0.181	3.018	0.18000
Centrifugal pump 3	Water	792	6.1	2.18	2	8480	0.193	183.6	762	0.700	7.000	0.18000
	SPT (2500 kg/m³]	792	6.0	0.87	2	848	0.250	449.8	1025	0.362	3.623	0.18000
	Galinstan	792	5.7	1.35	1	13426	0.250	519.4	898	0.562	5.618	0.18000
	Mercury	793	4.5	0.64	1	26242	0.250	681.0	1028	0.266	2.658	0.18000
Gear pump 2	Water	796	1.8	0.17	7	2300	2.201	56.9	786	0.642	6.416	0.18000
	SPT (2500 kg/m³]	795	2.6	0.14	5	315	3.063	204.8	884	0.700	7.000	0.18000

	Galinstan	796	1.5	0.08	4	3046	5.071	154.1	629	0.700	7.000	0.18000
	Mercury	797	1.3	0.07	3	9875	6.005	175.1	562	0.700	7.000	0.18000
Gear pump 3	Water	796	2.0	0.18	7	2091	1.500	68.9	832	0.438	4.375	0.18000
	SPT (2500 kg/m³]	794	3.8	0.38	3	599	1.097	264.3	848	0.700	7.000	0.18000
	Galinstan	795	2.9	0.33	2	6581	1.261	266.1	675	0.700	7.000	0.18000
	Mercury	796	2.2	0.16	2	13467	1.500	319.2	690	0.395	3.948	0.18000
MHD 2	Galinstan	793	4.9	0.15	3	1737	0.040	1144.5	1717	0.010	0.332	0.18000
	Mercury	791	7.0	0.64	1	17124	0.040	1620.9	1933	0.043	1.432	0.18000
MHD 3	Galinstan	794	4.2	0.33	2	7031	0.200	562.8	1041	0.112	3.722	0.18000
	Mercury	793	4.8	0.64	1	24830	0.197	761.7	1116	0.210	7.000	0.18000

Turksat 3A

		D [mm]	d [mm]	Q [L/min]	n_{coils}	Nr	Δp [bar]	m_{fluid} [g]	$m_{actuator}$ [g]	P_{hydro} [W]	$P_{electric}$ [W]	H [Nms]
	Wheel X								4850		20	12
Centrifugal pump 3	Water	1987	11.0	3.68	5	4574	0.250	3734.9	7949	1.535	15.352	12.00000
	SPT (2500 kg/m³]	1986	12.4	4.09	3	1945	0.250	7135.2	10022	1.705	17.046	12.00000
	Galinstan	1987	11.1	3.57	2	18250	0.250	9879.4	11702	1.486	14.858	12.00000
	Mercury	1989	8.8	1.69	2	35586	0.250	13037.6	14553	0.704	7.037	12.00000
Gear pump 2	Water	1996	2.4	0.19	22	1889	6.396	765.5	5965	2.000	20.000	12.00000
	SPT (2500 kg/m³]	1994	3.7	0.19	14	292	6.480	3051.3	7726	2.000	20.000	12.00000

	Galinstan	1995	2.7	0.17	9	3717	6.911	2566.4	4993	2.000	20.000	12.00000
	Mercury	1995	2.5	0.19	6	13719	6.462	3204.9	4829	2.000	20.000	12.00000
Gear pump 3	Water	1993	5.1	0.91	10	4263	1.316	1609.5	5911	2.000	20.000	12.00000
	SPT (2500 kg/m³]	1992	6.4	0.74	7	685	1.500	4473.8	8162	1.860	18.600	12.00000
	Galinstan	1992	5.5	0.88	4	9134	1.359	4870.4	6823	2.000	20.000	12.00000
	Mercury	1993	4.8	0.75	3	28835	1.500	5832.6	7205	1.864	18.641	12.00000
MHD 3	Galinstan	1988	9.8	1.58	3	9151	0.200	11609.7	13989	0.527	17.571	12.00000
	Mercury	1989	9.3	1.69	2	33786	0.200	14477.9	16056	0.563	18.780	12.00000

Quickbird

		D [mm]	d [mm]	Q [L/min]	n_{coils}	Nr	Δp [bar]	m_{fluid} [g]	$m_{actuator}$ [g]	P_{hydro} [W]	$P_{electric}$ [W]	H [Nms]
	Wheel X								6300		20	25
Centrifugal pump 3	Water	1586	11.8	4.72	8	9501	0.250	5482.6	11141	1.965	19.654	25.00000
	SPT (2500 kg/m³]	1584	13.9	4.84	5	2051	0.248	11881.8	16041	2.000	20.000	25.00000
	Galinstan	1586	11.8	2.92	4	14154	0.250	17554.5	20473	1.217	12.169	25.00000
	Mercury	1587	10.6	2.46	3	42999	0.250	22664.7	24726	1.026	10.262	25.00000
Gear pump 2	Water	1595	2.6	0.19	39	1764	6.162	1339.3	9174	2.000	20.000	25.00000
	SPT (2500 kg/m³]	1594	4.1	0.19	25	271	6.330	5318.7	12430	2.000	20.000	25.00000
	Galinstan	1595	3.0	0.18	16	3433	6.695	4552.6	8184	2.000	20.000	25.00000
	Mercury	1595	2.7	0.18	11	12237	6.659	5557.1	7974	2.000	20.000	25.00000

Gear pump 3	Water	1594	4.1	0.38	28	2219	1.500	2296.4	10133	0.947	9.473	25.00000
	SPT (2500 kg/m³]	1591	7.2	0.83	12	680	1.449	7674.7	13139	2.000	20.000	25.00000
	Galinstan	1592	5.7	0.72	8	7229	1.500	8275.0	11349	1.802	18.025	25.00000
	Mercury	1593	5.1	0.61	6	22301	1.500	10375.1	12533	1.522	15.216	25.00000
MHD 3	Galinstan	1587	11.3	1.87	5	9373	0.193	20472.3	23965	0.600	20.000	25.00000
	Mercury	1588	9.8	1.38	4	26240	0.200	25616.7	28120	0.461	15.366	25.00000